DISS. ETH NO. 16264

Correlating Statistical Properties of Aftershock Sequences to Earthquake Physics

A DISSERTATION SUBMITTED TO THE

SWISS FEDERAL INSTITUTE OF TECHNOLOGY ZURICH

FOR THE DEGREE OF

DOCTOR OF NATURAL SCIENCES

PRESENTED BY

Jochen Wößner

DIPLOMA OF GEOPHYSICS (DIPL. GEOPHYS.)
UNIVERSITY OF KARLRUHE (TH)
BORN JUNE 25, 1973
CITIZEN OF GERMANY

ACCEPTED ON THE RECOMMENDATION OF

Prof. Dr. D. Giardini, examiner
Dr. S. Wiemer, co-examiner
Dr. E. Hauksson, co-examiner

Zurich, 2005

Zusammenfassung

In meiner Doktorarbeit habe ich statistische Methoden zur Analyse von Erdbebenkatalogen im Allgemeinen und von Nachbebensequenzen im Speziellen entwickelt. In der Statistischen Seismologie sind diese Methoden grundlegend, um detaillierte Untersuchungen mit Gesetzmässigkeiten wie dem Gutenberg-Richter Gesetz und dem modifizierten Omori Gesetz durchzuführen, sowie deren Parameter und Unsicherheiten zu bestimmen. Mittels der Analyse von Seismizitätsparametern zeige ich, dass die räumlichen und zeitlichen Eigenschaften von Nachbebensequenzen in Relation zum Versatz und Spannungsänderungen auf Bruchflächen stehen und sich diese Zusammenhänge in der Heterogenität der Seismizitätsparameter auf allen Skalen widerspiegeln. Meine Untersuchungen orientieren sich daran, (1) weitere Einblicke in das räumliche und zeitliche Auftreten von Erdbebenhäufungen, sogenannten Clustern, in der Nähe von seismisch aktiven Verwerfungszonen zu erhalten, (2) Zusammenhänge zu den physikalischen Prozessen am Erdbebenherd zu ermitteln und (3) Implikationen für die seismische Gefährdungsabschätzung zu analysieren.

Die Magnituden-Häufigkeitsverteilung $\log N = a - bM$ und die zeitliche Abnahme der Erdbebenrate in Nachbebensequenzen $n(t) = k(t + c)^{-p}$ hängen stark vom Magnitudenschwellwert M_c eines Erdbebenkataloges ab. Aufgrund der vielfach geringen Zuverlässigkeit bestehender Algorithmen zur Bestimmung des Magnitudenschwellwertes, habe ich eine Methode (EMR-Methode) entwickelt, die ein Seizmizitätsmodell des gesamten Magnitudenbereiches berechnet und mittels statistischer Verfahren gegen die beobachtete Magnituden-Häufigkeitsverteilung getestet werden kann. Im Gegensatz zu anderen Methoden reproduziert die EMR-Methode Magnitudenschwellenwerte von synthetischen Katalogen korrekt und erweist sich bei der Anwendung auf reale Daten im Vergleich als robuster. In Kombination

mit einer Monte Carlo Approximation der Bootstrap-Methode können simultan Unsicherheiten von M_c und b abgeschätzt werden, wobei alle zur Verfügung stehenden Methoden zur Bestimmng des Magnitudenschwellwertes angewendet werden können.

Durch Spannungsänderungen verursachte räumliche und zeitliche Ratenänderungen in der Erdkruste wurden in einer Vielzahl von Publikationen in Entfernungen grösser als $d \geq 10\,\mathrm{km}$ um Verwerfungszonen beobachtet und untersucht. Im Gegensatz dazu wurden Ratenänderungen in Nachbebensequenzen nahe an Verwerfungen ($d \leq 10\,\mathrm{km}$) und unter dem Einfluss von in der Nähe auftretenden starken Erdbeben nicht quantitativ analysiert. Deshalb habe ich ein Methode entwickelt, um relative Ratenänderungen in Nachbebensequenzen auszukartieren und um die statistische Signifikanz der Ratenänderung zu quantifizieren. Im Vergleich mit Spannungsänderungen, die basierend auf einem Modell der Coulomb-Spannungsübertragung im elastischen Halbraum berechnet wurden, konnte ich eine gute Übereinstimmung in Bereichen positiver und negativer Spannungsänderungen mit den jeweiligen Ratenänderungen ermitteln.

Komplexe Versatzverteilungen und entsprechend variable Spannungsänderungen in der Erdkruste charakterisieren Bruchflächen von Erdbeben. Es ist allgemein akzeptiert, dass diese Variabilität das Auftreten von Nachbeben ursächlich beeinflusst. Um diese Einflüsse deutlicher zu beleuchten, habe ich statistische Tests entwickelt, um Korrelationen zwischen Nachbebenhypozentren und Versatz- sowie Scherspannungsverteilungen auf der Bruchfläche von Starkbeben zu quantifizieren. In diesen Tests werden die Testhypothesen H_1, Nachbeben treten in Regionen geringen Versatzes auf, und H_2, Nachbeben treten in Regionen mit erhöhten Scherspannungen auf, gegenüber der Nullhypothese H_0, Nachbeben verteilen sich zufällig auf der Bruchfläche, geprüft. Die Ergebnisse bestätigen, dass, unter Berücksichtigung der Unsicherheiten in den Datensätzen, Nachbeben vorzugsweise in Regionen geringen Versatzes statistisch signifikant auftreten. Mit geringerer Signifikanz trifft diese Aussage auf die Korrelation mit der Scherspannungsverteilung auf der Bruchfläche des Starkbebens zu. Die Korrelationen sind bei Verwendung relokalisierter Nachbebenhypozentren statistisch signifikanter.

Um weitere Zusammenhänge zwischen dem Auftreten von Nachbeben und dem nach einem Starkbeben resultierenden Spannungsfeld zu erhalten, untersuchte ich die räumlichen Korrelation von Regionen grossen Versatzes mit der Heterogenität β des post-seismischen Spannungsfeldes, die zeitliche Evolution der Spannungsheterogenität und die Orientierung des Spannungstensors. Diese Grössen wurden mittels Inversion der Herdflächenlösungen von Nachbeben berechnet. Die Ergebnisse bestätigen, dass sich Bereiche mit grossem Versatz als Folge eines Starkbebens mit Regionen erhöhter Heterogeneität im Spannungsfeld überlagern. Weiterhin lässt sich feststellen, dass das Mass der Heterogeneität β mit der Zeit abnimmt. Meine Resultate weisen darauf hin, dass die Abnahme der Heterogeneität zur Herstellungs des Spannungszustandes vor dem Starkbeben sich auf einer kürzeren Zeitskala abspielt als die Dauer von Nachbebensequenzen allgemein. Die räumlich heterogene Dauer der Nachbebensequenzen lässt sich nicht mit derjenigen der Heterogenität des post-seismischen Spannungsfeldes korrelieren. Die beobachteten Rotationen der maximalen Spannungsachse des Spannungstensors lassen sich qualitativ mit einem Modell basierend auf der Übertragung von CoulombSpannungen im elastischen Halbraum erklären. Unter der Annahme, dass das regionale Spannungsfeld ein Grösse von 30-50 bar besitzt, bestätigte sich eine gute qualitative Übereinstimmung zwischen Modell und beobachteten Daten. Zusammen mit der Annahme, dass post-seismisch heterogene Spannungsfelder durch Erdbeben, die nahezu die komplette Scherspannung auf einer Bruchfläche abbauen, verursacht werden, deutet dies darauf hin, dass die San Andreas Verwerfung sowie die untersuchten Verwerfungen in der kalifornischen Mojave-Wüste als schwach bezeichnet werden können.

Abstract

The objectives of my research were (1) to gain more insight in the spatial and temporal occurrence of clustered seismicity in the near-source region of seismogenic faults, (2) to improve links to the underlying physics of earthquakes, and (3) to analyze implications for seismic hazard assessment. Therefore, I developed advanced statistical methods to analyze parametric earthquake catalogs in general and aftershock sequence data in particular. These methods are essential for detailed analyses of the parameters and their uncertainties for relations used in statistical seismology: the Gutenberg-Richter law and the modified Omori law. I demonstrated that the spatial and temporal evolution of aftershock sequence properties are related to the slip and stress distribution in the near-field of rupture planes, as reflected in heterogeneities of the seismicity parameters on all scales resolvable.

The frequency-magnitude distribution $\log N = a - bM$ and the temporal decay of aftershock sequences $n(t) = k(t + c)^{-p}$ are both highly dependent on the completeness level of earthquake catalogs. I introduced a new method to determine the magnitude of completeness M_c, which provides a testable seismicity model for the entire frequency-magnitude range and shows superior performance compared to previously published methods when applied to synthetic and real earthquake catalogs. In combination with a Monte Carlo approximation of the bootstrap technique, adequate estimates of the uncertainties in M_c and b can be obtained, while different methods to determine the completeness level can be applied.

Spatial and temporal variations of seismicity rates caused by static stress changes have been observed and investigated in many publications away from the causative fault ($d \geq 10\,\mathrm{km}$), but rate changes in aftershock sequences in the near-source region ($d \leq 10\,\mathrm{km}$) influenced by large events in the immediate vicinity have not been quantitatively analyzed. I developed a method to map relative rate changes in

aftershock sequences and to quantify their statistical significance. Comparing the results to a Coulomb stress transfer model, I obtain good agreement of positive and negative stress changes and seismicity rates, supporting the idea of interacting stress fields of small and large earthquakes.

Seismologists have learned that complex main shock slip patterns and the resulting changes in the state of stress of the Earths' crust are common to large earthquakes. It is widely accepted that this complexity causes the variability in aftershock generation. I developed non-standard statistical tests to correlate the hypocenter locations of aftershocks and properties of finite-fault source models: the slip and stress-drop distribution. I evaluated the test hypotheses if aftershocks are located (1) in low-slip regions H_1 or (2) in increased shear-stress regions H_2 compared to the null hypothesis H_0: Aftershocks are randomly distributed over the main-shock fault plane. The results confirm that aftershocks are preferentially located in low-slip regions with high statistical significance given the uncertainty levels in the data sets. At a lower significance level, aftershock hypocenters are correlated with the on-fault shear stress distribution and are more significant using relocated catalogs.

At a high resolution level, I spatially and temporally inverted aftershock focal mechanisms to determine the heterogneity of the stress tensor measured by the angular misfit to a homogeneous stress tensor β, the temporal evlution of $\beta(t)$, and the rotation of the stress tensor axes, to investigate the suggestions of the heterogeneous post-seismic stress field hypothesis (HPSSF-hypothesis). The results confirm that the largest heterogeneities in the stress field are in general concentrated in areas of highest coseismic slip and reveal that β decreases with time. The results suggest that (1) the stress field recovers on a shorter time scale than the aftershock sequence duration and that (2) the heterogeneity of the aftershock sequence duration along the cross-section does not correlate with the mapped stress tensor heterogeneity. Rotations of the maximum compressive stress axis σ_1 obtained from the stress tensor inversion are qualitatively matched using a conceptual model based on Coulomb stress transfer, assuming a background stress field on the order of 30-50 bars. Combining the results of the stress tensor inversion and the confirmed assumptions of the HPSSF-hypothesis suggests that the San Andreas fault and faults in the eastern California shear zone are relatively weak.

Contents

List of Tables

Seite Leer /
Blank leaf

List of Figures

Chapter 1

General Introduction

Earthquakes are a serious threat to society and human beings. Large earthquakes are one of the most hazardous natural disasters summing up to approximately 50 percent of the total loss in human life and 30 percent of economic losses over the last 50 years (*Berz*, 2000). Nature dramatically demonstrated its destructive power with the devastating $M_W = 9.3$ Sumatra-Andaman earthquake on December 26^{th}, 2004, causing about 300 000 fatalities, many related to the subsequent tsunami (*Ni et al.*, 2005; *Sieh*, 2005).

Scientists and decision makers are responsible to develop efficient procedures to mitigate earthquake risk in order to reduce casualties and financial losses in future. Increasingly important, from a scientific point of view, is the implementation of physically-based time-dependent hazard models in the assessment of seismic risk (*Stein*, 1999; *Wiemer*, 2000; *Gerstenberger et al.*, 2005). To construct these models, it is essential to improve our understanding of the earthquake source processes, wave propagation effects, and seismicity patterns. I aim to contribute to the scientific efforts by developing statistical methods to gain new insights in the spatial and temporal occurrence of clustered seismicity in the near-source region of seismogenic faults, to improve links to the underlying physics of earthquakes and to analyze implications for seismic hazard assessment.

I address these problems in the immediate vicinity of seismogenic faults adding further detail to a wealth of published research on stress changes, earthquake triggering and effects on seismicity rates caused by large main shocks (e. g., *Harris*, 1998; *Kagan and Jackson*, 1998; *Toda et al.*, 1998; *Stein*, 1999; *Gomberg et al.*, 2001; *Steacy et al.*, 2005; *Toda et al.*, 2005)), but leaving aside the closest 5–10 km around the causative fault. Here, it is essential to include the complexity of slip distributions that seismologists have learned to image, the heterogeneities in the stress field common to follow moderate and large earthquakes, and the spatio-temporal properties describing the interaction of clustered seismicity. The principle questions during my research with the focus on observational seismology were:

- What do aftershock seismicity patterns and aftershock focal mechanisms tell us about stress conditions on the fault?
- Can we understand the complexity of aftershock seismicity in relationship to mainshock slip?
- What are the implications for seismic hazard assessment?

1.1 Chapter Contents

The variability of seismicity parameters in space and time, the interdependence of these parameters, and systematic changes have been observed in various tectonic regimes (e. g., *Wiemer and Katsumata*, 1999; *Wiemer and Wyss*, 2000; *Wiemer et al.*, 2002). The importance of the magnitude of completeness, the magnitude level above which it is assumed to detect and locate each earthquake in a region covered by seismic network, has been emphasized in *Gerstenberger* (2004). Based on these findings, I have dedicated a large fraction of my thesis work to develop methods and tools to assess the quality of modern parametric earthquake catalogs being one of the most important products of seismological research. I introduced a new likelihood based method to estimate the completeness level using a constrained

non-linear grid search algorithm, compared the performance against existing methods and introduced a Monte-Carlo approximation of the bootstrap method to estimate adequate uncertainties. Including the entire magnitude range in the estimation, I was able to provide a complete frequency-magnitude model which can be tested against observed seismicity using standard statistical tests. This work has been published in *The Bulletin of the Seismological Society of America* in 2005 (*Woessner and Wiemer*, 2005).

Building upon the improved understanding of earthquake catalogs, I investigated the interaction of small and large earthquake in a special case of an earthquake doublet that allowed me to compare rate changes in the aftershock sequence of the first $M_W = 6.1$ event with Coulomb stress changes induced by a second $M_W = 6.0$ event, following only 49 days later in a distance of about 10 km. I developed a procedure to estimate relative rate changes and analyzed them with respect to results of Coulomb stress transfer computations of *Toda and Stein* (2003). The approach proved to be a viable tool to analyze rate changes in clustered seismicity in the larger surroundings of faults and particularly in the near-source region of moderate earthquakes. This research was published in *Geophysical Research Letters* in 2004 (*Woessner et al.*, 2004a).

Due to the limitations in the resolution of complex slip distributions of large earthquakes and the location accuracy of earthquake hypocenters, surprisingly little research except qualitative comparisons has been published on the spatial relation between man shock slip and its aftershock distribution. *Das and Henry* (2003) approached this topic mainly for large subduction zone earthquakes and wrote a summary on the early works (e. g., *Das and Aki*, 1977; *Aki*, 1979, 1984; *Mendoza and Hartzell*, 1988; *Beroza and Zoback*, 1993). On the basis of these results, it is widely accepted that parts of large earthquakes with high slip during the main shock have

relatively few aftershocks (*Yeats et al.*, 1997); however, this had not been tested in a quantitative way. Recent improvements to image the earthquake source using a variety of data sets from strong motion recordings to satellite data (e. g., *Beroza and Spudich*, 1988; *Wald and Heaton*, 1994; *Ji et al.*, 2002a), refined location techniques (*Waldhauser and Ellsworth*, 2000; *Hauksson and Shearer*, 2005; *Shearer et al.*, 2005) and fast availability of these results online allowed to gain new quantitative insight in the relation between these parameters. I developed non-standard statistical tests and obtained statistically significant correlations between hypocenter locations of aftershocks and the slip complexity in support of the asperity model (*Haskell*, 1966; *Aki*, 1967) for the primarily vertical strike-slip events studied. Using relocated earthquake catalogs lead in general to higher statistical significance levels emphasizing the need for accurate and fast available data. The statistical tests allow to approach other problems in seismology and has in a similar manner been applied to test earthquake forecasts (*Schorlemmer et al.*, 2004b). This research has been submitted to the *Journal of Geophysical Research* in 2005 and is currently under peer review.

In the last chapter, I revisited the heterogeneous post-seismic stress field (HPSSF) hypothesis (*Michael et al.*, 1990) to explore the relation between the stress field orientation and its observed heterogeneity with the main shock slip complexity. I added a temporal component to the earlier works (*Michael*, 1987b; *Wiemer et al.*, 2002) finding a fast decay of the stress field heterogeneity measure β starting shortly after the main shock, occurring on a shorter time scale than the aftershock sequence durations for several Californian earthquakes. I used the detailed mapping of modified Omori law parameters to estimate the spatial variability of aftershock sequence durations which proved to be laterally very heterogeneous. Both approaches have yet not been linked in detail to the underlying physics; however I have developed a conceptual model based on Coulomb stress transfer (*Stein et al.*, 1992; *King et al.*,

1994) that is prone to explain the heterogeneity of the stress field, the rotations of the maximum compressive stress axis, and the temporal dependence considering various loading mechanisms, e. g., tectonic loading, viscoelastic relaxation (*Freed and Lin*, 2001), or fluid flow (*Nur and Booker*, 1972; *Hickman et al.*, 1995, and references therein).

Chapter 2

Assessing the Quality of Earthquake Catalogues: Estimating the Magnitude of Completeness and Its Uncertainty

This chapter is published in the Bulletin of the Seismological Society of America: J. Woessner and S. Wiemer, Assessing the Quality of Earthquake Catalogues: Estimating the Magnitude of Completeness and Its Uncertainty, (2005), *Bull. Seism. Soc. Am.*, 95(2), April, doi:10.1785/0120040007.

2.1 Abstract

We introduce a new method to determine the magnitude of completeness M_c and its uncertainty. Our method models the entire magnitude range (EMR method) consisting of the self-similar complete part of the frequency-magnitude distribution and the incomplete portion, thus providing a comprehensive seismicity model. We compare the EMR method with three existing techniques, finding that EMR shows a superior performance when applied to synthetic test cases or real data from regional and

global earthquake catalogues. This method, however, is also the most computationally intensive. Accurate knowledge of M_c is essential for many seismicity-based studies, and particularly for mapping out seismicity parameters such as the b-value of the Gutenberg-Richter relationship. By explicitly computing the uncertainties in M_c using a bootstrap approach, we show that uncertainties in b-values are larger than traditionally assumed, especially when considering small sample sizes.
As examples, we investigated temporal variations of M_c for the 1992 Landers aftershock sequence and found that it was underestimated on average by 0.2 with former techniques. Mapping M_c on a global scale, M_c reveals considerable spatial variations for the Harvard Centroid Moment Tensor (CMT) ($5.3 \leq M_c \leq 6.0$) and the International Seismological Centre (ISC) catalogue ($4.3 \leq M_c \leq 5.0$).

2.2 Introduction

Earthquake catalogues are one of the most important products of seismology. They provide a comprehensive database useful for numerous studies related to seismotectonics, seismicity, earthquake physics, and hazard analysis. A critical issue to be addressed before any scientific analysis is to assess the quality, consistency and homogeneity of the data. Any earthquake catalogue is the result of signals recorded on a complex, spatially and temporally heterogeneous network of seismometers, processed by humans using a variety of software and assumptions. Consequently, the resulting seismicity record is far from being calibrated in the sense of a laboratory physical experiment. Thus, even the best earthquake catalogues are heterogeneous and inconsistent in space and time because of networks' limitations to detect signals, and are likely to show as many man-made changes in reporting as natural ones (*Habermann*, 1987, 1991; *Habermann and Creamer*, 1994; *Zúñiga and Wiemer*, 1999). Unraveling and understanding this complex fabric is a challenging yet essential task.

In this study, we address one specific aspect of quality control: The assessment of the magnitude of completeness, M_c, defined as the lowest magnitude at which 100% of the events in a space-time volume are detected (*Rydelek and Sacks*, 1989; *Taylor et al.*, 1990; *Wiemer and Wyss*, 2000). This definition is not strict in a mathematical sense and is connected to the assumption of a power-law behavior of the larger magnitudes. Below M_c, a fraction of events is missed by the network, because they are too small to be recorded on enough stations, because network operators decided that events below a certain threshold are not of interest, or, in case of an aftershock sequence, because they are too small to be detected within the Coda of larger events.

We compare methods to estimate M_c based on the assumption that for a given volume a simple power-law can approximate the frequency-magnitude distribution (FMD). The FMD describes the relationship between the frequency of occurrence and the magnitude of earthquakes (*Ishimoto and Iida*, 1939; *Gutenberg and Richter*, 1944):

$$\log_{10} N(M) = a - bM \tag{2.1}$$

where $N(M)$ refers to the frequency of earthquakes with magnitudes larger or equal than M. The b-value describes the relative size distribution of events. To estimate the b-value, a maximum-likelihood technique is the most appropriate measure:

$$b = \frac{\log_{10}(e)}{\langle M \rangle - (M_c - \frac{\Delta M_{bin}}{2})} \tag{2.2}$$

Here $\langle M \rangle$ is the mean magnitude of the sample and M_{bin} is the binning width of the catalogue (*Aki*, 1965; *Bender*, 1983; *Utsu*, 1999).

Rydelek and Sacks (2003) criticized *Wiemer and Wyss* (2000), who performed detailed mapping of M_c, for using the assumption of earthquake self-similarity in their methods. However, *Wiemer and Wyss* (2003) maintain that the assumption of self-similarity is in most cases well founded, and that breaks in earthquake scaling claimed by *Rydelek and Sacks* (2003) are indeed caused by temporal and spatial heterogeneity in M_c. The assumption that seismic events are self-similar for the entire range of observable events is supported by studies of, for example, *Seggern et al.* (2003) and *Ide and Beroza* (2001).

A 'safe' way to deal with the dependence of b- and a-values on M_c is to choose a large value of M_c, but this seems to be overly conservative. However, this approach decreases the amount of available data reducing spatial and temporal resolution and increasing uncertainties due to smaller sample sizes. Maximizing data availability while avoiding bias due to underestimated M_c is desirable; moreover, it is essential when one is interested in questions such as studying breaks in magnitude scaling (*Abercrombie and Brune*, 1994; *Knopoff*, 2000; *Taylor et al.*, 1990; *Seggern et al.*, 2003). Unless the space-time history of $M_c = M_c(x, y, z, t)$ is taken into consideration, a study would have to conservatively assume the highest M_c observed. It is further complicated by the need to determine M_c automatically, since in most applications, numerous determinations of M_c are needed when mapping parameters such as seismicity rates or b-values (*Wiemer and Wyss*, 2000; *Wiemer*, 2001).

A reliable M_c determination is vital for numerous seismicity and hazard related studies. Transients in seismicity rates, for example, have increasingly been scrutinized as they are closely linked to changes in stress or strain, for example static and dynamic triggering phenomena (e. g. , *Gomberg et al.*, 2001; *Stein*, 1999). Other examples of studies that are sensitive to M_c are scaling related investigations (*Main*, 2000; *Knopoff*, 2000) or aftershock sequences (*Enescu and Ito*, 2002; *Woessner*

et al., 2004a). In our own work on, for example, seismic quiescence (*Wiemer and Wyss*, 1994; *Wyss and Wiemer*, 2000), b-value mapping (*Wiemer and Wyss*, 2002; *Gerstenberger et al.*, 2001), and time-dependent hazard (*Wiemer*, 2000), we often found M_c to be the most critical parameter of the analysis. Knowledge of $M_c(x, y, z, t)$ is important, because a minute change in M_c of $M_c = 0.1$ leads (assuming $b = 1.0$) to a 25% change in seismicity rates, a change of $M_c = 0.3$ to a factor of two.

The requirements for an algorithm to determine M_c in our assessment are: (1) to calculate M_c automatically for a variety of datasets; (2) to give reliable uncertainty estimates; (3) to conserve computer time. We specifically limit our study to techniques based on parametric data of modern earthquake catalogues. A number of researchers have investigated detection capability by studying signal to noise ratios at particular stations (*Gomberg*, 1991; *Kvaerna et al.*, 2002a,b); however, these waveform based techniques are generally too time-consuming to be practical for most studies. We also focus on recent instrumental catalogues, ignoring the question of how to best determine M_c in historical datasets commonly used in seismic hazard assessment (*Albarello et al.*, 2001; *Faeh et al.*, 2003). In order to evaluate the performance of the different algorithms, we use synthetically created, regional and global data sets.

We believe that the review and comparison of adaptable methods presented in this study, and the introduction of uncertainties in M_c, are an important contribution for improving seismicity related studies.

2.3 Data

For the comparison of methods to determine M_c, we chose subsets of six different catalogues with diverse properties. The catalogues analyzed are freely available

from the websites of the specific agencies:

- Regional catalogue: We selected a subset of the Earthquake Catalogue Of Switzerland (ECOS) of the Swiss Seismological Service (SSS) in the southern province Wallis for the period $1992 - 2002$ (Figure 2.1A), providing a local magnitude M_L (*Deichmann et al.*, 2002).
- Regional catalogue: We chose a subset of the Northern California Seismic Network (NCSN) catalogue focused on the San Francisco Bay-area for the period $1998 - 2002$ using the preferred magnitude (Figure 2.1B).
- Volcanic region: We use a subset of the earthquake catalogue maintained by the National Research Institute for Earth Science and Disaster Prevention (NIED) reporting a local magnitude M_L. The subset spans a small volcanic region in the Kanto province for the period $1992 - 2002$ (Figure 2.1C).
- Aftershock sequence: We selected a seven year period ($1992.49 - 1999.49$) from the Landers 1992 $M_W = 7.3$ aftershock sequence using the earthquakes recorded by the Southern California Seismic Network (SCSN), a cooperative project of Caltech and the U.S. Geological Survey, distributed through the Southern California Earthquake Data Center (SCEDC) reporting a local magnitude M_L (Figure 2.1D).
- Global datasets:
    a. the Harvard CMT catalogue, reporting the moment magnitude M_W, is used for the time period $1983 - 2002$. Only shallow events ($d \leq 70\text{km}$) are used for mapping purposes.
    b. the ISC catalogue is analyzed for the period $1980-2000$ and magnitudes $m_b \geq 4.3$. Only shallow events ($d \leq 70\text{km}$) are used. The cut-off magnitude was chosen due to the temporal heterogeneity of the catalogue. Surface wave magnitudes are taken to equal m_b in case there is none.

From this point on, we refer to the generic expression 'magnitude' which corresponds to the magnitude of the respective earthquake catalogue outlined above.

2.4 Methods

Methods to estimate the magnitude of completeness of earthquake catalogues are based on two fundamentally different assumptions. Most methods assume self-similarity of the earthquake process, which consequently implies a power-law distribution of earthquakes in the magnitude and in the seismic moment domain. One other approach relies on the assumption that the detection threshold due to noise decreases during nighttime, thus the magnitude of completeness is determined using the day-to-night ratio of earthquake frequency (*Rydelek and Sacks*, 1989; *Taylor et al.*, 1990). In this study, we compare only methods assuming self-similarity of the earthquake process:

1. Entire-magnitude-range method (EMR) modified from *Ogata and Katsura* (1993)
2. Maximum curvature-method (MAXC) (*Wiemer and Wyss*, 2000)
3. Goodness-of-fit test (GFT) (*Wiemer and Wyss*, 2000)
4. M_c by b-value stability (MBS) (*Cao and Gao*, 2002)

These methods are described below and are illustrated schematically in Figure 2.2. The code is freely available together with the seismicity analysis software package ZMAP (*Wiemer*, 2001) which is written in Mathworks commercial software language Matlab® (*http://www.mathworks.com*).

EMR-method

We developed a method to estimate M_c that uses the entire data set, including the range of magnitudes reported incompletely. Our approach is similar to that of *Ogata and Katsura* (1993) and uses a maximum-likelihood estimator for a model that con-

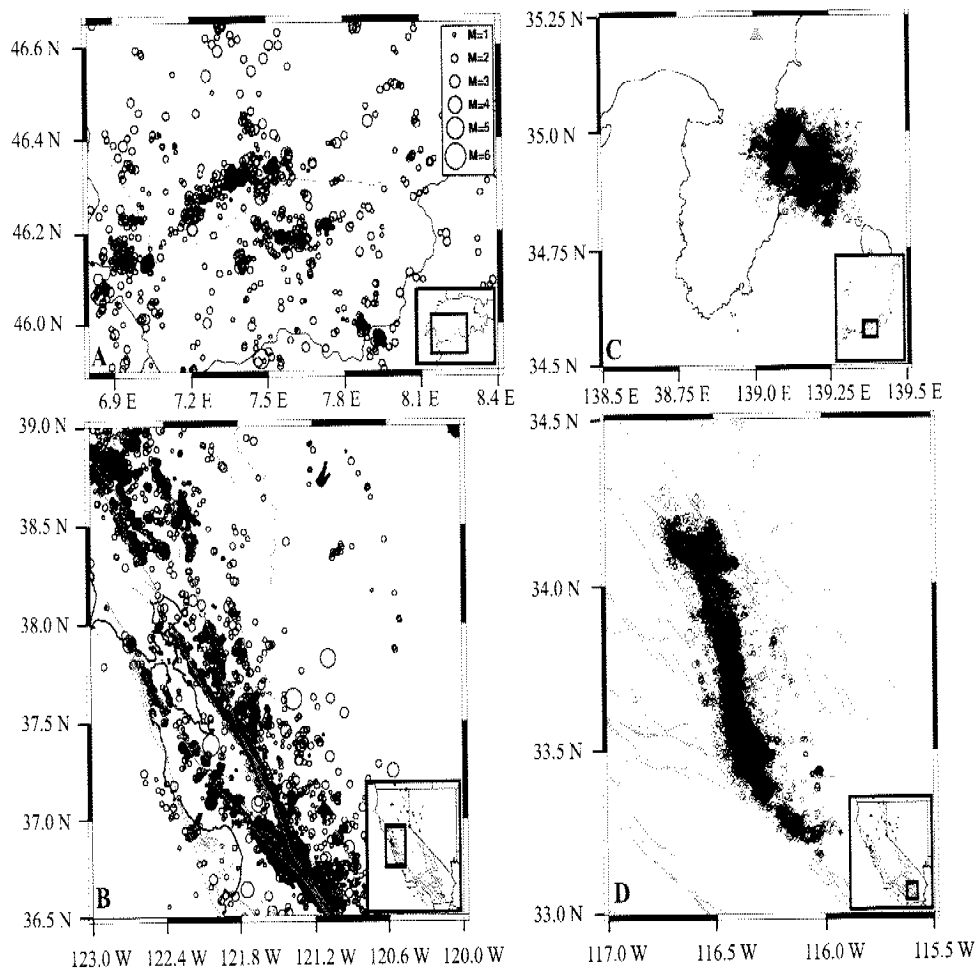

Figure 2.1: Earthquakes used in this study: A) Subset of the earthquake catalogue of Switzerland (ECOS) in the southern province Wallis, B) subset of the NCSN catalogue comprising the Bay area, C) subset of the NIED catalogue in the Kanto province with the triangles indicating volcanoes, and D) the Landers 1992 aftershock sequence from the SCSN catalogue. California maps display known faults in light gray.

sists of two parts: One to model the complete part and one to sample the incomplete part of the frequency-magnitude distribution (Figure 2.2). We use the entire magnitude range to obtain a more robust estimate of M_c especially for mapping purposes.

For data above an assumed M_c, we presume a power-law behavior. We compute a- and b-values using a maximum-likelihood estimate for the a- and b-value (*Aki*, 1965; *Utsu*, 1965). For data below the assumed M_c, a normal cumulative distribution function $q(M|\mu,\sigma)$ that describes the detection capability as a function of magnitude is fitted to the data. $q(M|\mu,\sigma)$ denotes the probability of a seismic network to detect an earthquake of a certain magnitude and can be written as:

$$q(M|\mu,\sigma) = \frac{1}{\sigma\sqrt{2\pi}} \int_{-\infty}^{M_c} \exp -\frac{(M-\mu)^2}{2\sigma^2} dM \quad \text{, for} \quad M < M_c \tag{2.3}$$

$$q(M|\mu,\sigma) = 1 \quad \text{, for} \quad M \geq M_c \tag{2.4}$$

μ is the magnitude at which 50% of the earthquakes are detected and σ denotes the standard deviation describing the width of the range where earthquakes are partially detected. Higher values of σ indicate that the detection capability of a specific network decreases faster. Earthquakes with magnitudes equal to or greater than M_c are assumed to be detected with a probability of one. The free parameters μ and σ are estimated using a maximum-likelihood estimate. The best fitting model is the one that maximizes the log-likelihood function for four parameters: μ and σ as well as a and b. As the negative log-likelihoods are computed, we changed the sign for display reasons so that the minimum actually shows the maximum likelihood estimate in Figure 2.2C. The circles in Figure 2.2B show the best fit for the dataset in Figure 2.2A.

We tested four functions to fit the incomplete part of real earthquake catalogues: three cumulative distribution functions (Exponential, Lognormal and Normal) and

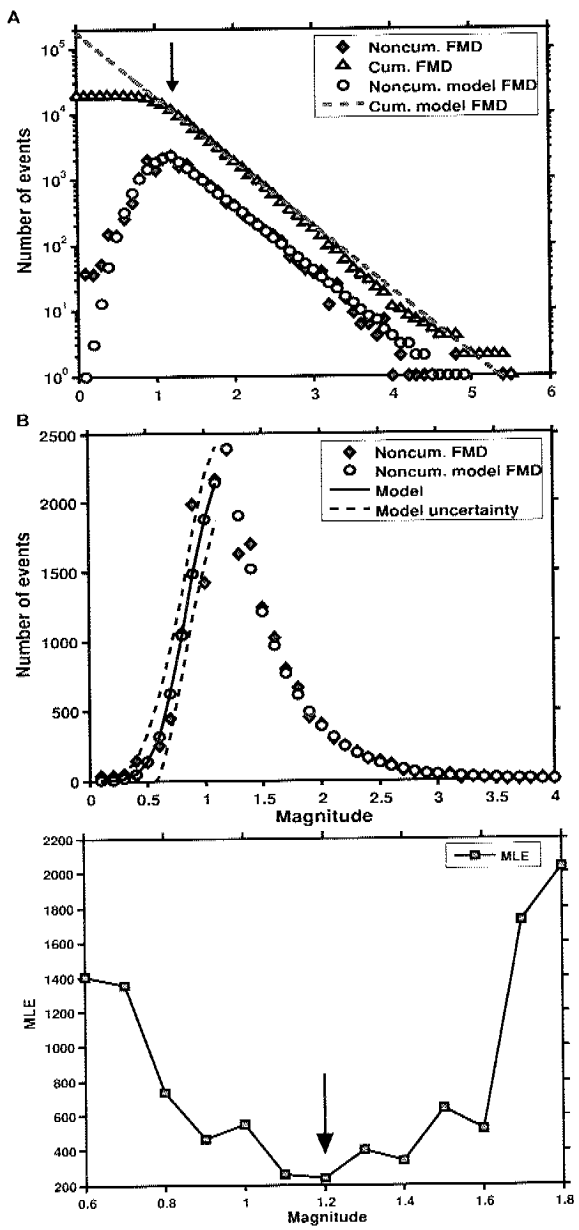

Figure 2.2: EMR-method applied to the NCSN-catalogue data (1998 – 2001): $M_c = 1.2$, $b = 0.98$, $a = 5.25$, $\mu = 0.73$, $\sigma = 21$. A) Cumulative and non-cumulative FMD and model on logarithmic scale with the arrow indicating Mc. B) Normal CDF fit (gray line) to the data below $M_c = 1.2$ on linear scale. Dashed gray line shows standard deviations of the model. Diamonds show original data, circles display non-cumulative FMD of EMR-model. C) Choice of the best model from the maximum-likelihood estimates denoted with an arrow pointing to the resulting M_c-value.

an exponential decay. The latter two cumulative distribution functions (CDF) are competitive when computing the likelihood score. However, the Normal CDF generally fits best the data from regional to worldwide earthquake catalogues compared to the other functions.

The EMR-method creates a comprehensive seismicity model. To evaluate if this model is acceptable compared to the actual data, we adopt a Kolmogorov-Smirnov-test (KS-test) at the 5% significance level to examine the goodness-of-fit (*Conover*, 1999). The test assumes that the two samples are random and mutually independent. The null-hypothesis H_0 of the test is that the two samples are drawn from the same distribution.

Maximum curvature (MAXC)

Wiemer and Wyss (2000) proposed two methods based on the assumption of self-similarity. A fast and reliable estimate of M_c is to define the point of the maximum curvature (MAXC) as magnitude of completeness by computing the maximum value of the first derivative of the frequency-magnitude curve. In practice, this matches the magnitude bin with the highest frequency of events in the non-cumulative frequency-magnitude distribution as indicated in Figure 2.3A. Despite the easy applicability and relative robustness of this approach, M_c is often underestimated especially for gradually curved frequency-magnitude distributions that result from spatial or temporal heterogeneities.

Goodness-of-fit test (GFT)

The GFT-method to calculate M_c compares the observed frequency-magnitude distribution with synthetic ones (*Wiemer and Wyss*, 2000). The goodness-of-fit is computed as the absolute difference of the number of events in the magnitude bins between the observed and synthetic Gutenberg-Richter distribution. Synthetic distributions are calculated using estimated a- and b-values of the observed dataset for

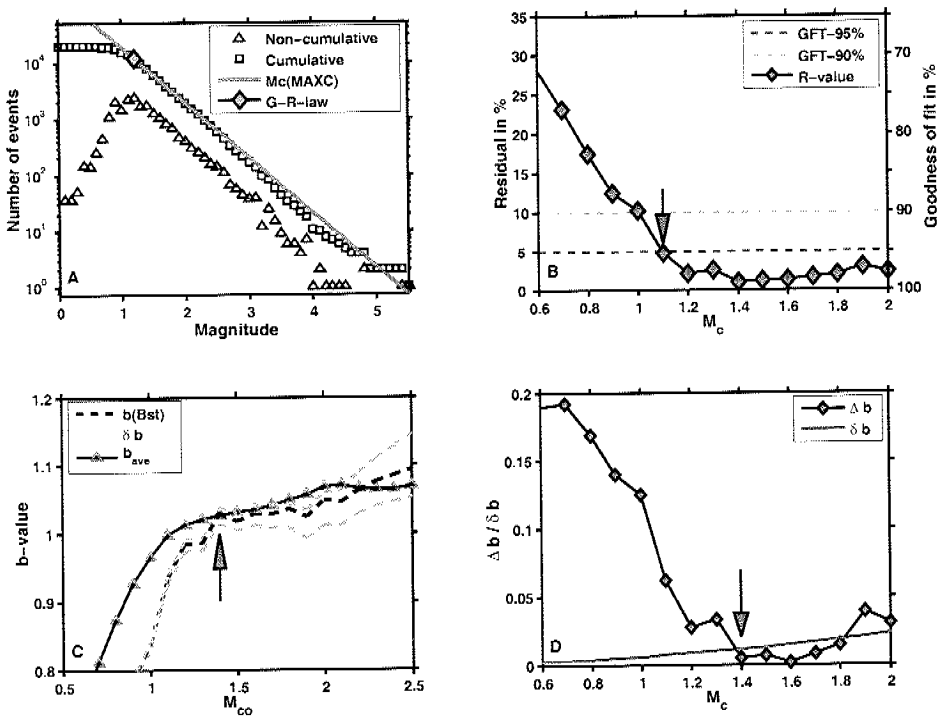

Figure 2.3: A) Frequency-magnitude distribution of the subset of the NCSN catalogue. The result of the MAXC-approach is indicated with a diamond. B) Residuals and goodness-of-fit value R for the GFT-method. R is the difference between the observed and synthetic FMDs, as a function of M_c. Dashed horizontal lines indicate at which magnitudes 90% and 95% of the observed data are modeled by a straight line fit. C) b, b_{ave} and the uncertainties δb as a function of cut-off magnitude M_{co} for the MBS-approach. The decision criterion is displayed in panel D. D) Standard deviation δb and difference $\Delta b = |b - b_{ave}|$ as a function of M_{co}. M_c is defined at the cut-off magnitude for which $\Delta b \leq \delta b$ for the first time.

$M \geq M_{co}$ as a function of ascending cut-off-magnitudes M_{co}. R defines the fit in percentage to the observed frequency-magnitude distribution and is computed as a function of cut-off-magnitude. A model is found at an R-value at which a predefined percentage (90% or 95%) of the observed data is modeled by a straight line. Figure 2.3B shows a schematic example with the choice of M_c indicated by the arrow as the R-value falls below the horizontal line of the 95% fit. Note that it is not the minimum R-value that is chosen. The 95% level of fit is rarely obtained for real catalogues, the 90% level is a compromise.

M_c by b-value stability (MBS)

Cao and Gao (2002) estimate M_c using the stability of the b-value as a function of cut-off magnitude M_{co}. This model is based on the assumption that b-values ascend for $M_{co} < M_c$, remain constant for ($M_{co} > M_c$ and ascend again for $M_{co} >> M_c$. If $M_{co} << M_c$, the resulting b-value will be too low. As M_{co} approaches M_c, the b-value approaches its true value and remains constant for $M_{co} >> M_c$, forming a plateau (Figure 2.3C). These authors arbitrarily defined M_c as the magnitude for which the change in b-value $\Delta b(M_{co})$ of two successive M_{co} is smaller than 0.03. Testing this approach for mapping purposes, we found the criterion to be unstable since the frequency of events in single magnitude bins can vary strongly. To base the approach on an objective measure and to stabilize it numerically, we decided to use the b-value uncertainty according to *Shi and Bolt* (1982) as criterion

$$\delta b = 2.3b^2 \sqrt{\frac{\sum_{i=1}^{N}(M_i - \langle M \rangle)}{N(N-1)}} \tag{2.5}$$

with $\langle M \rangle$ being the mean magnitude and N the number of events. We define M_c as the magnitude at which $\Delta b = \mid b_{ave} - b \mid \leq \delta b$ (Figure 2.3D). b_{ave} is the arithmetic mean calculated from b-values of successive cut-off magnitudes in half a magnitude

range $dM = 0.5$:

$$b_{ave} = \frac{\sum_{M_{co}}^{M_{co}+0.5} b(M_{co})}{5} \tag{2.6}$$

for a bin size of 0.1. Note that the magnitude range dM to calculate b_{ave} is crucial. If one chose e.g. $dM = 0.3$, the resulting M_c can be very different from the one obtained using $dM = 0.5$. Large magnitude ranges are preferable and would be justified for frequency-magnitude distributions that perfectly obey a power-law. Figure 2.3C shows b, b_{ave} and b as a function of M_{co}. At $M_{co} = 1.4$, b_{ave} is within the uncertainty bounds of b (Figure 2.3D), thus $M_c = 1.4$.

Additional methods

Several other authors proposed additional methods to estimate the magnitude of completeness. Some of them are rather similar to the ones outlined above, one method is based on other assumptions. For the reasons described in the following, we did not add these methods to our comparison.

Kagan (2003) proposed a method fitting the empirical distribution of the observed data with the Pareto-law in the seismic moment domain using fixed β-values. The goodness-of-fit is computed applying a Kolmogorov-Smirnov-test. This approach is similar in concept to the GFT-method but applying a rigorous statistical test. However, we found this method to show instabilities when using a grid search technique to simultaneously fit b and M_c.

Marsan (2003) introduced a method computing the b-value and the log-likelihood of completeness for earthquakes above a certain cut-off magnitude. The log-likelihood of completeness is defined as the logarithmic probability that the Gutenberg-Richter law fitted to the data above the cut-off magnitude can predict the number of earthquakes in the magnitude bin just below the cut-off magnitude. The magni-

tude of completeness is chosen so that (1) the b-value drops for magnitudes smaller than M_c and (2) the log-likelihood drops at M_c. The method is similar to the MBS-method, but the two criteria are difficult to combine for automatic M_c calculations. Additionally, calculating the log-likelihood for only one magnitude bin bears instabilities as the frequencies of events in the magnitude bins vary strongly.

Rydelek and Sacks (1989) introduced a method to estimate M_c using a random walk simulation (Schuster's method). The test assumes 1) that earthquakes, at any magnitude level, follow a Poisson distribution; and 2) that due to higher, man-made noise-levels during daytime, M_c is higher at this time. The method requires that other non-random features in earthquake catalogues like swarms, aftershock sequences or mine blasts are removed in advance, implying that it is not useful for the determination of M_c if such features are present bearing strong limitations on the applicability (*Wiemer and Wyss*, 2003). In contrast to others, this method does not assume self-similarity of earthquakes which is the main reason not to include it in the comparison as we want to compare methods based on the same assumption.

Estimating the uncertainty of M_c and b

None of the aforementioned methods has yet explicitly considered the uncertainty in the estimate of M_c and its influence on the b-value. We use a Monte Carlo approximation of the bootstrap method (*Chernick*, 1999; *Efron*, 1979) to calculate the uncertainties δM_c and δb. This can be combined with all methods described in detail. Bootstrap sample earthquake catalogues are generated by drawing with replacement an equivalent amount of events from the original catalogue. For each of the bootstrap sample earthquake catalogues, M_c and b are calculated. The second moment of the evolving empirical distributions of M_c and b-values is defined as the uncertainty δM_c and δb, respectively.

Note that we use the mean values of the empirical distributions for M_c and

b as final result for automated mapping, not the ones from the single observed frequency-magnitude distribution. The bootstrap accounts for outliers and consequently smoothes the results spatially which is desirable for mapping purposes. When analyzing the FMD of single sub-volumes, one might use the results of the observed frequency-magnitude distribution. In general, bootstrapping itself was designed to estimate the accuracy of a statistic and not to produce a better point estimate, although there are a few exceptions to the rule (*Chernick*, 1999). However, we choose the mean value since the mean estimate considers aleatory uncertainties of the magnitude determination process. This implies that the frequency-magnitude distribution of a parametric earthquake catalogue is considered to be the best guess. We do not observe a significant bias of the estimated parameters to either higher or lower values computing the mean values for different types of earthquake catalogues.

2.5 Results

Sensitivity of the EMR-method

To quantify the sensitivity of the EMR-method to magnitude distributions that do not conform to the assumed Normal CDF, we designed synthetic catalogues that follow probabilities of the Normal CDF and of two other cumulative distribution functions for magnitudes smaller than the magnitude of completeness: the Weibull and the Lognormal CDF. All three distributions have the same number of free parameters. Magnitudes above $M_c = 1.5$ follow a Gutenberg-Richter law with $b = 1$.

For each of the three CDFs, a thousand possible synthetic distributions of magnitudes below M_c are computed, randomly varying the governing parameters of the CDFs. These parameters are constrained so that the probability of detecting events above $M_c \geq 1.5$ is close or equal to 1. For each of these catalogues, we apply the EMR-method to obtain M_c and the KS-test acceptance indicator H (Figure 2.4).

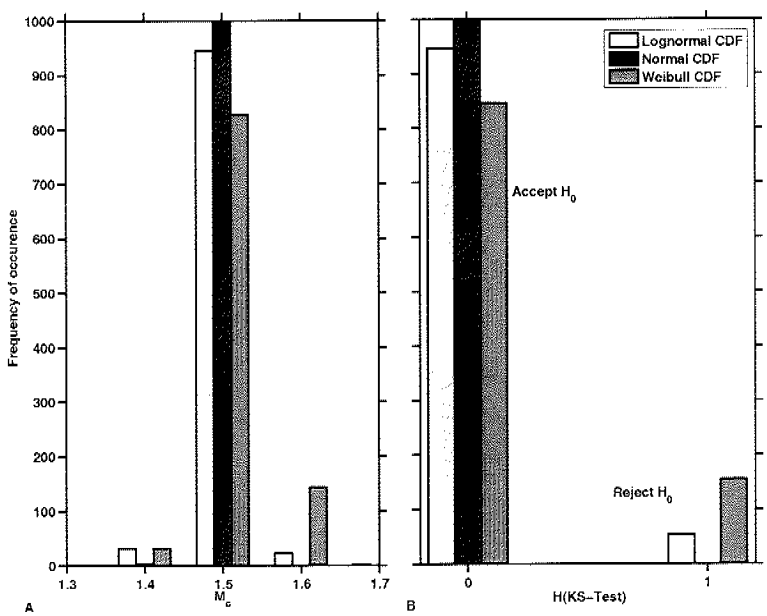

Figure 2.4: Histograms of A) M_c-distributions and B) KS-test acceptance indicator H for synthetic frequency-magnitude distributions randomly created using Normal, Lognormal and the Weibull CDFs below M_c. Second moments are small and the fractions of accepted models are high in all three cases. In detail, the second moments are $\delta M_c = 0.006$, $\delta M_c = 0.025$ and $\delta M_c = 0.040$ and the fractions of accepted models are 100%, 94.6% and 84.6% for the Normal, Lognormal and the Weibull CDF, respectively.

The result shows peaked distributions of M_c with small second moments $\delta M_c = 0.006$, $\delta M_c = 0.025$ and $\delta M_c = 0.040$ for the Normal, Lognormal and the Weibull CDF, respectively. The KS-test results reveal that the seismicity model is accepted 100% for the Normal CDF, 94.6% for the Lognormal and 84.6% for the Weibull CDF. Thus, the EMR-method based on the Normal CDF creates a magnitude distribution that resembles the original distribution and results in a good fit even though the magnitude distribution violates a basic assumption.

Comparing the methods - dependence on the sample size

We first analyze the dependence of M_c on the sample size S, i.e. number of events, for the different methods. A synthetic catalogue with $M_c = 1$ and $b = 1$ is used: the incomplete part below M_c was modeled using a Normal CDF q with $\mu = 0.5$ and $\sigma = 0.25$. From the synthetic dataset random samples of ascending size $20 \leq S \leq 1000$ are drawn and M_c as well as b are computed. For each sample size, this procedure is repeated for $N = 1000$ bootstrap samples.

In general, we expect from each approach to recover the predefined $M_c = 1.0$ and the uncertainties M_c to decrease with an increasing amount of data. The EMR-method is capable of recovering $M_c = 1.0$ well (Figure 2.5A). The MBS-approach underestimates M_c substantially for small sample sizes ($S \leq 250$) and shows the strongest dependence on sample size (Figure 2.5B). Both, the MAXC- and GFT95-approach (Figure 2.5C and D) underestimate M_c by about 0.1 with MAXC consistently calculating the smallest value. Apart from the MBS-approach, δM_c shows the expected decrease with increasing sample size S. Uncertainties of the EMR-approach decrease slightly for $S \leq 100$ probably due to the limited data set. The uncertainties δM_c vary between 0.2 and 0.04 and are smaller for the MAXC-approach, on average almost half the size of the uncertainties computed for the GFT95%- and EMR-uncertainties. In case of the MBS-approach, the increasing number of sam-

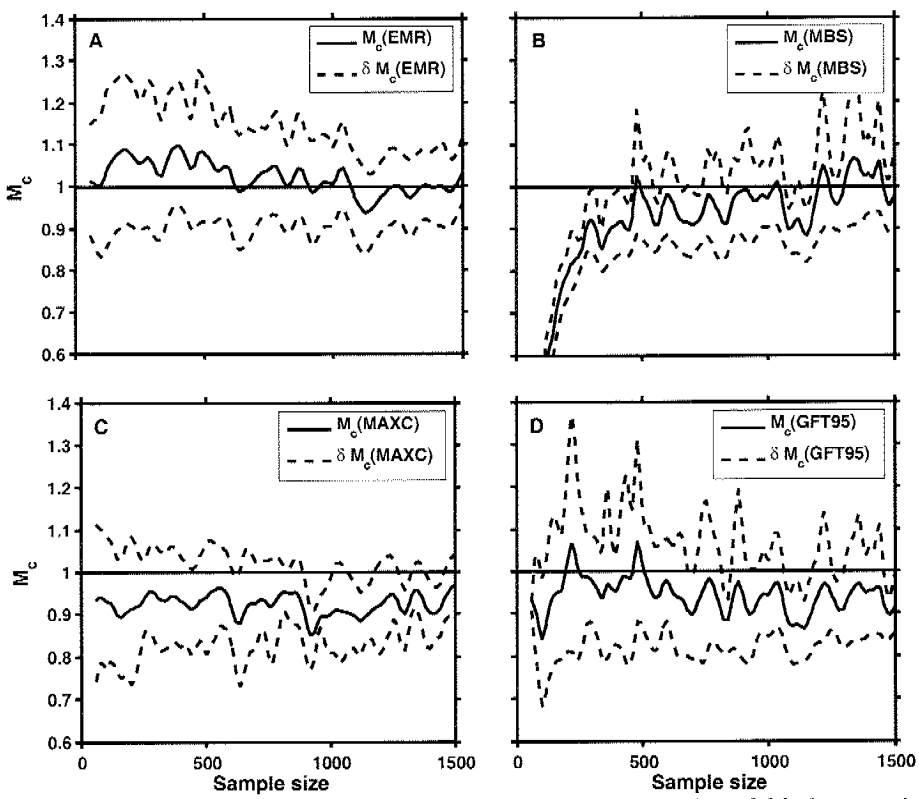

Figure 2.5: M_c as function of the sample size used for the determination of M_c for a synthetic catalogue. The synthetic catalogue was created with $M_c = 1$ and $b = 1$ and $\mu = 0.5$ and $\sigma = 0.25$ for the NCDF. Each subplot displays the mean M_c-values and the uncertainty $M_c \pm \delta M_c$ for A) the EMR-approach, B) the MBS-approach, C) the MAXC-approach, and D) the GFT95-method. Note that the uncertainties decrease with increasing sample size for all methods except for the MBS-approach.

ples result in a decrease of the uncertainty δb calculated using equation (2.5) (*Shi and Bolt*, 1982). Consequently, the criterion $\Delta b = \mid b_{ave} - b \mid \leq \delta b$ becomes stricter and in turn results in higher uncertainties for the M_c determination.

We infer that reliable estimates for M_c can only be obtained for larger sample sizes. However, M_c estimates of the MAXC- and EMR-approach result in reasonable values that could be used in case of small datasets. From our investigations, we assume that $S \geq 200$ events are desirable as a minimum sample size S. We are aware of the fact that it is not always possible to achieve this amount when spatially and temporally mapping M_c. For smaller quantities, we suggest further statistical tests for the significance of the results, e.g. when addressing b-value anomalies (*Schorlemmer et al.*, 2003).

We also addressed the question of how many bootstrap samples are needed to obtain reliable estimates of uncertainties. While *Chernick* (1999) proposes $N = 100$ bootstrap samples as adequate to establish standard deviations but recommends to use $N = 1000$ depending on available computing power, we find that our results stabilize above $N = 200$.

Comparing the methods - real catalogues

We apply the bootstrap approach to compare the performance of the different methods for a variety of earthquake catalogues. For the comparison, M_c and b-values are calculated simultaneously for $N = 500$ bootstrap samples. Figure 2.6 illustrates the results in two panels for catalogues of the SSS (A, B), the NCSN (C, D), the NIED (E, F), and the Harvard CMT catalogue (G, H): For each catalogue, b-value vs. M_c plots are shown with each marker indicating the mean values for M_c and b as well as the uncertainties δM_c and δb displayed as error bars. The additional panels show the cumulative and non-cumulative frequency-magnitude distributions of the catalogue. Table 2.1 summarizes the results.

The comparison exhibits a consistent picture across the different data sets, which also agrees with the results obtained in Figure 2.4 for the synthetic distribution. However, in contrast to the synthetic distribution we do not know the 'true' value of M_c in these cases, thus we render a relative evaluation on the performance of the algorithms. While uncertainties across the methods are in the same order of magnitude for both δb and δM_c, respectively, the individual estimates of M_c and b are not consistent. The MBS-method leads to the highest M_c values whereas the MAXC- and the GFT90%-approach appear at the lower limit of M_c. The EMR-approach shows medium estimates of both parameters while estimates of the GFT95%-approach vary strongest. In case of the Harvard CMT catalogue the GFT95%-approach does not show a result since this level of fit is not obtained. The MBS-approach applied to the NIED- and Harvard-CMT catalogue finds $M_c = 1.96$ and $M_c = 6.0$, respectively, much higher than the average values of $M_c \approx 1.2$ and $M_c \approx 5.35$ determined by the other methods. This results from the fact that b as a function of magnitude does not show a plateau region as expected in theory (compare to Figure 2.2C).

Catalogue	SSS[1]	NCSN[2]	NIED[3]	Harvard[4]
No. of events	988	19559	30882	16385
M_c(EMR)	1.5 ± 0.13	1.20 ± 0.07	1.25 ± 0.05	5.39 ± 0.04
b(EMR)	0.96 ± 0.07	0.98 ± 0.02	0.81 ± 0.02	0.89 ± 0.01
M_c(MAXC)	1.36 ± 0.07	1.2 ± 0.0	1.2 ± 0.0	5.31 ± 0.03
M_c(GFT90)	$1.31 + 0.07$	1.07 ± 0.04	1.07 ± 0.04	5.3 ± 0.00
M_c(GFT95)	1.58 ± 0.12	1.12 ± 0.04	1.12 ± 0.04	–
M_c(MBS)	1.64 ± 0.11	1.44 ± 0.12	1.44 ± 0.12	5.94 ± 0.34

Table 2.1: Number of events, M_c and b-values together with their uncertainties determined for the data used in Figure 2.6. Shortcuts and Polygons: [1]Swiss Seismological Service (6.8°E – 8.4°E, 45.9°N – 46.65°N), [2]Northern California Seismic Network (123°W – 120.5°W, 36°N – 39.0°N) , [3]National Research Institute of Earth Science and Disaster Prevention (138.95°E – 139.35°E, 34.08°N – 35.05°N), [4]Harvard Centroid Moment Tensor. M_c(GFT95) could not be determined for the Harvard CMT catalog.

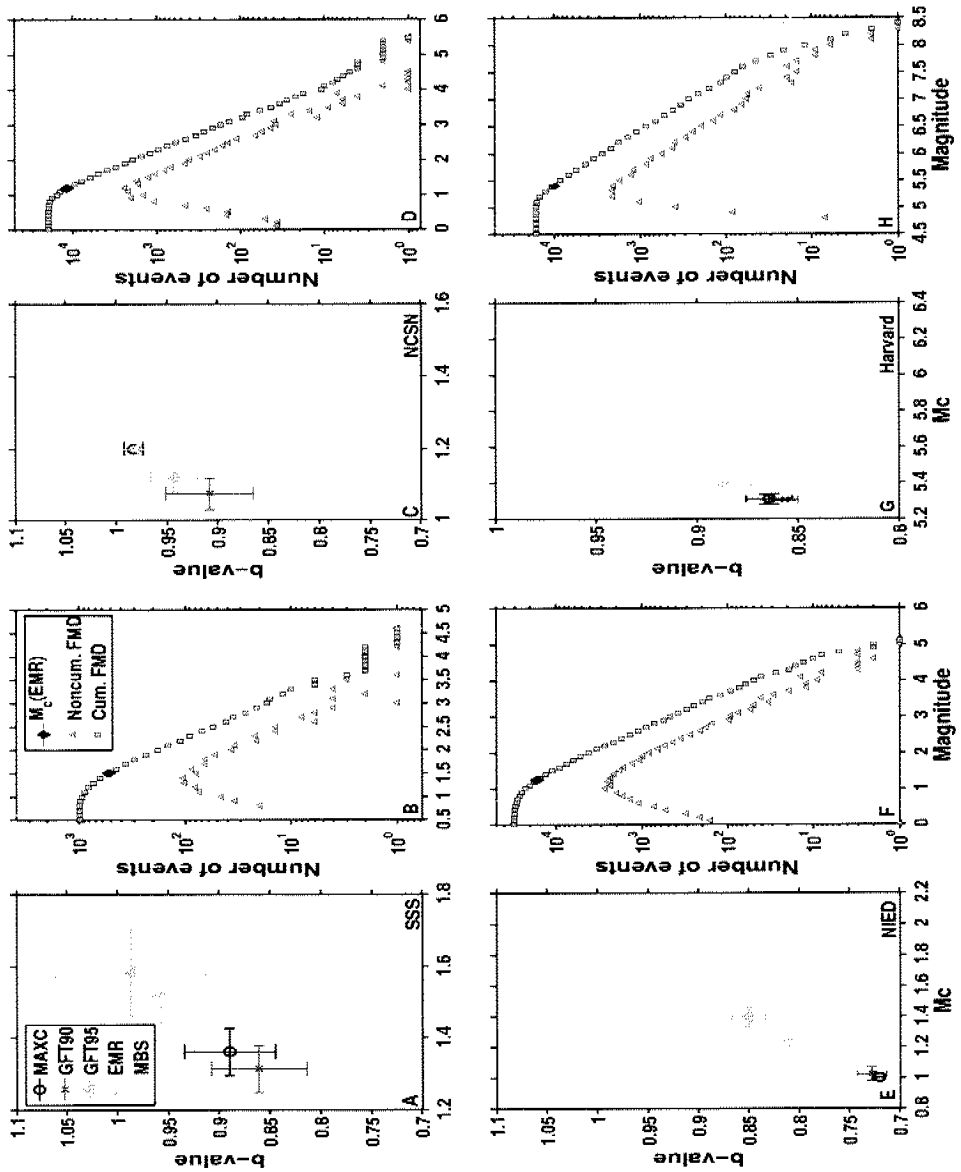

Figure 2.6: M_c and b-values combined with bootstrap uncertainties indicated as error bars and the corresponding FMDs of four catalogues: 1) Regional catalogue: subset of the ECOS catalogue of the SSS in the Wallis province of Switzerland (A, B), 2) Regional catalogue: subset of the NCSN-catalogue in the San Francisco Bay area (C, D), 3) Volcanic area in the Kanto province taken from the NIED-catalogue (E, F), 4) Global catalogue: Results using the Harvard CMT catalogue, no M_c(GFT95) determined (G,H). Comparing the results in all panels, MAXC and GFT90 tend to small, MBS to high, and EMR to medium M_c-values. Results from the GFT95-method reveal no clear tendency. Results are listed in Table 2.1.

2.6 Case studies

M_c and b as a function of time: The Landers aftershock sequence

M_c and b-values vary in space and time. Aftershock sequences provide excellent opportunities to study the behavior of the M_c determination algorithms in an environment of rapid M_c changes (*Wiemer and Katsumata*, 1999). A reliable estimate of the magnitude of completeness in aftershock sequences is essential for a variety of applications, such as aftershock hazard assessment, determining modified Omori-law parameters, and detecting rate changes. We investigate the aftershock sequence of the June 28, 1992 $M_W = 7.3$ Landers earthquake consisting of more than 43500 events in the 7 years following the mainshock ($M_L \geq 0.1$). We selected data in a polygon with a NW-SE extension of about 120 km and a lateral extension of up to 15 km on each side of the fault-line. This sequence was investigated by *Liu et al.* (2003); *Ogata et al.* (2003); *Wiemer and Katsumata* (1999); however uncertainties and temporal variations have yet not been taken into account.

We reevaluate the temporal evolution of M_c for the entire sequence, the northernmost and southernmost 20 km of the Landers rupture. To create the time series, we chose a moving window approach with a window size of $S = 1000$ events to compute parameters while moving the window by 250 events for the entire sequence. For the subregions, we used $S = 400$ and shifted the window by hundred events. We also analyzed the entire sequence for smaller sample sizes of $S = 400$, which showed slightly higher estimates of M_c, particularly right after the mainshock, but well in the uncertainty bounds of using $S = 1000$ samples.

$M_c(\mathrm{EMR})$ and its uncertainty values are plotted as light gray lines in the background (Figure 2.7). Disregarding the first four days, values for the entire sequence (Figure 2.7A) vary around $M_c(\mathrm{EMR}) = 1.61 \pm 0.1$ ($M_c(\mathrm{MAXC}) = 1.52 \pm 0.07$), values in the northern part vary around $M_c(\mathrm{EMR}) = 1.84 \pm 0.135$ compared to

$M_c(\mathrm{MAXC}) = 1.71 \pm 0.09$ (Figure 2.7B). In the southern part (Figure 2.7C), values vary around $M_c(\mathrm{EMR}) - 1.54 \pm 0.15$ ($M_c(\mathrm{MAXC}) = 1.37 \pm 0.10$). The comparison reveals that M_c-values are largest in the northern part of the rupture zone and smallest in the south. The MAXC-approach used in *Wiemer and Katsumata* (1999) underestimated M_c on average by 0.2.

Globally mapping M_c

On a global scale, we apply the EMR-method to the Harvard CMT and the MAXC-method ISC catalogue (Figure 2.8). *Kagan* (2003) analyzed properties of global earthquake catalogues and concluded that the Harvard CMT catalogue is reasonably complete for the period $1977 - 2001$ with a magnitude threshold changing between $M_W = 5.7$ before 1983 to about $M_W = 5.4$ in recent years. He analyzed variations of M_c as a function of earthquake depth, tectonic provinces, and focal mechanisms. We exclude the early years before 1983 as those years show a higher M_c and significantly fewer earthquakes (*Kagan*, 2003; *Dziewonski et al.*, 1999). We apply the EMR-approach to map M_c for the Harvard CMT. In case of the more heterogeneous ISC-catalogue, we cut the catalogue at $M \geq 4.3$ and apply the MAXC-approach. This is necessary because the ISC includes reports from regional networks and we seek to evaluate the completeness of the catalogue comparable to the Harvard CMT catalogue. We do not consider different focal mechanisms and limit our study to seismicity in the depth range $d \leq 70\,\mathrm{km}$. The differentiation of tectonic provinces is implicitly included when mapping M_c on an equally spaced grid ($2^\circ \times 2^\circ$ degrees).

The Harvard CMT catalogue for the period $1983 - 2002$ in the depth range $d \leq 70\,\mathrm{km}$ contains a total of about 12650 events. We use a constant radius of $R = 1000\,\mathrm{km}$ to create sub-catalogues at each grid node and $N_{Bst} = 200$ bootstrap samples to calculate uncertainties. We require $N_{min} = 60$ events per node due to the sparse dataset. About 60% of the nodes have sample sizes between $60 \leq N \leq 150$

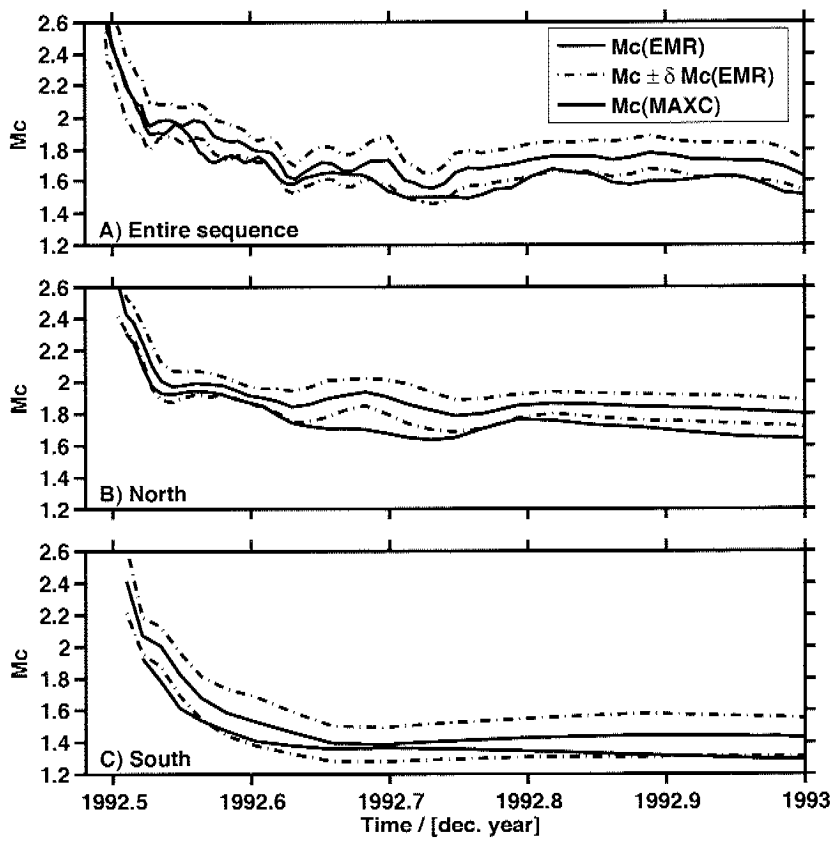

Figure 2.7: M_c as a function of time for A) the entire 1992 Landers aftershock sequence, B) the northernmost (20km) aftershocks of the rupture zone, and C) the southernmost (20km) aftershocks. M_c(EMR) and δM_c(EMR) are plotted as gray lines, results of the MAXC-approach as black lines. M_c for the entire sequence shows average values compared to the results obtained for limited regions.

events. The magnitude ranges ΔM for single nodes vary in between $1 \leq M \leq 3$. The ISC-catalogue in the period $1983 - 2000$ ($M \leq 4.3$) contains about 83000 events. As more data is available, we chose $R = 900$km, $N_{Bst} = 200$, $N_{min} = 60$. Here, only about 5% of the grid nodes have fewer than $N = 150$ events, the magnitude ranges also vary between $1 \leq M \leq 3$. We admit that the choice of parameters for the Harvard CMT catalogue is at a very low margin, but for coverage purposes a larger N_{min} is not suitable. The smaller amount of data reduces the capabilities to obtain a good fit in the magnitude range below the magnitude of completeness.

M_c(EMR) varies for the Harvard CMT catalogue in general around $M_c = 5.6$ (Figure 2.8A). The lowest values of approximately $5.3 \leq M_c \leq 5.5$ are observed spanning the circum-pacific region from Alaska and the Aleutians down to New Zealand and to the islands of Java and Indonesia. The west coast of North and South America shows slightly higher M_c-values ($M_c = 5.5 - 5.7$) with larger fluctuations. Uncertainties δM_c are in general small ($\delta M_c = 0.15$) as a consequence of sufficiently large datasets or peaked non-cumulative frequency-magnitude distributions (Figure 2.8B). The highest values of about $M_c \geq 5.8$ are obtained in the two red regions close to the Antarctica due sparse data ($N \leq 100$) probably as a consequence of poor network coverage, a small magnitude range of about $\Delta M = 1.2$ and a flat distribution of the non-cumulative frequency of magnitudes. These results correlate well with the larger uncertainty of $M_c \geq 0.2$. The Mid-Atlantic ridge is covered only between $\pm 25°$ latitude with M_c values primarily below $M_c \leq 5.6$.

The ISC catalogue shows in general lower completeness levels as the Harvard CMT catalogue. In continental regions, M_c varies between $4.3 \leq M_c 4.5$, whereas on the Atlantic ridges values fluctuate between $4.6 \leq M_c \leq 5.1$ (Figure 2.8C). Uncertainties δM_c display the same picture with values $M_c \leq 0.11$ in continental regions and higher values $0.12 \leq M_c \leq 0.35$ on Atlantic ridges and especially in

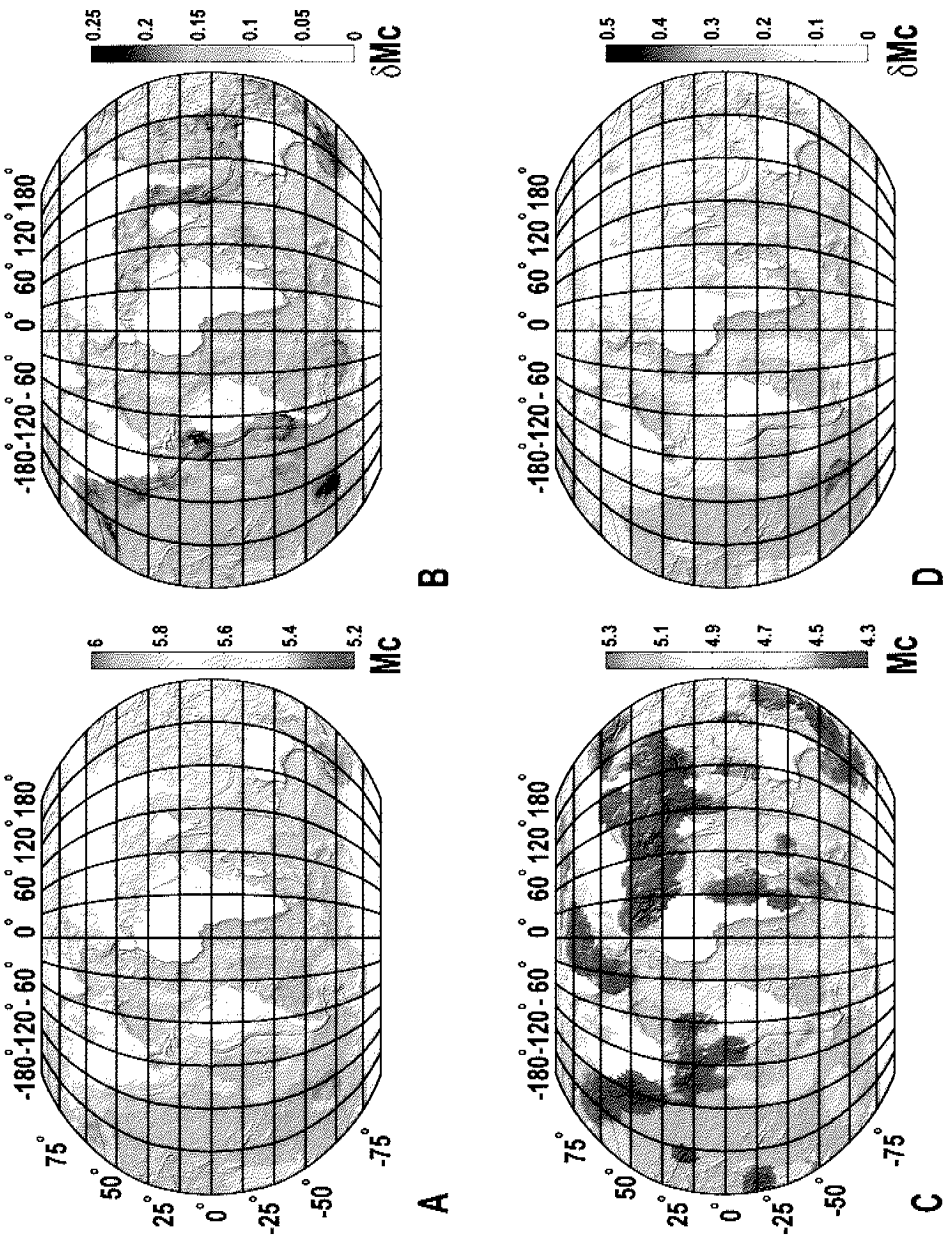

Figure 2.8: Global maps of M_c. Panels A and B illustrate M_c and δM_c using the Harvard CMT catalogue 1983 – 2002 for seismicity in the depth range $d \leq 70$ km, and constant radii $R = 1000$ km. The gray circles indicate the spots for which frequency-magnitude distributions are shown in Figure 2.9. Panels C and D display M_c and δM_c of the ISC catalogue ($M \geq 4$) for the time period 1980 – 2001 ($d \leq$ 70km, $R = 900$ km). M_c-values are calculated as the mean of $N = 200$ bootstrap samples using the EMR-method for the Harvard CMT catalogue and the MAXC-method for the ISC.

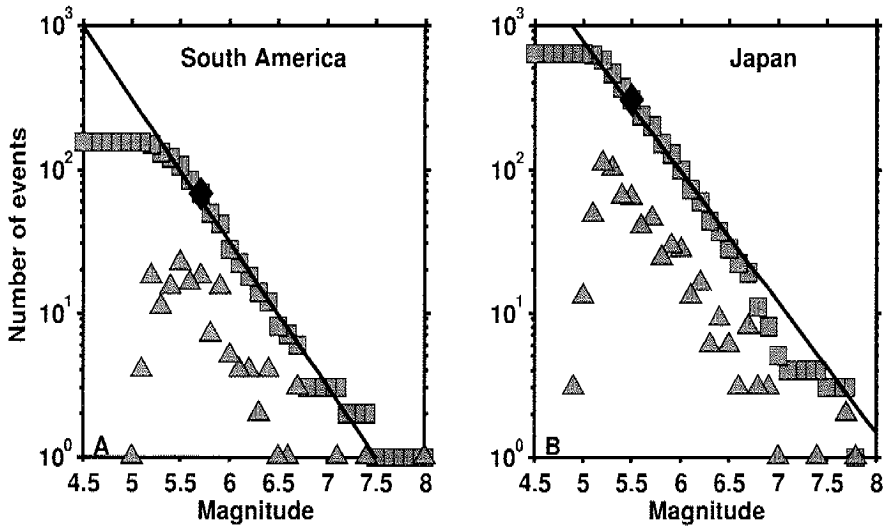

Figure 2.9: Cumulative and non-cumulative frequency-magnitude distributions from grid nodes indicated as gray circles in Figure 2.8A: A) South America (subduction/ ridge): a flat frequency-magnitude distribution leading to relatively high uncertainties $M_c(\mathrm{EMR}) = 5.7 \pm 0.15$, B) Japan: a 'peaked' frequency-magnitude distribution resulting in small uncertainties ($M_c(\mathrm{EMR}) = 5.5 \pm 0.06$).

the South Pacific near the Antarctica (Figure 2.8D). As the ISC is a combination of different catalogues, magnitudes had to be converted to be comparable and this might be the reason for larger uncertainties in certain regions.

Two examples from different tectonic regimes for regions in South America (subduction / spreading rigde) and Japan (subduction) illustrate aspects of the relation between FMDs, M_c and δM_c in Figure 2.9, respectively. Gray circles in Figure 2.8A show the respective locations. In case of Figure 2.9A for the South-American example the relatively flat frequency-magnitude distribution and small sample size ($N \leq 180$) leads to relatively high uncertainties in $M_c = 5.68 \pm 0.15$ (Figure 2.9A). A small uncertainty is found for the 'peaked' distribution in Figure 2.9B (Japan) where the small uncertainties $M_c = 5.47 \pm 0.06$ are also expected due to the large sample size.

2.7 Discussion

Finding the best approach to determining M_c

We introduced the EMR-method based on *Ogata and Katsura* (1993) to model the entire frequency-magnitude distribution with two functions, a normal cumulative distribution function and a Gutenberg-Richter power-law. M_c is based on maximum-likelihood estimates. The choice of the normal cumulative distribution function is based on visual inspection, modeling of a variety of catalogues as well as comparisons to other possible functions but not based on physical reasoning. Thus, cases exist for which the choice of another function might be more appropriate. However, synthetic tests endorse that estimates of M_c can be correct even if this assumption is violated (Figure 2.4).

Compared to other methods, the EMR-method maximizes the amount of data available for the M_c determination, which should serve to stabilize the M_c estimates; however, it also adds two additional free parameters. Results from our synthetic test (Figure 2.4 and 2.5) and case studies (Figures 2.6-2.8) confirm that $M_c(\mathrm{EMR})$ together with the bootstrap approach performs best of all methods investigated for automatic mapping, justifying the additional free parameters. From these results we believe that the EMR-method is indeed well capable of resolving M_c. It also has the additional benefit of delivering a complete seismicity model, which may be used in search for M_c changes, magnitude shifts or rate changes. However, EMR is time consuming compared to MAXC, which is especially important when mapping large regions with large numbers of bootstrap samples. Additionally, the approach should only be applied when the incomplete part of the catalogues is available. *Kagan* (2002) argued that the Normal CDF, acting as a thinning function on the Gutenberg-Richter law, may distort conclusions as the smaller earthquakes may not have statistical stability. We instead believe that using the algorithm we provide

minimizes the risk of questionable interpretations, especially because the fitting quality can be tested for using the Kolmogorov-Smirnov test.

Cao and Gao (2002) published a method based on the assumption that b-values stabilize above the magnitude of completeness (Figures 2.3C and D). We enhanced this approach by adding a criterion based on the b-value uncertainty to decide on the threshold, and by adding a smoothing window to ensure robust automatic fits. However, our synthetic tests showed that $M_c(\mathrm{MBS})$ depends strongly on the sample size (Figure 2.5B) and uncertainties are larger compared to other methods due to the linearity of the FMD. We found the method applicable only for regional catalogues. Note that the resulting $M_c(\mathrm{MBS})$ is always higher than other M_c estimates (Figure 2.6). In summary, we conclude that $M_c(\mathrm{MBS})$ cannot be used for automatic determination of $M_c(\mathrm{MBS})$, but spot-checking b as a function of the cut-off magnitude M_{co} (Figure 2.3) can give important clues about M_c and b.

The MAXC-approach and the GFT-approach (*Wiemer and Wyss*, 2002) tend to underestimate the magnitude of completeness. This is found in our synthetic catalogue analysis (Figure 2.5), confirmed in the analysis of various catalogues (Figure 2.6) and for the case study of the Landers aftershock sequence (Figure 2.7). The advantage of $M_c(\mathrm{MAXC})$ is that results can be obtained with low computational effort, for small sample sizes and in pre-cut catalogues. $M_c(\mathrm{GFT})$ on the other hand shows a smaller systematic bias; however, it is slightly more computational intensive and not robust for small sample sizes $S < 200$.

The application of the EMR- and MAXC-approaches to the 1992 Landers aftershock sequence shows that M_c were slightly underestimated by 0.2 in *Wiemer and Katsumata* (1999) (Figure 2.7). The reevaluation displays the importance of the spatial and temporal assessment of M_c as it has proven to be a crucial parameter in a variety of studies especially when working on near real-time time-dependent

hazard estimates for daily forecasts (*Gerstenberger*, 2004).

We applied a gridding technique rather than assuming predefined Flinn-Engdahl regions (*Kagan*, 1999; *Frohlich and Davis*, 1993) to map M_c for global catalogues (Figure 2.8). The maps reveal considerable spatial variations in M_c on a global scale in both the Harvard CMT ($5.3 \leq M_c \leq 6.0$) and ISC catalogue ($4.3 \leq M_c \leq 5.0$).

The overall M_c values we compute, for example, for the entire Harvard catalog ($M_c = 5.4$, Figure 6) are often lower than the maximum value found when mapping out M_c in space and/or time. Technically, one might argue that the overall completeness cannot be lower than any of its subsets. Given that in the seconds and minutes after a large mainshocks such as Landers, even magnitude 6 events may not be detectable in the Coda of the mainshock, for practical purposes completeness is best treated not in this purist view 100% completeness can never be established. The contribution of the relatively minor incomplete subsets, such as the regions with high M_c in the southern hemisphere (Figure 2.8) are generally not relevant when analyzing the overall behavior of the catalogue. Such subsets, however, need to be identified when analyzing spatial and temporal variations of seismicity parameters, highlighting the importance of the presented quantitative techniques to map M_c.

2.8 Conclusion

We demonstrated that the EMR-method is the most favorable choice to determine M_c because the method is stable under most conditions, because a comprehensive seismicity model is computed and because the model fit can be tested. We conclude that:

- for automated mapping purposes, the mean value of the N bootstrapped M_c determinations is a suitable estimate of M_c because it avoids outliers and smoothes the results;

- the bootstrap approach to determine uncertainties in M_c is a reliable method;
- for a fast analysis of M_c, we recommend using the MAXC-approach in combination with the bootstrap and add a correction value, for example $M_c = M_c(\mathrm{MAXC}) + 0.2$. This correction factor can be determined by spot-checking individual regions and is justified by the analysis of the synthetic catalogues.

2.9 Acknowledgements

The authors would like to thank D. Schorlemmer, P. M. Mai, M. Wyss and J. Hauser for helpful comments to improve the manuscript and programming support. We are indebted to the associate editor J. Hardebeck and three anonymous reviewers for valuable comments that significantly enhanced the manuscript. We acknowledge the Northern and Southern Earthquake Data Centers distributing the catalogues of the Northern California Seismic Network (NCSN) and the Southern California Seismic Network (SCSN), the Japanese Meteorological Agency (JMA), the Swiss Seismological Service, the International Seismological Center and the Harvard Seismology Group for providing seismicity catalogues used in this study. Figure 2.1 was created using GMT (*Wessel and Smith*, 1991). This is contribution number 1372 of the Institute of Geophysics, ETH Zurich.

Chapter 3

The 1997 Kagoshima (Japan) Earthquake Doublet: A Quantitative Analysis of Aftershock Rate Changes

This chapter is published in Geophysical Research Letters.

J. Woessner, E. Hauksson, S. Wiemer, and S. Neukomm (2004), The 1997 Kagoshima (Japan) earthquake doublet: A quantitative analysis of aftershock rate changes, *Geophys. Res. Lett.*, **31**, L03605, doi:10.1029/2003GL018858.

3.1 Abstract

We quantitatively map relative rate changes for the aftershock sequence following the second mainshock of the 1997 earthquake doublet ($M_W = 6.1$, $M_W = 6.0$) in the Kagoshima province (Japan). Using the spatial distribution of the modified Omori law parameters for aftershocks that occurred during the 47.8 days between the two mainshocks, we forecast the aftershock activity in the next 50 days and compare it to the actually observed rates. The relative rate change map reveals four regions with statistically significant relative rate changes - three negative and one positive. Our analysis suggests that changes in static stress from the second

mainshock could explain the coseismic rate changes for off-fault aftershocks, but either unusual crustal properties or the presence of crustal fluids have contributed to the activation and deactivation of on-fault seismicity.

3.2 Introduction

Understanding how earthquakes are affected by sudden changes in the state of stress in their immediate vicinity provides insight into the relationship between static stress changes and earthquake occurrence. If aftershocks are in part caused by stress changes from their mainshock, changes in their rate may reflect alterations in the state of stress in their immediate vicinity. Recently, *Stein* (2003) provided a review of how adjacent earthquakes interact through static stress changes, invoking a combination of rate and state friction (*Dieterich*, 1994) and Coulomb Stress changes (*King et al.*, 1994). In particular, *Stein* (2003) and *Toda and Stein* (2003) suggested that the second mainshock of the 1997 Kagoshima earthquake sequence in Japan decreased the rate of off-fault aftershocks from the first mainshock due to a stress drop caused by the second main event.

The objective of our study is to confirm spatial changes in the rate of aftershocks following the second mainshock and to investigate whether or not these changes are statistically significant. Different from previous studies, we determine the spatial distribution of relative rate changes and establish their significance. Determining quantitatively the changes in microearthquake activity is difficult, especially when addressing rate decreases (*Wyss and Toya*, 2000). Establishing rate decreases within an aftershock sequence is both desirable, because the high seismicity rate allows detailed investigations, and challenging, because establishing the significance of a relative rate change is more complicated when embedded within exponentially decaying sequences rather than in a stationary Poissonian process.

The entire 1997 Kagoshima sequence is not easily fit with existing aftershock sequence models. *Ogata* (2001) investigated the first 47.8 days of the 1997 Kagoshima aftershock sequence using the earthquake catalog of the Japanese Meteorological Agency (JMA). He found that a two-stage Epidemic-Type Aftershock-Sequence-model (ETAS, *Ogata*, 1999, 2001) provides the best approximation although the overall goodness-of-fit throughout the period remains poor. Contrary to the modified Omori law, the ETAS-model considers the magnitude distribution of the aftershock sequence and therefore requires additional free parameters resulting in a limited forecast ability. We apply simpler modified Omori law type models to map the spatial distribution of aftershock sequence parameters because these models allow to compute a more accurate representation of the sequence than just modeling the entire sequence.

3.3 Data

The 1997 earthquake doublet in the northwestern part of the Kagoshima Prefecture, Kyushu, southern Japan, occurred on March 26^{th} ($M_W = 6.1, M_L = 6.5$) and May 13^{th}, 1997 ($M_W = 6.0, M_L = 6.3$). Both mainshocks were followed by rich aftershock sequences. The first mainshock ruptured unilaterally westward for 15km along a strike-slip fault striking N280°, while the second mainshock ruptured two orthogonal 7.5km long segments, with one being parallel to the first rupture (*Horikawa*, 2001). The hypocenters of the two mainshocks are approximately 5km apart, and the parallel rupture planes are approximately 3km apart (*Horikawa*, 2001, Figure 3.1).

We analyze the Kagoshima University catalog (KU) (*Miyamachi et al.*, 1999) from 1997.23 to 1997.55 containing about 7000 events in the study area (Figure 3.1). The KU catalog is preferable to the JMA catalog (about 3500 events), because it has a lower completeness level, relocated aftershocks locations, and contains twice as

many events. We use the JMA catalog only for cross-validation of our results.

We investigated the magnitude of completeness M_c as a function of time and space (*Wiemer and Katsumata*, 1999; *Wiemer and Wyss*, 2000). The spatial and temporal distribution of M_c is used to establish a lower cut-off magnitude ensuring that further analysis is not biased by incomplete data. In case of the KU catalog, we set the global minimum threshold at $M_c = 1.3$ as results generally fluctuate around $M_c = 1.2$ when mapping spatially. In the time series, M_c decreases rapidly from $M_c - 1.8$ down to around $M_c = 1.2$. The low detection level is partly explained by the installation of temporary stations (*Miyamachi et al.*, 1999). We also investigated the JMA catalog to determine an overall M_c value in the same manner and obtained a value of $M_c = 1.6$.

3.4 Method

To derive the relative rate change values Δ_{RC}, we developed the following procedure: First, we use the observed data of the learning period t_L to fit the parameters of four different models of aftershock decay to the aftershock sequence applying the maximum-likelihood method (*Ogata*, 1999). Second, the best fitting model is used to forecast aftershocks until the end of the forecast period t_F. Finally, relative rate changes are established at the end of the forecast period.

The basic model is the modified Omori law (*Utsu*, 1961):

$$n(t) = k(t + c)^{-p} \tag{3.1}$$

with $n(t)$ being the number of earthquakes occurring at time t. This is equal to the intensity function $\lambda(t)$ assuming that aftershocks are distributed according to a non-stationary Poisson process. k represents the productivity of the mainshock and depends on the lower magnitude threshold of the earthquake catalog. p is a mea-

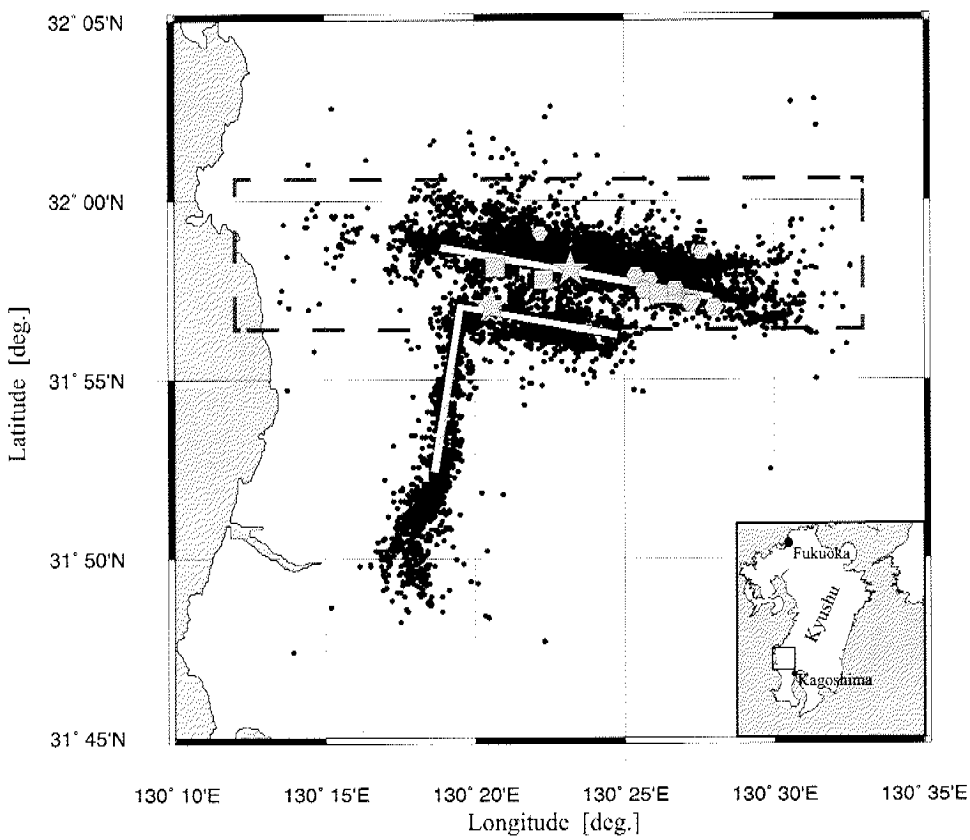

Figure 3.1: Map of the 1997 Kagoshima earthquake sequence. Fault ruptures are taken from *Horikawa* (2001), stars indicate the two mainshocks, aftershocks are displayed as squares ($5.0 \leq M_L \leq 6.0$) and hexagons ($4.0 \leq M_L \leq 5.0$). As background, the entire seismicity listed in the KU catalog is plotted as black dots. The dashed gray box frames the area shown in Figure 2.

sure for the exponential decrease of the aftershock rate and c describes a temporal offset that compensates for incomplete data at the beginning of the aftershock sequence. The other three models include one secondary aftershock sequence within the learning period and consist of two superimposed modified Omori laws. We limit our analysis to a maximum of two nested Omori sequences rather than including more complex point process models (*Vere-Jones*, 1995; *Ogata*, 1999; *Helmstetter and Sornette*, 2002) because we believe that simpler modified Omori law models are more suitable for computing forecasts at numerous nodes of a spatial grid. Forecasting the magnitude distribution as required applying an ETAS-model would greatly increase uncertainties.

The intensity function for these nested Omori models is written as:

$$\lambda(t) = \begin{cases} \lambda_1 = k_1(t+c_1)^{-p_1} & : \quad t \leq t_a \\ \lambda_2 = k_1(t+c_1)^{-p_1} + k_2(t+c_2)^{-p_2} & : \quad t_a \leq t \leq t_L \end{cases} \tag{3.2}$$

where t_a is the time of the largest aftershock from the mainshock time in the learning period. The indices 1 and 2 relate the modified Omori law parameters in the time periods t_a in the learning period, respectively.

In summary, we fit four models with increasing model complexity varying as a function of free parameters:

1. Model 1: Modified Omori law (MOL) (3 parameters: p, c and k)

2. Model 2: nested MOL (4 parameters: p, c, k1, k2)

3. Model 3: nested MOL (5 parameters: p1, p2, c, k1, k2)

4. Model 4: nested MOL (6 parameters: p1, p2, c1, c2, k1, k2).

The maximum-likelihood estimate (*Ogata*, 1999) for each model is computed by a constrained nonlinear grid search over the free parameter space, maximizing the

likelihood function. To find the best fitting model we use the corrected Akaike Information Criterion AIC_c (*Kenneth et al.*, 2002):

$$AIC_c = -2\max(\ln L) + 2P + \frac{2P(P+1)}{N-P-1} \tag{3.3}$$

with $\ln L$ being the likelihood function, P the number of free parameters and N the sample size. In contrast to the original AIC, the corrected AIC_c penalizes also for the amount of samples which becomes critical for small sample sizes. The AIC_c is useful in selecting the best model in the set; however, if all the models are poor, AIC_c still selects the one estimated to be best, but even that model may be poor in an absolute sense (*Kenneth et al.*, 2002). Thus, we estimate the goodness-of-fit for the selected AIC_c model to the observed data by applying a Kolmogorov-Smirnov-Test at a significance level of 0.05 (*Conover*, 1999). We do not use results for the interpretation of rate changes if even the best model is rejected (rejection level H equal to 1).

To establish the significance of a relative rate change, we need an estimate of the uncertainties of the model forecast at time t_F, which we derive based on a bootstrap approach (*Chernick*, 1999). The original dataset is bootstrapped 100 times, model parameters and forecasts are estimated for each bootstrap sample. From the empirical distribution of forecasted rates, we calculate the 2^{nd} moment as the uncertainty of our forecasts at time t_F. Thus, we include both, epistemic uncertainties by using different models and aleatory uncertainties due to the data. The relative rate changes can then be expressed as the ratio of the difference between the cumulative number of observed to forecasted events normalized by the 2^{nd} moment of the bootstrap forecasts

$$\Delta_{RC} = \frac{N_{(Obs}(t_F) - N_{Obs}(t_L)) - (\overline{N}(t_F) - \overline{N}(t_L))}{\sigma(N_{Bst}(t_F)} \tag{3.4}$$

N_{Obs} is the cumulative number of observed events, the cumulative number of forecasted events at the times t_L and t_F, $\sigma(N_{Bst}(t_F))$ the 2^{nd} moment of the bootstrap forecast at the end of the forecast period. The value Δ_{RC} expresses the normalized relative rate change between the observed and forecasted events. Positive values report an increase of the observed rate compared to the modelled rate of aftershock. We map Δ_{RC} spatially by covering the region with a rectangular grid and sampling events within radius R.

3.5 Results

Relative rate changes caused by the second mainshock ($M_L = 6.3$, 13 May 1997) show strong spatial variations with high statistical significance. The patterns are similar for both, the KU and the JMA catalog analyzed on evenly spaced grids of $0.002°$ and $0.005°$ degrees, respectively (Figure 3.2a and b). To evaluate the significance of the rate changes for the KU catalog, we determine the distribution of the best fitting model, and the rejection level H of the Kolmogorov-Smirnov-test as a measure for the goodness-of-fit (Figures 3.2c and d). Because the earthquakes exhibited mostly strike-slip faulting with a uniform depth distribution of aftershocks from 0 to 10km depth, we chose to show results in map view.

We identify four regions that exhibit significant rate changes (Figure 3.2a). The detailed temporal development of aftershock activity for four representative grid nodes is shown in Figure 3.3. The largest relative rate decrease is found at the western end of the aftershock zone of the first mainshock (Figure 3.2a, circle A). After the second mainshock, the time series of aftershocks at this node (Figure 3.3A) exhibits a clear rate decrease ($\Delta_{RC} \simeq -8$). The aftershocks within the adjacent circle B on the other hand display a large positive Δ_{RC}. This region coincides with the northern end of the north striking-segment of the conjugated fault on which the second mainshock occurred (Figure 3.1). Hence this positive relative rate change

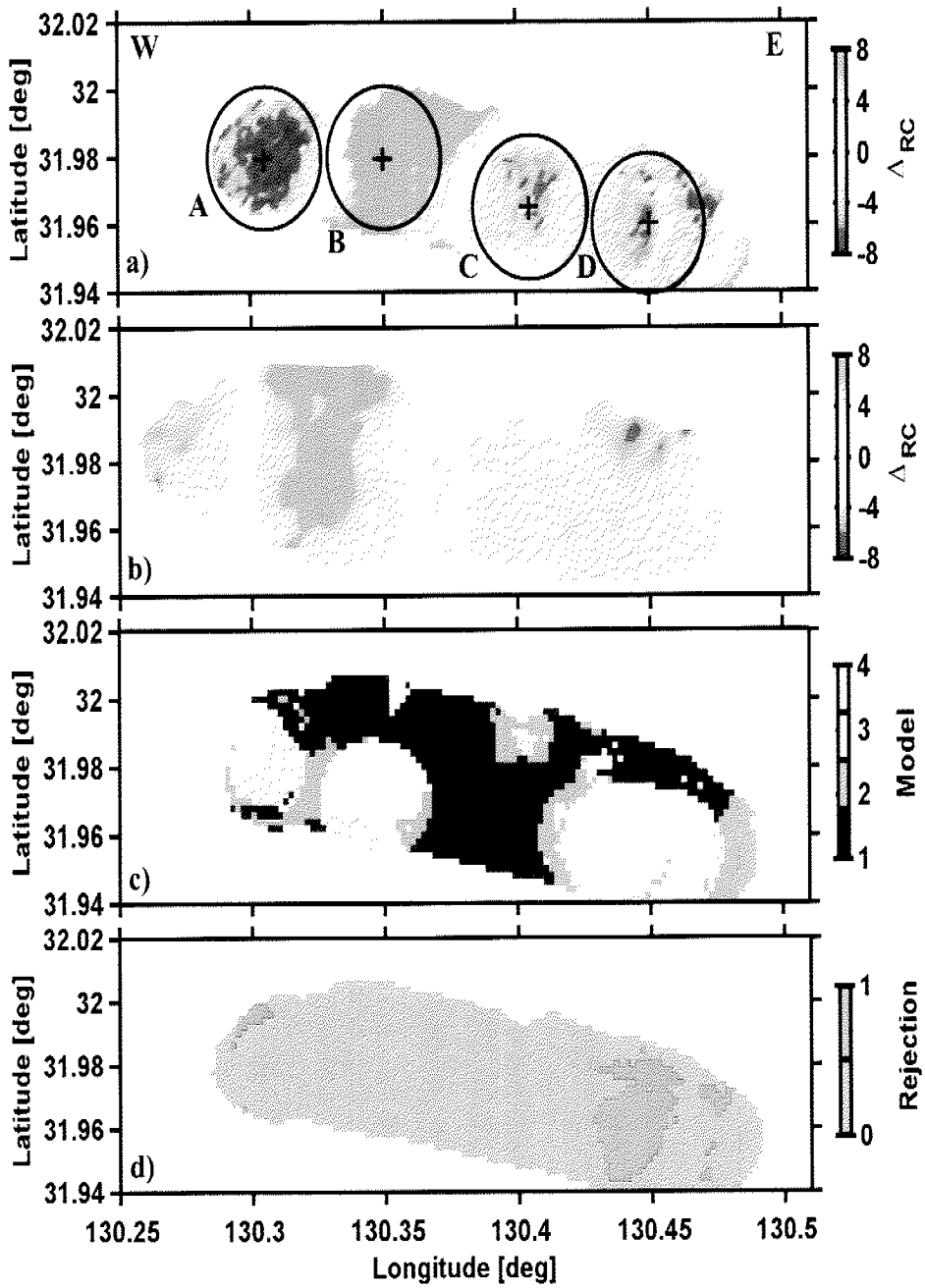

Figure 3.2: Spatial distribution of a) Δ_{RC} for the KU catalog, b) Δ_{RC} for the JMA catalog. Spatial parameter distributions computed for the KU catalog are, c) the best fitting model and d) the KS-test rejection (H). Sub-catalogs are created using events located within $R =$ 2km radii and $R = 3$km for the KU and JMA catalog, respectively. Crosses and circles relate to Figure 3.3.

($\Delta_{RC} \simeq 11.5$) is most likely triggered aftershock activity near the rupture termination of the second mainshock. Within the third area, to the east of the hypocenter of the first mainshock, we also detected a significant negative rate change (circle C). The onset of aftershock quiescence in this volume ($\Delta_{RC} \simeq -5.5$) occurred about five to seven days later than in circle A. Within the forth area (circle D), close to the east end of the aftershock zone, there is an apparent decrease in aftershock activity following the time of the second mainshock. However, the model fit in the learning period is poor (Figure 3D) as indicated by the KS-test rejection level $H = 1$, thus we do not consider this region to be meaningful. At the south eastern end, we find significant positive rate changes for off-fault aftershocks but insignificant ones closer to and north of the fault line.

The nested Omori models that match the aftershock data vary spatially (Figure 3.2c) because the large aftershocks have a heterogeneous spatial distribution (Figure 3.1). The regions A, B, and D of rapidly changing aftershock activity require the nested Omori models 3 or 4 due to the complexity of the aftershock occurrence: Region A is characterized by a series of $3.0 \leq M_L \leq 3.9$ events, the sequence in region B is influenced by a strong $M_L = 5.6$ event and region D is again characterized by a series of $4.0 \leq M_L \leq 4.8$ events. In contrast, region C does not include large aftershocks and is well fitted with a single modified Omori law. Thus, the respective spatial pattern of the model distribution concerning their complexity coincides well with the aftershock distribution.

3.6 Discussion and Conclusions

To quantify the effects of the second mainshock on the aftershock sequence of the first mainshock, we investigated the aftershock activity focusing on aftershocks adjacent to the northern fault that ruptured in the first mainshock. The 1997 Kagoshima earthquake doublet occurred in a small area, and thus it is reasonable to expect the

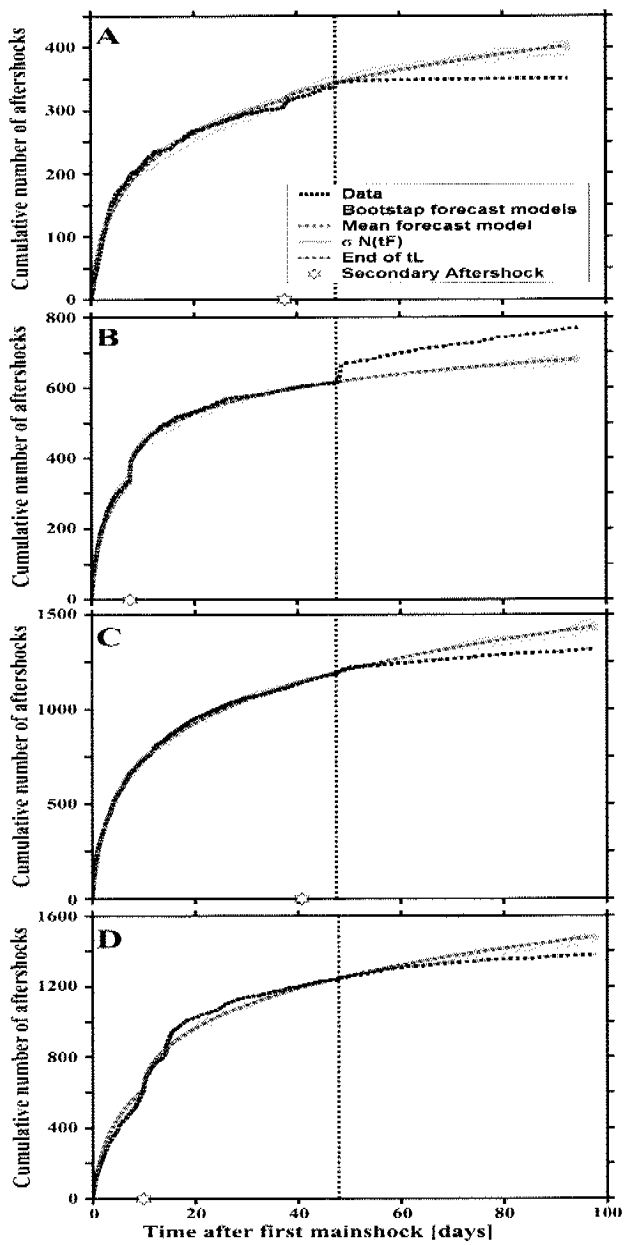

Figure 3.3: Modified Omori law fits for grid nodes indicated on Figure 3.2 a with the bootstrap forecast models plotted as gray lines in the background, the dashed blue line displaying the mean forecast model and the red bar indicating the standard deviation of forecasted events at time t_F. The vertical line indicates the end of the learning period t_L. All panels show significant rate changes with the ones in panel A-C not rejected by the KS-test ($H = 0$). In contrast, panel D shows a poor fit as even the best model is rejected by the KS-test ($H = 1$).

second mainshock to have influenced the ongoing aftershock sequence of the first. We applied an objective spatio-temporal mapping approach and formulated a measure of the statistical significance of rate changes within the decaying aftershock sequence. Thus our approach differs from *Stein* (2003) and *Toda and Stein* (2003) who focused mostly on the physical implications of off-fault earthquake triggering and used subjectively selected boxes to determine rate changes. Our high resolution mapping results confirm quantitatively only some of their qualitative results. In particular, our mapping shows that a statistically significant rate decrease followed the second Kagoshima mainshock in the westernmost part of the aftershocks zone of the first mainshock (Figure 3.2a and 3.3A, box A in (*Toda and Stein*, 2003)). We also identify two other on-fault regions of increased and decreased aftershock activity. However, at the eastern end of the aftershock zone, we find statistically insignificant rate variations if possible to detect due to sparse data, where *Toda and Stein* (2003) claimed a qualitative significant rate decrease (Figure 3.3a, box C in *Toda and Stein* (2003)). Our quantitative analysis shows that both off-fault and on-fault aftershock activity were increased but also decreased by the nearby second mainshock. These findings may independently contribute to determining the validity of the stress triggering hypothesis (*Harris*, 1998) as well as seismicity rate change computations based on rate and state friction (*Dieterich*, 1994) by using our approach as a quantitative measure.

How the effects of static stress changes on earthquake triggering may be affected by the presence of crustal fluids or anisotropic crustal material properties is poorly understood. There are many hot springs in the area and crustal fluids or geothermal areas as well as geological boundaries may have affected the temporal evolution and spatial distribution of aftershock (*Miyamachi et al.*, 1999). Furthermore, differences in material properties could have contributed to the rupture behavior of the two mainshocks and the spatio-temporal distribution of the aftershocks. The

east-west rupture of the second mainshock propagated eastward while the rupture of the first mainshock propagated to the west (*Horikawa*, 2001). *Miyamachi et al.* (1999) relocated the 1997 Kagoshima earthquakes using a 3-D velocity model and suggested that some of the aftershocks were occurring on geological boundaries striking north-south. Thus, several other geophysical and geological parameters as well as other mechanisms, e.g. coseismic release of trapped high-pressure fluids, may have had similar influence on the spatial and temporal development of this sequence than coseismic changes in static stress, but these cannot be differentiated with our approach.

3.7 Acknowledgements

We thank H. Miyamachi, K. Goto and S. Toda for providing us with the Kagoshima University catalog, A. Yoshida for the JMA catalog. We thank M. Mai, D. Schorlemmer, S. Miller, G. Zöller and one anonymous reviewer for comments that improved the manuscript significantly. This is contribution number 1332 of the Institute of Geophysics, ETH Zurich. E. Hauksson was supported by grant number 01HQGR038 and this is contribution number 9034 of the Division of Geological and Planetary Sciences, California Institute of Technology, Pasadena.

Chapter 4

Spatial correlation of aftershock locations and on-fault main shock properties

submitted to the Journal of Geophysical Research

J. Woessner, D. Schorlemmer, S. Wiemer, and P. M. Mai

Title: Spatial correlation of aftershock locations and on-fault main shock properties

4.1 Abstract

We quantify the correlation between spatial patterns of aftershock hypocenter locations and the distribution of coseismic slip and stress drop on a main-shock fault plane using a non-standard statistical test. The tests evaluate if aftershocks are located in 1.) low-slip regions (Hypothesis H_1) or 2.) regions of increased shear stress (Hypothesis H_2). In both tests, we seek to reject the null hypothesis H_0: Aftershocks are randomly distributed on the main-shock fault plane. We tested the hypotheses on four strike-slip events for which multiple earthquake catalogs and multiple finite-fault source models of varying accuracy exist. Because we want to retain earthquake clustering as the fundamental feature of aftershock seismicity, we

generate slip distributions using a random spatial field model and derive the stress-drop distributions. We account for uncertainties in the aftershock locations by simulating aftershock locations within their location error bounds. Our findings imply that aftershocks are preferentially located in regions of low-slip and of increased shear stress particularly when considering relocated earthquake catalogs. However, the results show that stress-drop patterns provide less information content on aftershock locations. This indicates that the shear-stress change of the main shock may not be the governing process for aftershock genesis. We speculate that the redistribution of stresses from aftershocks, normal stress changes, fluid migation or other mechanisms may have similar influence on the occurrence of aftershocks.

4.2 Introduction

Analyzing the spatial and temporal evolution of earthquake rupture has led to compelling evidence that fault displacement and associated stress changes are heterogeneous at all resolvable scales along the fault plane. These heterogeneities are represented in finite-fault source models which result from inverting for slip on the fault plane based on a variety of data including strong ground motion and teleseismic recordings as well as geodetic measurements (e. g., (*Beroza and Spudich*, 1988; *Hartzell and Heaton*, 1986; *Wald and Heaton*, 1994)). Besides the primary goal to understand and model the rupture process of a moderate to large earthquake, it is of equal interest to understand the consequences for the following seismicity. It is generally assumed that the rupture process of the main shock and the resulting stress changes govern the subsequent aftershock activity to a large extend. The effect of the static stress changes induced by the main-shock slip should therefore be measurable in the aftershock sequence, particularly on and near the fault plane where stress changes are largest. However, the link between main-shock slip, resulting on-fault stress drop and aftershock seismicity on the fault plane has yet to be tested using

rigorous statistical approaches and high-quality slip and aftershock hypocenter data.

Aftershock sequences have been studied extensively and have proven to provide independent information on fault plane heterogeneity (e. g., (*Wiemer and Katsumata*, 1999; *Utsu*, 1999; *Ogata*, 1999)). However, only a few past studies have qualitatively addressed the relationship between the spatial distribution of aftershock hypocenters in comparison to the slip and/or stress-drop distribution on the main-shock fault plane (*Dalguer et al.*, 2002; *Mendoza and Hartzell*, 1988). An early qualitative correlation between aftershock locations and main-shock slip was provided by *Mendoza and Hartzell* (1988). By visual inspection, they found aftershocks to occur mostly outside or near the edges of high-slip regions of the main shock. *Das and Henry* (2003) investigated the spatial relationship mainly for large subduction zone type events. They found no universal relation between high- and low-moment regions and high or low aftershock occurrence, but they state (1) that generally few and smaller events occur in high-slip regions, (2) that aftershocks occur on favorably oriented planes in regions of increased stress, and (3) that clusters appear at the edges of rapid transition regions between high- and low-slip within the main fault area.

Many studies in the past decade focused on static and dynamic stress changes caused by main shocks, and their effect on future seismicity (e. g., (*Harris*, 1998; *Kagan and Jackson*, 1998; *Toda et al.*, 1998; *Stein*, 1999; *Gomberg et al.*, 2001; *Steacy et al.*, 2005; *Toda et al.*, 2005)). These studies generally excluded the closest 5–10 km to the fault plane, because here the details of the slip model are important. This is unfortunate, because here static and dynamic stress changes are strongest, and the large majority of aftershocks are triggered in the immediate vicinity of the fault plane. Our study extends triggering related work to the immediate vicinity of the fault plane, which is feasible now because of the improved quality of hypocenter

datasets and improved testing procedures developed herein.

The focus of our study is to evaluate the spatial relationship between the hypocenter location of aftershocks in comparison to the finite-fault source slip (Test T_1) and the corresponding on-fault stress-drop distribution (Test T_2). We develop a test that concurrently allows us to simulate the intrinsic uncertainties of aftershocks locations and slip distributions. The test is a modification of statistical approaches recently proposed for evaluating seismicity forecasts (*Schorlemmer et al.*, 2005a). Both tests T_1 and T_2 have the same null hypothesis H_0: Aftershocks are randomly distributed on the main-shock fault plane. The test hypotheses are:

- Test hypothesis H_1: Aftershocks are located in low-slip regions. Rejecting H_0 in favor of H_1 implies a correlation of aftershock hypocenter locations with low-slip regions (Test T_1).

- Test hypothesis H_2: Aftershocks occur in regions of increased shear stress, i. e. regions of negative stress drop. Rejecting H_0 in favor of H_2 implies a correlation of aftershock hypocenter locations with increased shear-stress regions (Test T_2).

We apply the testing procedure to four crustal, primarily vertical strike-slip events in California, USA, and Japan presenting the 2004 $M_W = 6.0$ Parkfield event as an extensive case study. These regions are monitored by dense seismic networks to constrain the location of the aftershocks which is important because we include small events for statistical inferences. This is simultaneously the reason to exclude large subduction events primarily investigated by *Das and Henry* (2003). Furthermore, we discuss the 1984 Morgan Hill (CA), the 1992 Landers (CA) and the 2000 Tottori (Japan) events for each of which we are using two finite-fault source models and two parametric earthquake catalogs.

No	Event	Date	M_W	u_{max} [cm]	a_x [km]	a_z [km]	H	Resolution [km]	F_{LS}
1	Parkfield[1]	09/28/2004	5.96	77	10.20	3.20	0.52	1.5×1.5	0.89
	Parkfield[2]	09/28/2004	5.96	101	12.80	6.60	0.34	2.0×2.0	0.94
2	Tottori[3]	06/10/2000	6.8	402	6.00	10.60	0.64	2.2×2.0	0.79
	Tottori[4]	06/10/2000	6.74	321	24.00	12.8	0.16	2.0×2.0	0.75
3	Morgan Hill[5]	04/24/1984	6.1	230	12.6	3	0.22	1.0×0.5	0.94
	Morgan Hill[6]	04/24/1984	6.1	100	10.6	4.8	0.1	1.92×1.0	0.83
4	Landers[7]	06/28/1992	7.3	794	17.0	5.0	0.62	2.5×3.0	0.62
	Landers[8]	06/28/1992	7.22	670	14.60	4.60	0.66	5.0×5.0	0.60

Table 4.1: Parameters of the finite-fault source models used for the test. Displayed are the moment magnitude M_W computed from the slip model, the maximum slip u_{max}, the von Karman correlation lengths along strike a_x and down dip a_z , the Hurst number H, the subfault resolution of the source model, and the fraction of low-slip regions F_{LS}. References: [1]*Ji et al.* (2004), [2]*Dreger et al.* (2005), [3]*Sekiguchi and Iwata* (2001), [4]*Semmane et al.* (2005), [5]*Beroza and Spudich* (1988), [6]*Hartzell and Heaton* (1986), [7]*Wald and Heaton* (1994), [8]*Hernandez et al.* (1999).

The objectives we seek to achieve with our study can be summarized as follows:

- Quantitatively test if, and to what extend, the main-shock slip/stress-drop distribution governs aftershocks seismicity.

- Advance our understanding of the main-shock rupture process and aftershock genesis.

- Evaluate the influence of the resolution of slip models and precision of aftershocks locations on such a test.

- Improve the understanding of so far poorly understood heterogeneity in space and time of aftershocks seismicity (e. g., (*Wiemer and Katsumata*, 1999; *Utsu*, 1999; *Ogata*, 1999; *Wiemer and Wyss*, 2002; *Helmstetter et al.*, 2003)).

- Contribute to the development of improved time-dependent forecasting models as e. g., by *Gerstenberger et al.* (2005).

4.3 Data

Our study is based on the comparison of two distinct datasets for four prominent earthquakes: finite-fault source models and parametric earthquake catalogs.

No.	Event	Catalog 1 (Relocated)			Catalog 2				W [km]
		M_c	δx[km]	δz[km]	Network	M_c	δx[km]	δz[km]	
1	Parkfield[1]	1.6	0.42	0.84	NCSN	1.4	0.42	0.84	5
2	Tottori[2]	2.6	1	2	JMA	2.0	1	2	5
3	Morgan Hill[3]	1.4	0.23	0.59	NCSN	1.0	0.23	0.59	3
4	Landers[4]	2.4	0.12	0.2	SCSN	2.2	0.48	1.25	5

Table 4.2: Table of events listing available catalogs and the magnitude of completeness M_c. δx and δz are the median horizontal and vertical location errors determined from the datasets. Errors are assumed to be normally distributed with the median being the standard deviation. W is the width of the symmetric box around the surface line projection of the finite-fault source model. references: [1]J. Hardebeck (pers. comm.), [2]*Fukuyama et al.* (2003), [3]*Schaff et al.* (2002), [4]*Hauksson and Shearer* (2005).

Properties and origins of the data are listed in Table 4.1 and 4.2, respectively. The finite-fault source models are taken from the online database of *Mai* (2004) (`http://www.seismo.ethz.ch/srcmod`), which provides several independently derived slip distributions for each event in our study. To capture epistemic uncertainties, we selected two solutions for each event, focusing on inversions primarily based on strong motion waveform and geodetic data. A systematic comparison of the source models for specific events, however, is beyond the scope of this study. The parametric earthquake catalogs for the different events were downloaded from the responsible data centers, relocated data sets were provided by scientists that processed the catalogs. For the test, we selected aftershocks that are projected linearly and normal onto the assumed main-shock fault plane as defined by the finite-fault source model. The lateral extent of the cross-sections to select the aftershocks varies, but in general the width of these are on the order of 1.5–2.5 km to each side of the assumed surface rupture (Table 4.2). The extent of the fault plane is based primarily on the extent of the aftershock zone in the first days to weeks, although geodetic data is increasingly incorporated as constraints for recent models. The width of the cross-sections is varied to investigate the dependence on the lateral extent.

The testing we apply does not rely on earthquake catalogs complete in magnitude;

however, one might envision scenarios were the incomplete part of the catalog contaminates the results, because small events are located less accurately, which may not be reflected in the standard error estimation. Therefore, we perform the tests based on a catalog containing all events of magnitude $M \geq 0.1$, and with a dataset that is largely complete in space and time. To determine the complete catalog, we first estimate the magnitude of completeness M_c during the aftershock sequence as a function of time, using an overlapping moving window approach applying the EMR method (*Woessner and Wiemer*, 2005). In a next step, using data from the first few months only, we spatially map M_c on the fault plane as defined by the finite-fault source models. Based on this analysis, we define an overall M_c which ensures that the catalog is largely complete in space and time (with the exception of some sub-volumes in the first few hours of the sequence; see *Woessner and Wiemer* (2005) for details), and cut the catalog accordingly (Table 4.2).

We account for hypocentral location uncertainties in our method by simulating locations of the aftershocks within the given error bounds for each individual event. With the exception of the catalog by *Hauksson and Shearer* (2005), the relocated catalogs provide only relative location errors. In these three cases, we use the median errors taken from the networks' routine catalogs (catalog 2 in Table 4.2) for the simulations of possible aftershock locations.

Uncertainties in the finite-fault source models are accounted for by randomizing the slip distributions according to *Mai and Beroza* (2002). Finite-fault source models are solutions of an inverse problem that does not have a unique solution and is dependent on various assumptions, e. g., the velocity model, the causality of slip, the rupture velocity, the rise time and the source time function (*Mai and Beroza*, 2002; *Beresnev*, 2003). Although a lot of progress due to improved seismic and geodetic data sets, their combination in the inversion, refined inversion techniques,

and computer power has been made, the resolution of slip inversions is generally not better than about $3\,\mathrm{km} \times 3\,\mathrm{km}$.

4.4 Method

We introduce two closely related statistical tests to quantify the relationship between aftershock hypocenter locations projected onto the main-shock fault plane and (1) the finite-fault slip distribution (T_1) as well as (2) the inferred on-fault stress-drop distribution (T_2). The test hypothesis H_1 for test T_1 is: Aftershocks occur in low-slip regions on the main-shock fault plane. For test T_2 the test hypothesis H_2 is: Aftershocks occur in increased shear-stress regions. Both approaches are tested against the same null hypothesis H_0: Aftershocks occur randomly distributed on the main-shock fault plane.

4.4.1 Test preparation

In test T_1, we evaluate whether or not aftershocks preferentially occur in low-slip regions. We define low-slip regions as areas on the main-shock fault plane with a slip value less or equal than one third of the maximum slip during the main shock: $\Delta u \leq \frac{1}{3}\Delta u_{max}$. We assume this fraction of the maximum slip to be a reasonable choice based on investigations of 80 finite-fault source models from a database of about 50 earthquakes (*Mai et al.*, 2005). For these events, the percentage of fault area with large slip $\frac{1}{3}\Delta u_{max} \leq D \leq \frac{2}{3}\Delta u_{max}$ and very large slip $D \geq \frac{2}{3}\Delta u_{max}$ comprise about 28% and 7%. On average, about 65% of the area covered by finite-fault source models is therefore defined as low-slip regions in our study. This threshold is varied to investigate the influence of the assumption.

In test T_2, we investigate if aftershocks preferentially occur in regions of increased shear stress—which are simultaneously areas of negative stress drop ($\Delta\sigma < 0$). We do not use a threshold here because it is still an unresolved issue of how much

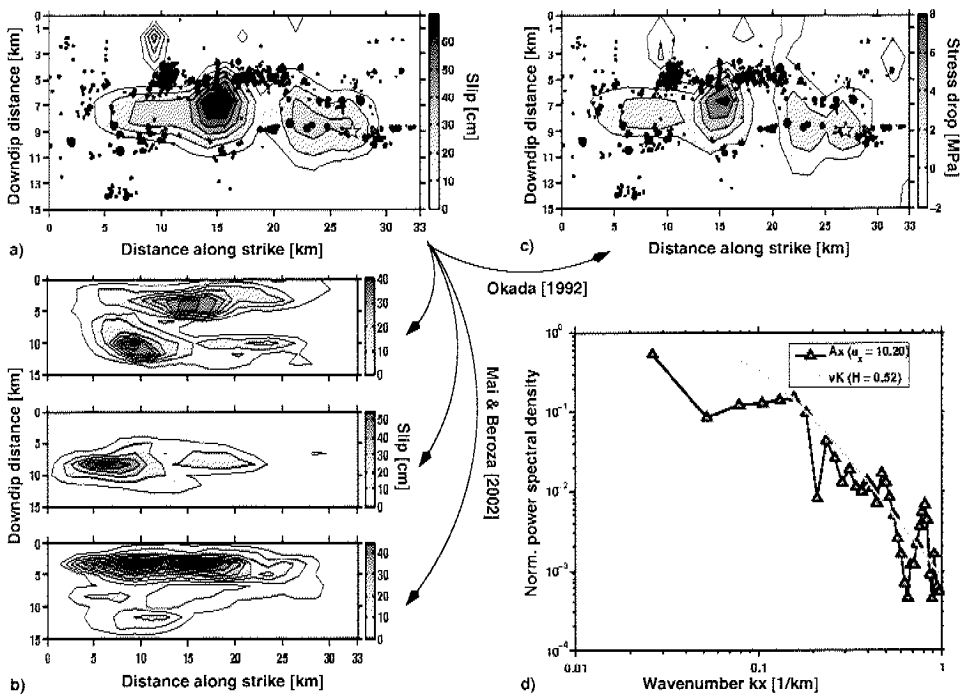

Figure 4.1: a) Finite-fault slip model of the 28 September 2004 Parkfield event by *Ji et al.* (2004) superimposed with relocated aftershocks (J. Hardebeck). b) Examples of slip distributions generated using the spatial random field model approach (*Mai and Beroza*, 2002). c) Finite-fault stress-drop model with aftershocks superimposed. d) von Karman correlation function fitted to the power spectral decay of the slip distribution in the wavenumber domain.

change in the state of stress is necessary to trigger events (*Harris*, 1998).

We perform tests based on comparing the observed distribution of aftershock hypocenters with respect to slip and stress-drop distributions. Randomizing either one of the distributions requires careful consideration of the property to be randomized. The most basic randomization would create randomly distribute hypocenters on a fault plane; however, clustering in space and time is one of the most fundamental characteristic features of aftershock seismicity. Unless we preserve this clustering, our test results may tell us more about general clustering of seismicity rather than the correlation of aftershocks and main shock properties. Pre-

serving clustering information can be done either by creating simulated, clustered sequences, or by retaining the aftershock hypocenters and simulating slip distributions. Both approaches are equally viable. Because we do not know well how to create randomized clustered hypocenters, we generate slip-model realizations using the spatial random field model that characterizes rupture complexity as imaged for past earthquakes (*Mai and Beroza*, 2002). Testing several (auto-)correlations functions (ACF), they found that the von Karman correlation function with moment-dependent correlation lengths provides the most consistent stochastic description for finite-fault slip models. The correlation lengths in along-strike (a_x) and down-dip (a_z) direction increase with increasing source size, while the Hurst number H remains scale invariant. These parameters, estimated from a finite-fault slip model (Figure 4.1a), define the decay of the power spectral density (PSD) of slip values in the wavenumber domain (Figure 4.1d).

In our simulations, we generate random slip distributions using the correlation lengths and Hurst number estimated from published slip maps. In general, the source dimensions and seismic moment for such slip simulations are chosen according to source-scaling relations (*Wells and Coppersmith*, 1994; *Somerville et al.*, 1999; *Mai and Beroza*, 2000); similarly, the correlation lengths are computed using empirical scaling relations (*Mai and Beroza*, 2002). In the present study, we choose the correlation lengths calculated for the slip distributions of the target events (Table 4.1). We fix the size of the rupture plane and the seismic moment to the corresponding values of the inverted source model. The slip realization, calculated at the same resolution as the original models, therefore obey the same power spectral decay, but have a different distribution of slip values (Figure 4.1b) since this spectral-synthesis approach assumes a normally distributed random phase. This slip-simulation approach ensures the generation of scenario earthquakes whose stochastic properties are consistent with past earthquakes of the same seismic moment and source dimen-

sions (*Mai and Beroza*, 2002). We finally calculate the on-fault stress-drop distribution based on analytical expressions that relate the final static displacements to the static stress changes in an elastic homogeneous half space (Figure 4.1c, (*Okada*, 1992; *Ripperger and Mai*, 2004)).

4.4.2 Testing procedure

In principle, both tests follow the same procedure with slight differences in the data preparation. Therefore, we only describe test T_1 in detail. The test hypothesis H_1 is tested against the null hypothesis H_0 using a one-sided N-test (Number test). The N-test compares the number of aftershocks located in low-slip regions for the original slip distribution (N_{LS}) to those from simulated slip distributions $N_{\mathrm{LS1}}...N_{\mathrm{LS1000}}$. Each aftershock hypocenter is assigned a main-shock slip value by projecting the aftershock along the fault plane normal onto the main-shock fault plane. The projection is performed first for the original slip distribution to obtain N_{LS} (Figure 4.2a, grey vertical line) and then repeated for thousand simulated slip distributions using the spatial random field model to determine $N_{\mathrm{LS1}}, \ldots, N_{\mathrm{LS1000}}$.

To estimate the influence of the aftershock hypocenter uncertainties, we simulate one thousand catalogs of aftershock locations by moving each earthquake horizontally and vertically by a value drawn from a random normal distribution with the standard deviation of the hypocenter uncertainty (Table 4.2). For each of these catalogs we then determine N_{LS}, based on the original slip distribution. The vertical dashed-dotted grey lines in Figure 4.2a show the standard deviation of N_{LS}. The solid black line in Figure 4.2a schematically shows the cumulative frequency distribution of the number of aftershocks in low-slip regions for one thousand simulations. The grey horizontal bar displays the rejection levels at the one-sided $\alpha = 0.1$ significance level. If the cumulative frequency distribution touches the grey rejection bar, we can reject the null hypothesis in favor of the test hypothesis H_1 (Fig-

ure 4.2a, dashed black line). Hypothetically, the cumulative frequency distribution could migrate to the right generating very small α-values. This would imply that the test hypothesis is worse than the null hypothesis we test against. Rejection in case of test T_1 at the $\alpha = 0.1$ significance level indicates that aftershocks preferentially occur in low-slip regions with a 10% probability of making a type I error, i. e., rejecting H_0 in favor of H_1 although H_0 is true. Likewise, in case of test T_2, rejection of H_0 in favor of H_2 implies a correlation between the stress-drop pattern and the aftershock locations.

The significance level chosen is a tradeoff between the uncertainties in the data sets and the rather unphysical null hypothesis. Due to the considerable uncertainties in the data sets, we apply less strong requirements. However, the larger the significance level, the larger the probability of making a type I error. A type I error means, H_0 is rejected in favor of the test hypothesis although it is true. Increasing the significance level facilitates to reject H_0 in favor of H_1 or H_2, but in turn increases the probability of making a type I error. A test at a smaller significance level would increase the strength of the result.

The test hypotheses are very rigorous and we emphasize that we do not expect that all aftershocks occur in the hypothesized regions. Other parameters such as normal stresses, fluid migration, geometrical complexities or the redistribution of stress from aftershocks themselves could similarly influence the genesis of aftershocks. Thus, a significance level of $\alpha = 0.1$ is in our opinion adequate for the purpose of this study.

In addition to the N-test result plot, Figure 4.2b displays the cumulative number of aftershocks located in regions less than a certain fraction of the maximum slip u_{max} as a black line. In the same manner, the cumulative fraction of cases of the slip distribution with slip less than a fraction of u_{max} is plotted. In test T_1, we use

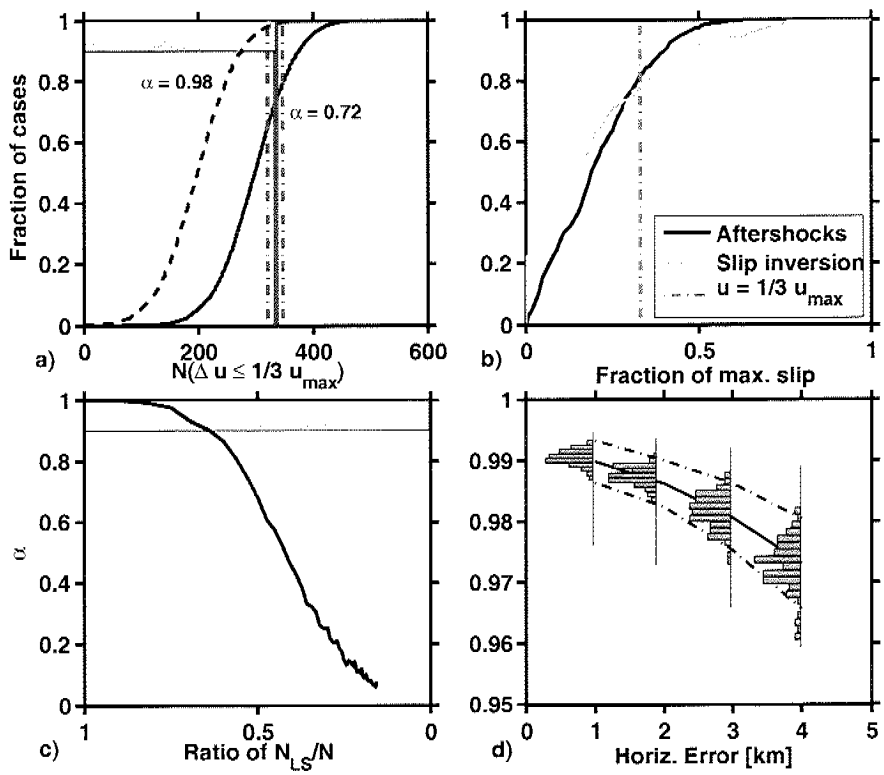

Figure 4.2: a) Schematic N-test result plot: Possible scenarios of either rejecting or not rejecting the null hypothesis. For explanation see text. b) Cumulative frequency distribution of the number of aftershocks (black) and fraction of the slip distribution (grey) as a function of the fraction of maximum slip. Dashed grey vertical line indicates the threshold for test T_1. c) Synthetic test: Dependence of the significance level α on the ratio of events in low-slip regions to the overall number of events. d) Synthetic test: α as a function of increasing normally distributed random errors. Histograms show the distribution of α-values.

the threshold $u \leq \frac{1}{3}u_{max}$ which means in this synthetic example that about 79% of the aftershocks are located in regions of low-slip. In addition, the grey line shows that a large portion of the slip distribution itself ($\approx 75\%$) shows values below the threshold. If this value is high, then the slip is concentrated on small asperities with relatively large slip. The same plot is possible for the inferred stress-drop distribution on the fault-plane, using a stress drop of $\Delta\sigma = 0$ as threshold.

In test T_2, the same procedure as for T_1 is applied to the stress-drop distribution derived from the slip inversion (Figure 4.1c, (*Okada*, 1992; *Ripperger and Mai*, 2004)). According to test T_1, the stress-drop value $\Delta\sigma$ is computed at the location of aftershock hypocenters by linear interpolation and the number of aftershocks located in negative stress-drop regions is determined (N_{SD}).

4.4.3 Synthetic tests

To illustrate our method, we construct a synthetic test that allows us to evaluate the dependence of the α-value on the ratio of the number of aftershocks located in low-slip regions N_{LS} to the overall number of events in the catalog N (Figure 4.2c). The synthetic test is performed for an arbitrary slip distribution S_1 created using the spatial random field model with parameters. We assume a magnitude $M_W = 6.5$ strike-slip event and, based on empirical relations, we compute the stochastic parameters (*Mai and Beroza*, 2000, 2002): the von Karman correlation length along strike $a_x = 8.03$ and down dip $a_z = 3.35$, Hurst number $H = 0.77$, fault length $L = 34\,\mathrm{km}$ and width $W = 15\,\mathrm{km}$. We created a synthetic catalog of 4000 events with a minimum magnitude of $M = 0.5$ and a b-value of $b = 1.0$. The hypocenter locations along strike reflect a uniform distribution, the depth distribution resembles a normal distribution fitted to the depth distribution of the relocated catalog for the Parkfield 2004 aftershock seismicity. Different ratios of N_{LS}/N were obtained by successively adding in events located in regions with slip values larger

than $u = \frac{1}{3}u_{max}$ for subsequent test runs. The α-value gradually decreases from $\alpha = 1$ in case of $N_{\mathrm{LS}}/N = 1$, i. e., only events in low-slip regions, to smaller values for decreasing ratios N_{LS}/N. For ratios of $N_{\mathrm{LS}}/N \lesssim 0.7$, we cannot reject H_0 in favor of H_1 at the $\alpha = 0.1$ significance level. This implies that at least about 70% of the aftershocks need to be located in low-slip regions to reveal a correlation in the synthetic test example (Figure 4.2c).

In a second synthetic test, we investigate the dependence of the significance value α on the location errors of the aftershocks (Figure 4.2d). We use the slip distribution S_1 from the first synthetic test and created a synthetic catalog of 2000 events located in low-slip regions. For this configuration, the test result is $\alpha = 1$ since this distribution resembles the expectation of the test hypothesis. The dependence on the location error is here tested by adding random errors to the hypocenters. The horizontal errors are assumed to be smaller than the vertical ones. The pairs of errors added follow a normal distribution with means and standard deviations of 0.5–2 km for the horizontal and 2–4 km for the vertical. For each error pair, one hundred catalogs were simulated. The results show that α decreases when adding larger errors. For the slip distribution used in this test, the dependence is not very strong and the test outcome, rejection of the null hypothesis in favor of the test hypothesis, remains unchanged. However, note that the reduction of the significance level depends on the ratio of low-to-high slip regions. The smaller the fraction of low-slip regions is, the more aftershocks are likely to be located in high-slip regions when adding random errors which reduces the significance level of the test.

4.5 Results

In this section, we discuss the results of the four selected events analyzed. For inter- and intra-event comparison reasons, we summarize the slip and stress-drop distributions in Figures 4.3 and 4.4. Plots showing the cumulative number of events

Event	Source model	Catalog 1 (Relocated)				Catalog 2			
		M_c	α	α_{min}	α_{max}	M_c	α	α_{min}	α_{max}
Parkfield	1	1.6	0.913	0.810	0.914	1.4	0.844	0.785	0.844
		0.1	0.920	0.818	0.897	0.1	0.772	0.716	0.772
	2	1.6	0.892	0.902	0.951	1.4	0.901	0.868	0.934
		0.1	0.913	0.920	0.955	0.1	0.904	0.879	0.912
Tottori	3	2.6	0.939	0.907	0.942	2.0	0.891	0.848	0.884
		0.1	0.929	0.916	0.935	0.1	0.867	0.839	0.862
	4	2.6	1	0.997	1	2.0	0.800	0.735	0.801
		0.1	1	0.994	1	0.1	0.799	0.749	0.789
Landers	5	2.4	0.866	0.848	0.871	2.2	0.692	0.626	0.692
		0.1	0.876	0.857	0.877	0.1	0.702	0.632	0.690
	6	2.4	0.493	0.459	0.592	2.2	0.297	0.267	0.315
		0.1	0.597	0.553	0.592	0.1	0.357	0.320	0.370

Table 4.3: Table of significance values α for test T_1. 10000 simulations are performed using data of 10 days after the main shock. α_{min} and α_{max} indicate the 95%-percentiles for the randomization of the aftershock locations. For the Morgan Hill event, all α-values are 1 or very close to 1. Finite-fault source models: [1]*Ji et al.* (2004), [2]*Dreger et al.* (2005), [3]*Sekiguchi and Iwata* (2001), [4]*Semmane et al.* (2005), [5]*Wald and Heaton* (1994),[6]*Hernandez et al.* (1999).

Event	Source model	Catalog 1 (Relocated)				Catalog 2			
		M_c	α	α_{min}	α_{max}	M_c	α	α_{min}	α_{max}
Parkfield	1	1.6	0.879	0.792	0.873	1.4	0.807	0.731	0.814
		0.1	0.895	0.808	0.869	0.1	0.771	0.728	0.792
	2	1.6	0.762	0.586	0.739	1.4	0.604	0.579	0.690
		0.1	0.813	0.677	0.770	0.1	0.702	0.706	0.769
Tottori	3	2.6	0.987	0.979	0.994	2.0	0.983	0.946	0.983
		0.1	0.988	0.987	0.994	0.1	0.980	0.964	0.979
	4	2.6	0.853	0.752	0.858	2.0	0.683	0.615	0.779
		0.1	0.846	0.764	0.828	0.1	0.665	0.625	0.729
Landers	5	2.4	0.847	0.818	0.878	2.2	0.548	0.413	0.544
		0.1	0.904	0.879	0.911	0.1	0.618	0.450	0.584
	6	2.4	0.245	0.216	0.298	2.2	0.282	0.205	0.291
		0.1	0.208	0.200	0.250	0.1	0.278	0.202	0.275

Table 4.4: Table of significance values α for test T_2. 10000 simulations are performed using data of 10 days after the main shock. α_{min} and α_{max} indicate the 95%-percentiles for the randomization of the aftershock locations. For the Morgan Hill event, all α-values are 1 or very close to 1. Finite-fault source models: [1]*Ji et al.* (2004), [2]*Dreger et al.* (2005), [3]*Sekiguchi and Iwata* (2001), [4]*Semmane et al.* (2005), [5]*Wald and Heaton* (1994),[6]*Hernandez et al.* (1999).

in low-slip regions as a function of the fraction of maximum slip are shown in Figure 4.5. Figure 4.6 displays superposed N-test result of increasing time periods for the Parkfield event in comparison to the finite-fault source model by *Ji et al.* (2004). Figure 4.7 summarizes the cumulative number of events in regions below a certain fraction of stress-drop as a function of stress-drop.

4.5.1 The 28 September 2004, Parkfield event

On 28 September 2004, an earthquake with a moment magnitude of $M_W = 5.96$ occurred on the Parkfield section of the San Andreas fault. Due to the variety of large projects like the Parkfield Prediction Experiment (*Bakun and Lindh*, 1984), the San Andreas Fault Observatory at Depth (SAFOD, *Hickman et al.* (2004)), and numerous seismic imaging projects (e. g., *Thurber et al.* (2003)), this section of the San Andreas fault is one of the best monitored fault systems on Earth. The event generated a wealth of high-quality geophysical and geological data. For the purpose of our test, this event represents an excellent case study since the quality of the data is probably superior to all other data sets used. We discuss this event in more detail than the other events.

We obtained two finite-fault source models (*Ji et al.*, 2004; *Dreger et al.*, 2005), each determined using strong motion and geodetic data (Figure 4.3a through 4.3d). In both models, the slip mainly occurs at a depth between 4–11 km and in two separated patches. The location of the highest slip patch between the models is significantly different (8 km) and the maximum slip differs by about 24 cm (Table 4.1). The hypocenters of the solutions are located at a depth of 9 km to the southern end of the resolved fault planes at the edges of larger slip patches.

The tests T_1 and T_2 were performed with both, the NCSN and a double-difference relocated earthquake catalog (see Table 4.2). The cross-sections (Figure 4.3a and 4.3b) display the finite-fault source models (*Ji et al.*, 2004; *Dreger et al.*,

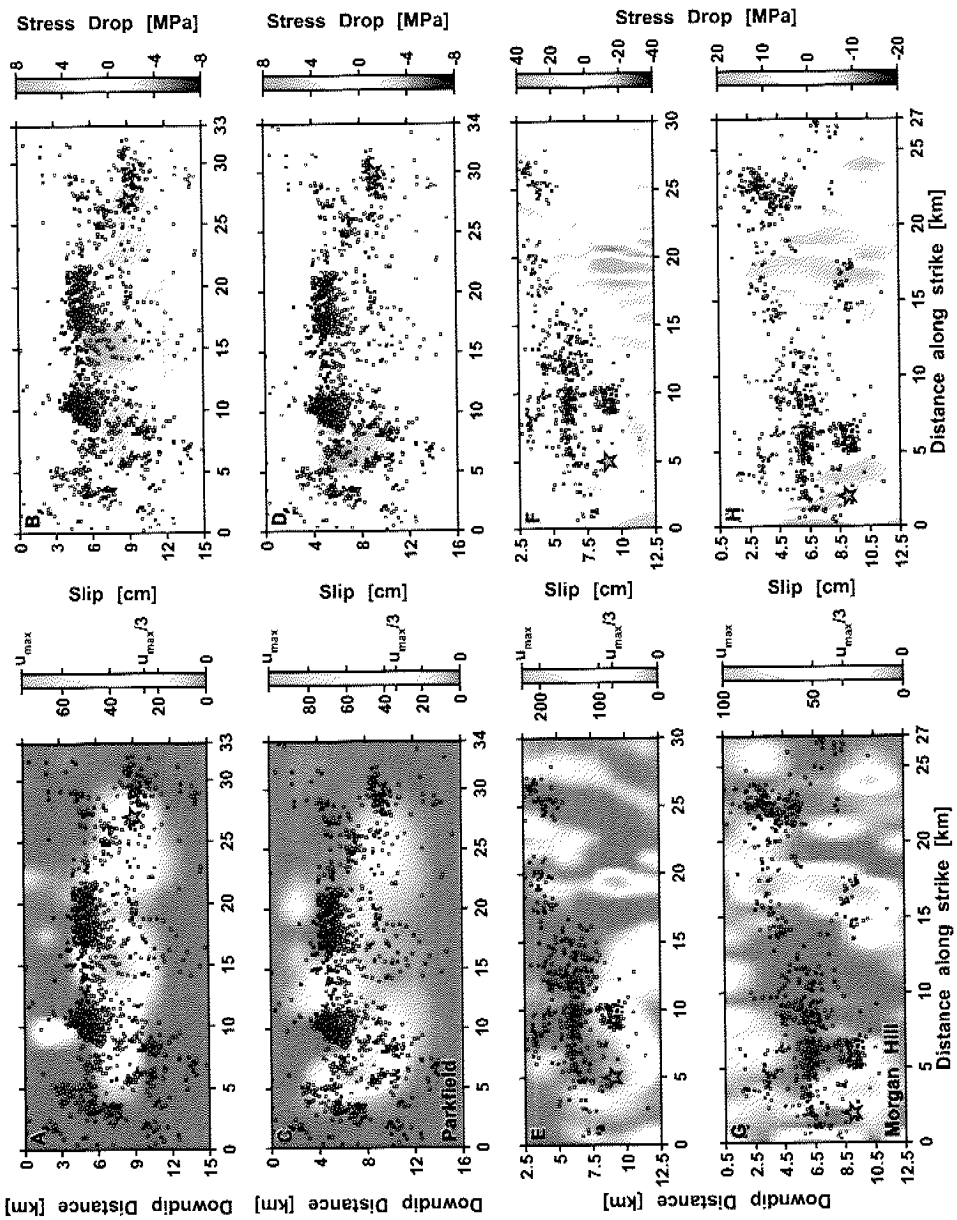

Figure 4.3: Finite-fault source models for the Parkfield (*Ji et al.* (2004)a-b and *Dreger et al.* (2005)c-d) and the Morgan Hill (*Beroza and Spudich* (1988)e-f and *Hartzell and Heaton* (1986)g-h) earthquake. Coseismic slip distributions are shown in the left, derived stress-drop distributions in the right column. Superimposed are the both available catalogs for a period of 10 days after the main shock. Dark grey and white rectangles symbolize hypocenters of the relocated and NCSN catalog,respectively, the star indicates the hypocenter. The white part in the colorbar visually distinguishes low and high slip as well as positive and negative stress-drop regions in the left and right column, respectively.

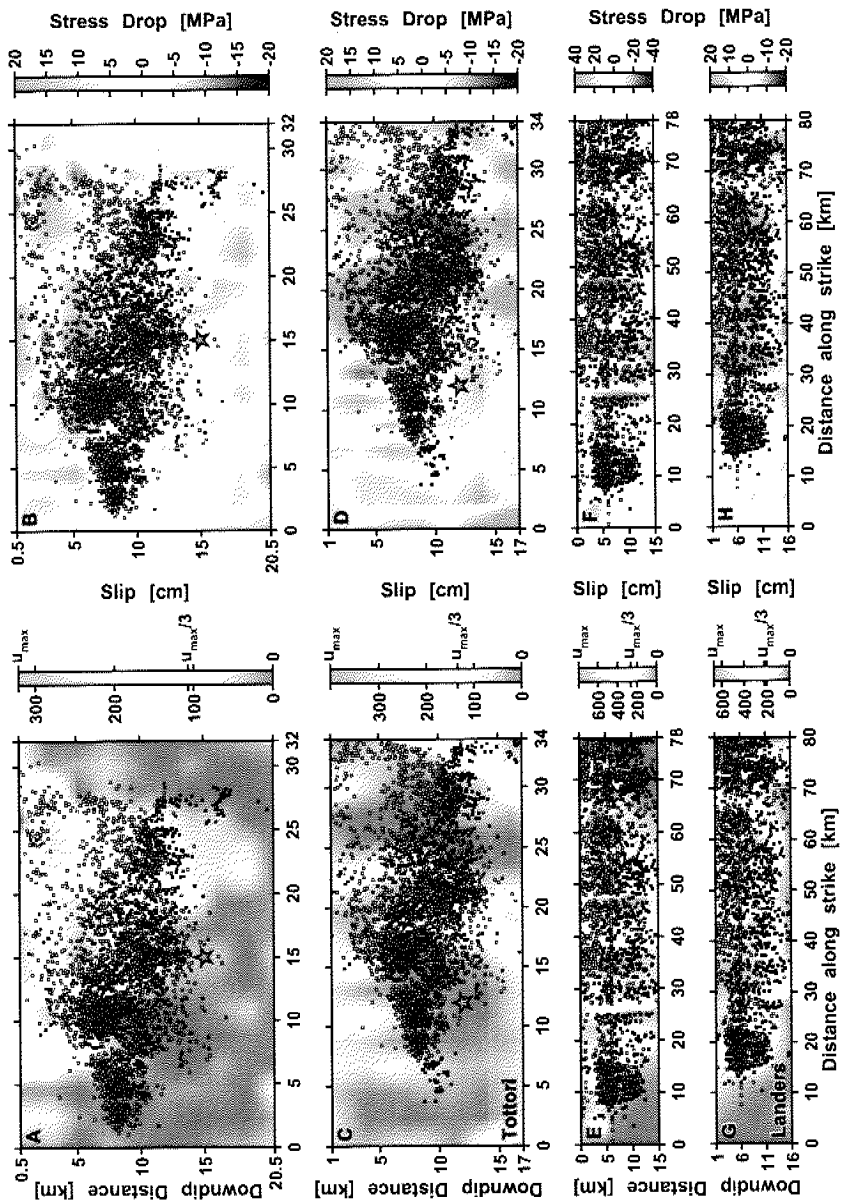

Figure 4.4: Finite-fault source models for the Tottori (*Semmane et al.* (2005)a-b and *Sekiguchi and Iwata* (2001)c-d) and the Landers (*Wald and Heaton* (1994)e-f and *Hernandez et al.* (1999)g-h) earthquake. Coseismic slip distributions are shown in the left, derived stress-drop distribution in the right column. Superimposed are both available catalogs per event for a period of 10 days after the main shock. Dark grey and white rectangles symbolize hypocenters of the relocated and general network catalogs, respectively, the star indicates the hypocenter. The white part in the colorbar visually distinguishes low and high slip as well as positive and negative stress-drop regions in the left and right column, respectively.

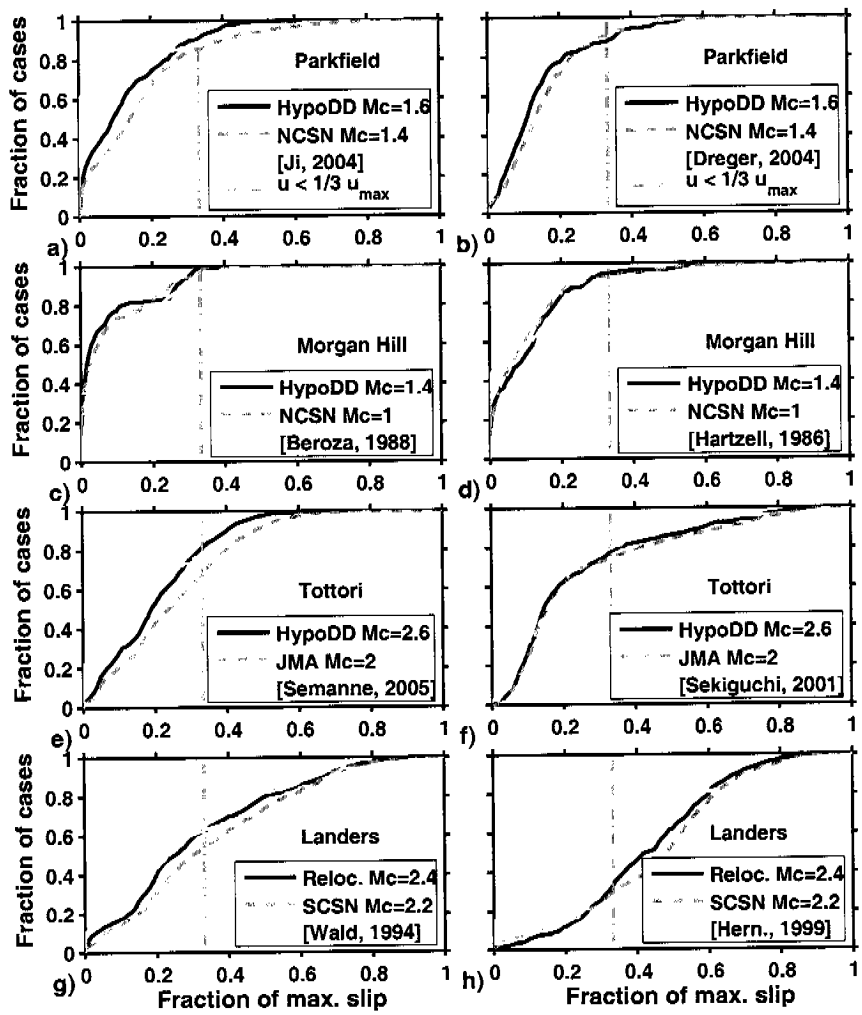

Figure 4.5: Cumulative number of events located in regions below a certain slip threshold as a function of the fraction of the maximum slip u_{max} for the different catalogs. The cumulative number is normalized by the entire number of events. The light grey line shows the cumulative number of subfaults below a certain slip threshold normalized by the entire number of subfaults.

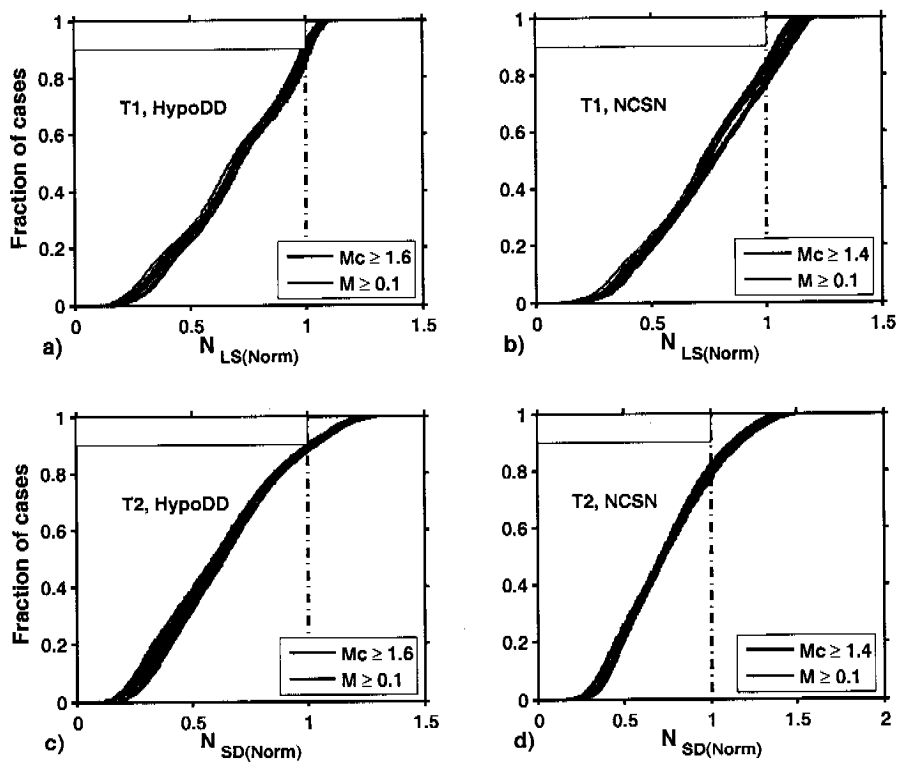

Figure 4.6: N-test result plot for the 2004 Parkfield event based on the finite source model of *Ji et al.* (2004). a) and b) display results of test T_1 for the HypoDD (left column) and the NCSN catalog (right column) using two magnitude thresholds. c) and d) show results of test T_2. The single lines represent computations of $12, 24, \ldots 240$hours using all events in the period.

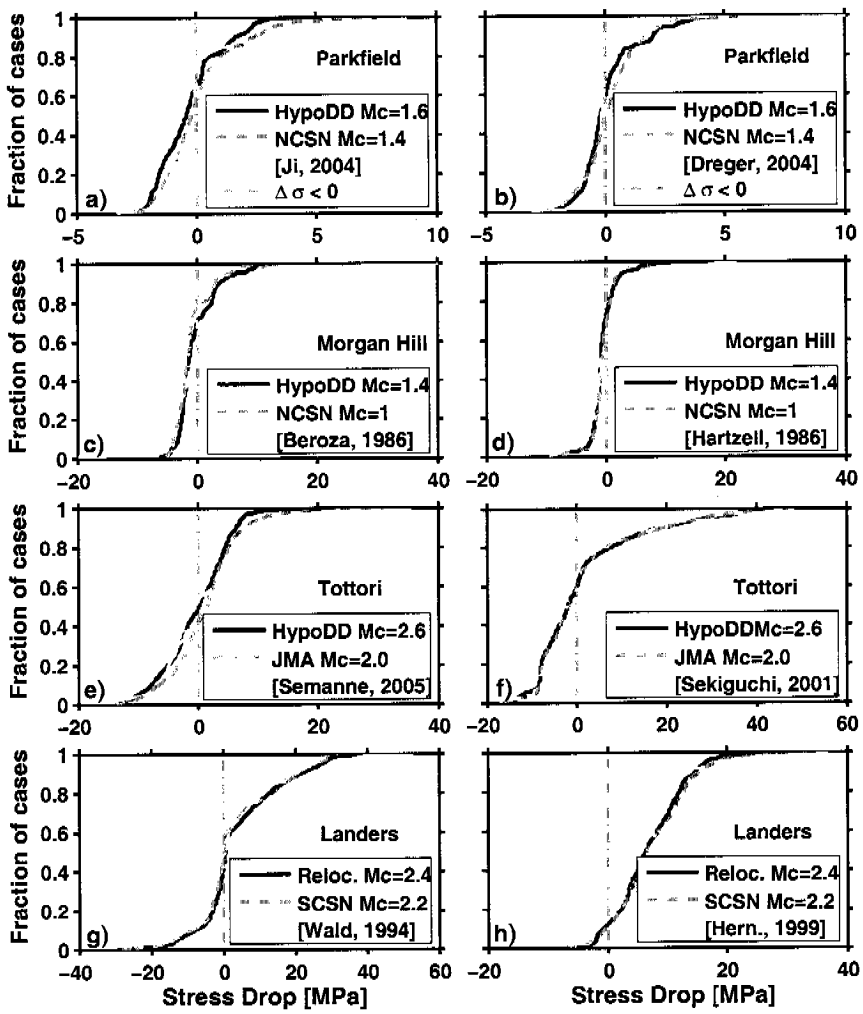

Figure 4.7: Cumulative number of events located in stress-drop regions below a certain threshold as a function of the fraction of stress drop $\Delta\sigma$ for the different catalogs. The cumulative number is normalized by the overall number of events. The light grey line shows the cumulative number of subfaults below a certain stress-drop threshold normalized by the entire number of subfaults.

2005) and the corresponding stress-drop distributions (Figure 4.3c and 4.3d) scaled with a regional rigidity model (*Ripperger and Mai*, 2004). Superimposed are the NCSN (white) and the double-difference relocated aftershocks (grey) of a 10 days period after the main shock. Aftershocks form an extended streak, a 10 km long horizontal alignment of hypocenters in a depth range between $3 - 6$ km similarly to the period before the $M_W = 5.96$ event (*Waldhauser et al.*, 2004). A smaller cluster is found around the hypocenter of the main shock to the southeast of the rupture plane at a depth of 9 km. The two largest aftershocks ($M_L = 5$) occurred to the northwest at a depth of about 10 km below the largest slip patches (*Schorlemmer and Wiemer*, 2005). A $M_L = 4.7$ aftershock occurred at shallow depth of about 6.6 km above the slip patches determined on the southeastern end. All features are observed in both catalogs but are more pronounced in the relocated one. The relocated hypocenters tend to be shifted to shallower depths compared to the NCSN catalog. We used a 5 km wide swath around the surface line projection of the finite-fault source models to sample the aftershocks. Based on analyzing the temporal dependence of the magnitude of completeness and spatially mapping on the main shock fault plane, we define $M_c = 1.6$ and $M_c = 1.4$ for the relocated and the NCSN catalog, respectively (Table 4.2).

The analysis of the 2004 Parkfield event reveals that large fractions of aftershocks occured in low-slip regions compared to the finite-fault source models. For the model determined by *Dreger et al.* (2005) and *Ji et al.* (2004), these fractions are 88% and 96% for the relocated catalog, 89% and 86% for the NCSN catalog, respectively (Figure 4.5a and 4.5b). Large portions of the slip distributions themselves have very little to no slip (both about 70%), and about 94% and 89% fall in regions of low-slip (Table 4.1). According to these observations and considering the uncertainties in the aftershock locations, test T_1 rejects the null hypothesis for both slip distributions using the relocated catalog in favor of H_1 at the $\alpha = 0.1$

significance level, whereas for the NCSN catalog, H_0 is rejected when correlating with the solution by *Dreger et al.* (2005) (Table 4.3). At the $\alpha = 0.2$ significance level, H_0 is rejected in favor of H_1 in all cases.

Figure 4.6a and 4.6b show N-test result plots obtained for the finite fault source model by *Ji et al.* (2004) for test T_1 and reflects the result from Table 4.3. The abscissae are normalized to N_{LS}, the cumulative number of aftershocks located in low-slip regions determined for the original slip distribution. This normalization allows overlapping multiple results of the N-test with the objective of studying the temporal evolution of the correlation. The first test was performed using data assembled in the first 12 hours, then the period was successively expanded by 12 hours up to 10 days after the main shock to examine temporal dependencies. In all four cases, no evidence for temporal evolution was found. We also investigated larger time spans, but the test results remain unchanged. In summary, these results imply at the $\alpha = 0.1$ significance level that relocated aftershocks of the 2004 Parkfield main shock are preferentially located in low-slip regions.

Testing the correlation between the aftershock hypocenter and the stress-drop distribution, test T_2, the null hypothesis is not rejected in favor of the test hypothesis H_2 at the $\alpha = 0.1$ significance level (Table 4.4). Figure 4.6c and 4.6d display the N-test results of test T_2 normalized to N_{SD}, the cumulative number of aftershocks located in increased shear-stress regions for the model of *Ji et al.* (2004). Both stress-drop distributions reveal approximately the same percentage of the fault plane with increased shear stress ($\approx 68\%$). The fraction of aftershocks located in increased shear-stress regions are in all cases below 65% (Figure 4.7a and 4.7b). The results of test T_2 suggest that there is no statistically significant correlation between the stress-drop pattern of the 2004 Parkfield event and the following aftershock distribution on the fault plane at the $\alpha = 0.1$ significance level. Furthermore,

the test results of T_2 do not reveal a time dependence.

Applying both tests with catalogs including all event with $M \geq 0.1$, we find slightly higher α-values when supporting both test hypotheses (Table 4.3 and 4.4). We conclude that small events tend to be located in regions of low-slip and increased shear-stress regions with a higher percentage for the relocated catalog which is an important finding. However, including events with magnitudes smaller than the completeness level of the catalog might bear the problem of drawing conclusions from non-representative samples.

4.5.2 The 24 April 1984 Morgan Hill event

The $M_W = 6.1$ Morgan Hill event ruptured parts of the Calaveras fault in Northern California. The finite-fault source models displayed in Figure 4.3e–4.3h were determined primarily using strong motion data and teleseismic waveforms (*Beroza and Spudich*, 1988; *Hartzell and Heaton*, 1986). Both slip inversion solutions are similar in the sense that large parts of the assumed rupture planes display very little slip and that strong slip heterogeneities are observed. The models differ largely in the maximum slip value (Table 4.1). The *Beroza and Spudich* (1988) model shows a more pronounced asperity when compared with the *Hartzell and Heaton* (1986) model.

Besides the NCSN catalog, a double-difference relocated catalog is available that exhibits highly organized structures of seismicity comparable to the Parkfield section (*Schaff et al.*, 2002). The latter catalog lead us to remove events associated with a blind thrust-fault inside the 3 km wide cross-section box around the fault plane (Figure 6 in *Schaff et al.* (2002)). The magnitude of completeness was computed as a function of time and mapped on the respective cross-sections of the assumed fault planes (*Woessner and Wiemer*, 2005). Based on these results, we defined the completeness level for the NCSN-catalog at $M_c = 1$ and for the relocated

catalog at $M_c = 1.4$.

Compared to the other events for which we conducted the test, Morgan Hill is exceptional as the null hypothesis is rejected in favor of the test hypothesis in all cases ($\alpha \simeq 1$), meaning that aftershocks are preferentially located in regions of low-slip (Test T_1) and regions of increased shear stress (Test T_2). The percentages of events located in low-slip regions reflect the test result: although slightly varying with time, more than 98% of the aftershocks are located in low-slip regions for both catalogs compared to the Beroza source model and more than 90% compared to the Hartzell source model (Figure 4.5c and 4.5d). The percentage of aftershocks located in increased shear-stress regions is lower but still at a higher level of above 70% in comparison to other investigated events (Figure 4.7c and 4.7d). The reasons for the unique correlation are probably the strong and localized asperities identified by the slip inversions and the highly organized seismicity on the Hayward and Calaveras fault system.

4.5.3 The 6 October 2000 Tottori event

The $M_W = 6.6$ Western Tottori event occurred in southwestern Japan, in a region previously showing low seismicity rates. A detailed model of the fault structure was developed by combining double-difference relocated aftershock hypocenters and moment tensor solutions revealing a complex fault system (*Fukuyama et al.*, 2003). The finite-fault source models shown in Figure 4.4a–4.4d are based on simplified structures to invert for the slip distribution of the earthquake (*Sekiguchi and Iwata*, 2001; *Semmane et al.*, 2005). Due to the detailed information on the fault structure, the earthquake catalogs where selected in $5\,\mathrm{km}$ wide boxes around the ruptured fault segments. The magnitude of completeness levels using spatial and temporal analysis techniques were estimated to be $M_c = 2.6$ for the relocated and at $M_c = 2.0$ for the JMA catalog (see Table 4.2).

Test T_1 leads in case of the relocated catalog to a rejection of the null hypothesis in favor of H_1 at the $\alpha = 0.1$ significance level for both slip distributions. H_0 cannot be rejected in favor of H_1 when using the JMA data set (Table 4.3). This difference can be explained by the percentage of aftershocks located in low-slip regions (Figure 4.5e and 4.5f). For the Semmane model these values are about $\approx 80\%$ for the relocated and $\approx 70\%$ for the JMA catalog. For the Sekiguchi model this difference is much smaller ($\approx 73\%$ and $\approx 72\%$) and this is reflected in the significance levels (Figures 4.5e and 4.5f, Table 4.3).

Test results of T_2 reject the null hypothesis in favor of H_2 for the Sekiguchi model but not for the Semanne model at the $\alpha = 0.1$ significance level (Table 4.4). The percentage of events in increased shear-stress regions are around 60% for the Sekiguchi model and less for the Semmane model (Figure 4.7e and 4.7f). This implies that aftershocks are preferentially located in increased shear-stress region based on the Sekiguchi model, but not based on the Semmane model. Note that the percentage of seismicity in increased shear-stress and low-slip regions increases slightly with time for this event, however, this is not affecting the interpretation.

4.5.4 The 28 June 1992 Landers event

The $M_W = 7.3$ Landers, California, event is the largest earthquake investigated. This event ruptured several mapped surface fault traces (Emerson/Camp Rock fault segments, Homestead valley fault, Johnson valley fault from north to south) which are represented in the selected combined finite-fault source models preferred by *Wald and Heaton* (1994) and *Hernandez et al.* (1999) (Figures 4.4e–4.4h). The patches of largest slip in both models occur at the cross-over of the Emerson/Camp Rock and the Homestead valley fault segments with a difference of about $1\,\mathrm{m}$ in the inferred maximum slip. The Wald model identifies more heterogeneities with smaller, distinct patches of high slip and less slip present at the surface. However,

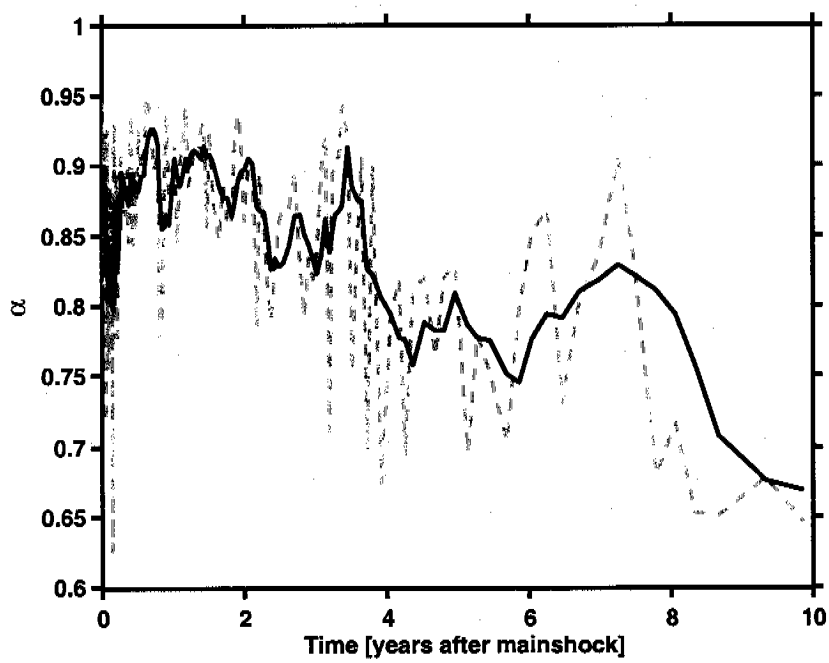

Figure 4.8: Temporal dependence of α-values for of test T_1. Results are computed for the 1992 Landers event using the Wald fault model and the relocated catalog with events of $M \geq 0.1$. The time series is created for non-overlapping moving windows of 200 aftershocks. The light dashed grey line shows results for the separate windows, the solid black line a moving average of 5 successive α-values. The significance level decays slightly with time and drops at about 4 and 8 years.

the models exhibit similar statistical properties represented by the von Karman correlation length parameters (see Table 4.1), though the solutions are based on different techniques and datasets.

The Southern California Earthquake Data Center (SCEDC) provides several data sets for the Landers event from which we chose the general SCSN catalog and a relocated catalog (Table 4.2, *Hauksson and Shearer* (2005)). We selected aftershocks in a 5 km wide box around the surface traces of the finite-fault source models using the information for the three segments. The magnitude of completeness varies significantly between the northern and the southern segments (*Woessner and Wiemer*, 2005), but since the threshold has a small influence on the results of the statistical tests, we chose general cut-off magnitudes of $M_c = 2.4$ for the relocated catalog and $M_c = 2.2$ for the SCSN catalog.

For the Landers case study, the tests for the relationship between the aftershock hypocenter locations of the SCSN catalog and both slip distributions do not allow to reject H_0 in favor of H_1 at the $\alpha = 0.1$ significance level (Table 4.3). The same result is found for the test using the relocated catalog. Comparing the results of the different slip distributions it is noteworthy that the rejection levels for the SCSN catalog and the Hernandez model (Figures 4.4e-4.4h) are much lower than for the other tests. The fraction of events located in low-slip regions is at a very low level (Figure 4.5h, 34% relocated, 29% SCSN) which corresponds to the relative smoothness of the Hernandez model as well as, at least in case of the SCSN catalog, problems with the depth determination. In case of the more heterogeneous Wald model, a much higher percentage of events falls into low-slip regions (Figure 4.5g, 71% relocated, 59% SCSN), for which the test is closer to rejection of H_0 for $\alpha = 0.1$.

Test T_1 reveals a temporal dependence in the long run (Figure 4.8). The α-values computed for successive windows of $N = 200$ events remain at a high level

for about 4 years, then they start to decrease with time and again drop at around 8 years. We speculate that this indicates a decreasing influence of the Landers event on the local seismicity. However, this time periods are short compared to overall estimated length of 20–56 years of the aftershock sequence (*Toda et al.*, 2005). Lower α-values in about the first 100 days of the aftershock sequence suggest that other processes like dynamic triggering, fluid migration or other nonlinear processes influence the occurrence of aftershocks.

Results of test T_2 likewise show an analogous picture, very little events being located in the increased shear-stress regions for the Hernandez model (12% relocated, 12% SCSN) and a much higher level for the Wald model (51% relocated, 41% SCSN) (Figures 4.7g and 4.7h). The null hypothesis is rejected in favor of H_2 only for the Wald model and the relocated catalog (Table 4.4). A clear difference is seen between the relocated and the SCSN catalog due to the percentage values when tested against the Wald model but not for the Hernandez model.

4.6 Discussion

Our study quantitatively correlates aftershock hypocenter locations and properties on the main-shock rupture plane, the slip distribution and the respective stress-drop distribution. The test is applied to four primarily vertical strike-slip faults for which well resolved finite-fault source models and well determined earthquake catalogs exist. Few events exist that fullfill these criteria and our study is only possible due to recent advancements in relocation techniques (*Waldhauser and Ellsworth*, 2000; *Hauksson*, 2000; *Hauksson and Shearer*, 2005). The selection of events reflects advances with time in the ability to resolve slip complexity as well as the ability to locate earthquakes with high accuracy. Both key tasks of seismology still suffer from relatively large uncertainties, but we believe that due to recent improvements

it is now appropriate to propose an approach to estimate the relationship quantitatively.

We find that in the case of test T_1, the null hypothesis can generally be rejected in favor of H_1 at the $\alpha = 0.1$ significance level when using the relocated catalogs. This implies that aftershocks do preferentially occur in low-slip regions, and that a statistically significant spatial correlation between the main-shock slip distribution and particularly the hypocenters of relocated aftershocks exist. Except for the Landers event, this results hold up for the routinely determined earthquake catalogs, but only at a significance level of $\alpha = 0.2$ which in our testing approach is a weaker statement. The higher significance level when using relocated catalogs is suggesting that relocation indeed enables us to reveal more of existing underlying physical processes.

Low-slip regions are somewhat arbitrarily defined in our test as locations at which less than one third of the maximum slip occurred $u \leq \frac{1}{3}u_{max}$. This is a reasonable assumption since about 70% of the slip distributions in the database have about 65% in areas with values less than one third of the maximum slip (*Mai et al.*, 2005). Tests with different threshold levels were conducted, but the results did not change except for thresholds at a very low level ($\frac{u}{u_{max}} \leq 5\%$). Very high threshold values ($\frac{u}{u_{max}} \geq 70\%$) are not suited for testing the hypothesis since this would define almost entire fault planes as low-slip regions, resulting always in a significant correlation. We also performed tests varying the width of the swath to select aftershocks which did not change the outcome of the results and their interpretation in general.

The largest significance level and therefore basically no correlation is determined for the Landers case using the finite-fault source model by *Hernandez et al.* (1999). The discrepancy to the Wald model is explained by the larger heterogene-

ity of the latter model, with more events located in low-slip regions. Note that many events exist in the SCSN catalog with a fixed depth of 6 km which, due to the smoothness of the slip inversion by *Hernandez et al.* (1999), result to be located in areas of relatively large slip.

In summary, we find about 50% of the T_1 tests using catalogs with events above M_c reject H_0 in favor of H_1 at the $\alpha = 0.1$ significance level and about 80% at the $\alpha = 0.2$ significance level. These values are slightly higher when using all events above $M \geq 0.1$. Considering only the test with the relocated catalogs, about 69% of tests reject H_0 in favor of H_1, for the general network catalogs this is only true in 38% of the cases at the $\alpha = 0.1$ significance level. Thus, we find a correlation between aftershock locations and low-slip areas on the main-shock fault plane supported particularly by high-quality data.

Test T_2 evaluates if aftershocks are preferentially located in increased shear-stress regions ($\Delta\sigma < 0$) rather than assuming a threshold value on the order of $\Delta\sigma < 0.01$ MPa thought to be sufficient to trigger aftershocks (*Harris*, 1998). The combined results imply that calculated shear-stress changes have only a weak correlation with aftershock activity. H_0 is rejected in favor of H_2 in case of the Tottori event (Sekiguchi model) and in all cases of the Morgan Hill event (38% of all cases). In all other cases, the null hypothesis cannot be rejected at the $\alpha = 0.1$ significance level. At the $\alpha = 0.2$ significance level, H_0 can be rejected in favor of H_2 in about 62% of the cases, but with a larger probability of rejecting the null hypothesis erroneously. Accordingly to test T_1, the α-values are slightly higher when using all events instead of using largely complete catalogs. Comparing the α-values for the relocated and the general network, we find a stronger correlation for the relocated catalogs. However, the correlation in comparison to test T_1 is statistically less significant.

The fact that low-slip regions provide more information content for aftershock activity than increased shear stress is an important finding. It implies that underlying assumption of static shear-stress changes as the primary physical mechanism triggering aftershocks is too simplistic. Other factors that need to be considered in this respect are that aftershocks themselves redistribute stresses rapidly (*Felzer et al.*, 2003; *Helmstetter et al.*, 2005), that normal stress changes and/or their combination (Coulomb failure stress) may equally strong affect the location of aftershocks close to the fault. Additionally, other mechanisms like fluid migration or degassing might play an important role for the generation of earthquake activity (*Bosl and Nur*, 2002; *Miller et al.*, 2004).

For both tests, we generally observe that the significance level increases when using all events instead of a catalog cut at the magnitude of completeness. This indicates that even a larger portion of the small events occurs in low-slip or increased shear-stress regions than for the larger ones (Table 4.3 and 4.4). This result may suggest that scaling properties of the post-main shock stress field may play a role with different sized events responding to different scale lengths of the rupture properties. However, it should be noted that not all of the small events are detected, which could bias the test results.

A specific case is the 1984 Morgan Hill event for which in both tests and for both catalogs the null hypothesis is rejected in favor of the test hypotheses. Several reasons for this fact might exist: Firstly, the seismicity on the Calaveras fault is highly organized and the aftershocks occur in regions where seismicity was clustered in space and time. Secondly, the slip distributions show very high peak slip values leaving most of the events in low-slip or increased shear-stress areas. Thirdly, the localized asperities identified by the finite-fault source models might support the hypothesis that existing holes in seismicity could appear as the areas in which larger

events on this segment can be generated (*Schaff et al.*, 2002). A similar setting is found on the Parkfield segment of the San Andreas fault system, where seismicity streaks, holes and repeating events have been reported (*Waldhauser and Ellsworth*, 2000). It is possible that for a tectonic settings of adjacent locked and creeping segments, the change in shear stress has a stimulating influence to trigger earthquakes on preexisting zones of weakness on the fault (*Zöller et al.*, 2005). However, the locations are not spatially offset due to the main shock occurrence.

Uncertainties in both data sets affect our abilities to resolve correlations. The best data sets in this respect are the relocated catalogs with an estimated relative error of a few hundred meters horizontally and vertically and an absolute error that is at most on the order of the ones determined in the routine locations. Uncertainties of other parametric earthquake catalogs range up to a few kilometers, generally twice as much in the vertical direction as in the horizontal one. We include this uncertainty by randomizing the earthquake locations in their respective error bounds; however the general interpretation of the test results remains the same. Based on the synthetic tests, special attention to this issue is required for the Landers case since the area of low slip only comprises about 60%.

Uncertainties are also contained in the finite-fault source models because these are results of inversion algorithms for which a variety of assumptions are necessary (*Beresnev*, 2003). The resolution of these models varies between 0.5 km and 5 km (Table 4.1), but the true uncertainty in the slip inversion is difficult to estimate. In our approach, epistemic uncertainties are addressed by using two different finite-fault source models and by randomizing the slip distributions with a spatial random field model (*Mai and Beroza*, 2002). Nonetheless, the uncertainties in the slip models could be incorporated more appropriately using multifold solutions of the actual inversion process instead of randomizing the authors best solution based on statis-

tical properties. The advantage, however, is the fast applicability of the statistical approach.

A temporal dependence of α-values is observed during the Landers sequence for which a first drop is observed about 4 years and a second about 8 years after the main shock. The decay reflects our expectation that the influence of the main-shock slip and stress changes on the seismicity decreases with time. However, this does not correspond to periods estimated for the duration of the aftershock sequence. The 1984 Morgan Hill and the 2004 Parkfield events do not show this dependence which may be explained by the specific tectonic setting of locked and creeping patches adjacent to each other. This type of regime is characterized by repeating earthquakes on the same locations, streaks and holes of seismicity which do not seem to be disturbed by main shocks of size $M6$ (*Waldhauser et al.*, 2004; *Schaff et al.*, 2002).

Noteworthy for the performance of the test is that the α-value might be influenced by the contribution of background seismicity to the aftershock sequence. The separation between the two types of events is difficult to achieve, but in general we expect the α-value to increase when the background seismicity was removed as they might not reflect the stress changes on the main shock fault plane. The effect of an decreasing significance level is supporting the test hypothesis.

4.7 Conclusion

In our study, we quantified the relationship between aftershock hypocenter locations and the main shock slip/stress-drop distribution. The developed non-standard statistical tests therefore enhance earlier qualitative investigations by *Mendoza and Hartzell* (1988); *Das and Henry* (2003). We found that aftershocks are preferentially located in low-slip regions with a higher significance for relocated catalogs compared to general network catalogs and also when including all events instead

of catalogs above the completeness level. Our test results suggest that aftershocks are correlated with stress-drop distributions, however, the correlation is statistically less significant compared to the correlation with the slip distribution. In summary, the correlation using relocated catalogs and all events ($M \geq 0.1$) is statistically more significant than with general network catalogs and/or complete catalogs. Our results are in agreement with the conclusions of *Mendoza and Hartzell* (1988) and *Das and Henry* (2003) for the slip test T_1, but in general not for the stress-drop test T_2.

We find that epistemic uncertainties included by using multiple data sets have stronger implications on the test results than aleatory uncertainties, i. e., randomizing hypocenter locations is found to have a small influence on α-values in the case studies as well as in synthetic tests.

The tests have so far been applied only to vertical strike-slip faults in crustal structures, but are adaptable to other types of earthquakes, different pre-, co- and postseismic properties of earthquakes and particularly close to seismogenic faults. We envision that from the information content we derive from testing several parameters using relocated catalogs, we are able to improve time-dependent forecasting models as suggested by *Gerstenberger et al.* (2005). The testing approach has been applied in a similar fashion to test earthquake forecasts (*Schorlemmer et al.*, 2004b), and is adaptable to other problems in seismology.

4.8 Acknowledgments

We would like to thank Northern California Earthquake Data Center (NCEDC) providing the catalog of the Northern California Seismic Network (NCSN), the Southern California Earthquake Data Center (SCEDC) providing the catalog of the Southern California Seismic Network (SCSN), and the Japanese Meteorological

Agency (JMA) providing us with the Japanese earthquake catalog. We are grateful for the relocated data sets provided by E. Fukuyama, J. Hardebeck, E. Hauksson, and D. Schaff. This is contribution number ???? of the Institute of Geophysics, ETH Zurich.

Chapter 5

Exploring the Heterogeneous Postseismic Stress Field Hypothesis

to be submitted in parts to JGR

Authors: J. Woessner, S. Toda, and S. Wiemer

Exploring the Heterogeneous Postseismic Stress Field Hypothesis

5.1 Introduction

Aftershock sequences are an ideal environment for studying geophysical mechanisms that influence the earthquake-size distribution, the relationship between the main shock and the aftershocks, the spatial distribution of aftershocks, and the duration of aftershock sequences. Variations in these parameters may be related to the main shock stress-drop, the state of stress in the fault zone, fluid migration, or other geophysical parameters. Often the earthquake size distribution is described with a power-law (*Ishimoto and Iida*, 1939; *Gutenberg and Richter*, 1944), in which the b-value represents the slope and hence the relative distribution between small and large events. The exponent p in the modified Omori law determines the rate decrease of aftershock sequences and mainly governs their duration (*Utsu*, 1961). The stress field orientation can be determined using earthquake focal mechanisms (e. g.,

Gephart and Forsyth, 1984; *Michael*, 1984, 1987a) and the local variability of the stress field, i. e. its heterogeneity, can be inferred from the misfit angle β to homogeneous stress tensor. Several recent studies have documented strong temporal and spatial heterogeneity of b-values, p-values, and the post-seismic stress field within aftershock sequences of recent large events such as Landers, Hector Mine, Denali and Western Tottori (*Wiemer and Wyss*, 1997; *Cao and Gao*, 2002; *Wiemer and Wyss*, 2002; *Ratchkovski et al.*, 2004). To improve our understanding of the link between main shock slip, resulting stress changes, and aftershock occurrence, we investigate the fine-scale properties of aftershock sequences. We compare these results to the parameters of the stress tensor inversions. Focusing on the immediate vicinity of the earthquake rupture allows us to evaluate the heterogeneous post-seismic stress-field hypothesis (HPSSF) as suggested by *Michael et al.* (1990) who analyzed the coseismic stress changes induced by the 1989 Loma Prieta earthquake.

The HPSSF-hypothesis states that a main shock with almost complete stress drop disturbs a previously homogeneous stress field by releasing most of the traction on the fault plane and leaving the stress field near the rupture area in a heterogeneous state with strong lateral variations. The complete stress drop may trigger aftershocks on faults in the crust that were unfavorably oriented in the previously homogeneous stress field. This can result in aftershocks with diverse focal mechanisms that have unfavorable orientations with respect to the pre-main shock stress field. *Michael et al.* (1990) analyzed the Loma Prieta aftershock data set using focal mechanisms determined with take-off angles from a 1D-velocity model. A similar stress field was obtained by *Eberhart-Phillips and Michael* (1998) using focal mechanisms computed with a 3D-velocity model. Locally heterogeneous stress fields supporting the HPSSF have been observed following strong earthquakes with magnitudes larger than $M = 7$, e. g., the 1992 Landers and the 1999 Hector Mine earthquakes (*Hauksson*, 1992; *Wiemer and Wyss*, 2002), and also for moderate sized

events like the 1983 Coalinga earthquake (*Michael*, 1987b). In addition, other studies have documented the evolution of the state of stress in the near field of fault zones prior to and immediately after an event (*Michael et al.*, 1990; *Hauksson*, 1992; *Wiemer and Wyss*, 2002; *Hauksson*, 2002).

The origin and implications of diverse aftershock mechanisms resulting from a main shock and the accompanying rotations of the principal stress axis have been debated in literature with respect to the mechanics of the San Andreas fault. The results by *Michael et al.* (1990) deduced from data subsets of the aftershock sequence could imply that the spatially uniform stress component of the stress field is fault normal compression, but the authors were not able to resolve this from the data. They concluded that this is because the magnitude of heterogeneous component of the stress field is much larger than the magnitude of the uniform component. *Kilb et al.* (1997) proposed that the combination of heterogeneous slip across the rupture plane an a relatively low-level background stress field leads to the aftershock mechanism diversity. In contrast, *Zoback and Beroza* (1993) analyzed the entire data set and concluded that the slip of the aftershocks is consistent with failure in response to a nearly uniaxial stress field. Similarly, the maximum principal stress axis acts almost fault normal to the main shock fault plane, but the homogeneous component of the stress tensor is larger than the heterogneous component. They thus argued that the heterogeneity is found in the fault strength. These interpretations have different implications for the mechanics of faulting on the San Andreas fault system. Both studies find that the 1989 Loma Prieta earthquake was a complete stress drop event, and hence the San Andreas fault has to be weak. However, only *Zoback and Beroza* (1993) conclude that the main shock induced decrease of fault strength helped controlling the occurrence of aftershocks under a fault normal compression.

By studying the orientation of the maximum compressive stress axis σ_1 com-

pared to the strike of the fault and its rotations after strong events other arguments for weak or strong faults have been obtained. *Hardebeck and Hauksson* (2001b); *Hardebeck and Michael* (2004) argue that the San Andreas fault is a weak fault in a relative sense to the other faults in the surrounding stress field as well as in an absolute sense considering the lack of heat flow anomaly. The rotation of stress axis in a zone of weakness on the order of a few kilometers, due to elevated fluid pressure on the basis of the fault fluid model, is consistent with a weak-fault interpretation (*Rice*, 1992; *Hardebeck and Hauksson*, 1999), but cannot explain wide zones of weakness. Another explanation could be a crust under low-stress as observed in the eastern California shear zone. Accordingly, *Zoback and Beroza* (1993) interpret the San Andreas to be a weak fault based on the high angle of $\sigma_1 \sim 50°$ to the fault strike resulting from near-hydrostatic pore-pressures and high crustal strength. In contrast, *Scholz* (2000) argues in favor of a strong fault by a model of a strong fault driven through a shear zone below, resulting in rotations of the stress field. However, this model contradicts the lack of heat flow anomaly (e. g., *Lachenbruch and Sass*, 1992).

We investigate the fine structure of aftershock sequences for several earthquakes (Table 5.1), resolving seismicity parameters onto vertical along-strike sections (cross sections) and in horizontal plane (map) view. The cross sections comprise the dimensions of finite-fault source models for the main shocks obtained from a finite-fault source model database (*Mai*, 2004). This combination allows a detailed comparison of main shock properties (the slip and stress drop distribution) with aftershock sequence properties (b- and p-value) and with the measure of stress field heterogeneity (angular misfit β, *Michael*, 1987a).

Statistically significant time-dependent and spatial variations of b-values have been documented in a wide range of studies: in laboratory experiments (*Scholz*,

1968; *Amitrano*, 2003), magma chambers (*Wiemer et al.*, 1998), along fault zones (*Amelung and King*, 1997; *Wiemer and Wyss*, 1997) and in aftershock sequences (*Wiemer and Katsumata*, 1999; *Schorlemmer et al.*, 2004a; *Woessner et al.*, 2004a). The interpretation of the b-value heterogeneity in terms of their relation to the stress field conditions or the stress regime is often blurred by small sample volumes, lack of data or other possible mechanisms that might contribute. However, recently *Schorlemmer et al.* (2005b) showed evidence that b-values depend on differential stresses and thus faulting styles which provides a physical basis for the interpretation of b-value variations.

We attempt to answer the unresolved questions of the HPSSF-hypothesis and the first order observations that regions of largest coseismic slip match regions of highest stress field heterogeneity. In addition, the detailed mapping allows us to test a hypothesis which extends the HPSSF-hypothesis and relates the stress tensor heterogeneity to the size of b-values in a highly fractured fault zone. *Wiemer et al.* (2002) proposed that a high degree of heterogeneity in stress also causes high b-values (H_1), since numerous small faults in multiple orientations can be activated resulting in relatively more small than large aftershocks.

The HPSSF-hypothesis postulates a sudden change in the stress field following a main shock. However, the temporal dependence of the stress field heterogeneity $\beta(t)$ following the main shock has not been thoroughly investigated. We hypothize H_2 that the stress field recovers with time, re-establishing the more homogeneous state of stress in the period prior to the main shock. Therefore, we analyze the temporal evolution of the observable, $\beta(t)$, for entire sequences of moderate events and "hot spots" of M7-type earthquakes. The hot spots are areas where the largest stress tensor heterogeneities are found following the main shock. This approach potentially may lead to new insights into the time needed to recover to the former state

No	Event	Date	M_W	u_{max} [cm]	Grid [km]	Size [km]
1	Morgan Hill	04/24/1984	6.1	100	1.92×1.0	12×27
2	Loma Prieta	10/18/1989	6.9	587	1.0×0.5	14×40
3	Landers	06/28/1992	7.3	794	2.5×3.0	15×78
4	Hector Mine	10/16/1999	7.1	820	2.66×3.0	15×54
5	Parkfield	09/28/2004	5.96	77	1.5×1.5	15×33

Table 5.1: Parameters of the finite-fault source models. Displayed are the moment magnitude M_W computed from the slip model, the maximum slip u_{max}, the subfault resolution, the size of the preferred model. Finite fault source models were developed by [1]*Hartzell and Heaton* (1986), [2]*Beroza* (1991), [3]*Wald and Heaton* (1994), [4]*Ji et al.* (2002b), and [5]*Ji et al.* (2004).

of stress and into the link between stress anomalies and the duration of aftershock sequences t_a.

Characteristic Omori law aftershock decay can be modeled as a sequence of earthquake nucleation events for which the distribution of initial conditions over the population of nucleation sources and the stressing history control the timing of the earthquakes. The initial conditions are experimentally derived rate- and state-dependent fault properties (*Dieterich*, 1994). In this model, aftershock parameters are interpreted in terms of stress changes and stressing rate, but only p-values of $p \leq 1$ can be reproduced and the heterogeneities on faults have not been fully investigated.

The modified Omori law and the Epidemic-Type Aftershock model (ETAS) are common models to describe the temporal decay of the rate of aftershocks (*Utsu*, 1961; *Ogata*, 1999; *Helmstetter and Sornette*, 2002). Both models are used to determine the duration of aftershock sequences for entire sequences or subvolumes along the cross sections. The major difference between the models is that ETAS-type models assume that each aftershock has its own aftershock sequence whereas this is not included in the modified Omori law. A wealth of studies has documented the spatial and temporal variability of the modified Omori law parameters (*Ouil-*

lon and Sornette, 2005; *Wiemer and Wyss*, 1997; *Wiemer and Katsumata*, 1999; *Woessner et al.*, 2004a). However, none of these studies provides an estimate of local differences in the aftershock duration which is of interest for applications in time-dependent seismic hazard assessment (*Gerstenberger et al.*, 2005). Based on the detailed mapping of modified Omori law parameters onto cross sections, we unravel spatial heterogeneities in the aftershock sequence duration assuming a constant background rate on the respective fault.

Our study contributes to ongoing research on basic relations between stress changes and earthquake triggering, fault zone mechanics and time-dependent seismic hazard assessment. The objectives of this study are

- to reevaluate the heterogeneous post-seismic stress-field hypothesis (*Michael et al.*, 1990),
- improve the understanding of the spatial relation between stress field heterogeneity and the main shock slip distribution (*Michael et al.*, 1990),
- to evaluate the causal relationship between high b-values and high stress field heterogeneity (H_1) (*Wiemer et al.*, 2002),
- to link temporal decay of stress field heterogeneity and aftershock sequence duration (H_2),
- and to explore possibilities of including fine-scale analysis of aftershock sequence parameters in time-dependent seismic hazard assessment (*Gerstenberger et al.*, 2005).

5.2 Data and Method

We use aftershock hypocenters of earthquake sequences in California (Figure 5.1) from several parametric earthquake catalogs to determine b- and p-values:

1. the standard southern California earthquake catalog,

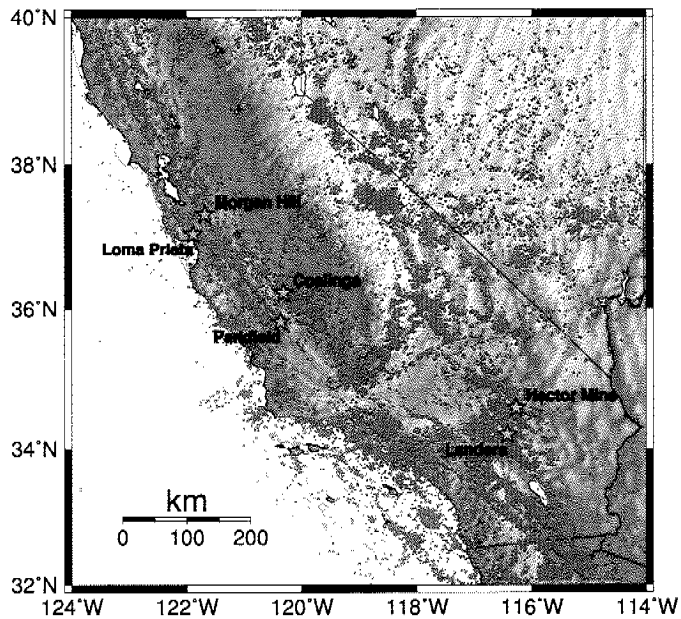

Figure 5.1: Seismicity map of California including detailed fault structures (red), seismicity of the ANSS catalog (1985-2004, $M \geq 2$, $d \leq 30km$). Red stars indicate locations of main shocks used in this study.

2. the catalog by *Hauksson* (2000), relocated using 3D ray tracing techniques combined with a 3D velocity model (updated until 2003),
3. the catalog by *Shearer et al.* (2005), relocated with events using waveform cross-correlation, site-specific events, and cluster analysis (Landers only for cross-checking),
4. the standard northern California earthquake catalog,
5. double-difference relocated catalogs from *Schaff et al.* (2002) (Morgan Hill, 1984) and J. Hardebeck (Parkfield 2004, pers. comm).

In most cases we use higher completeness levels for the time period immediately after the main shocks (Table 5.2) to take into account the lack of small events in the catalog caused by the high background noise level (*Wiemer and Wyss*, 2002; *Woessner and Wiemer*, 2005).

No	Event	Period [days]	M_c	Catalog
1	Morgan Hill		1.4	1984-1998[1]
2	Loma Prieta	0-3	1.4	1967-2005[2]
		> 3	1.2	
3	Landers	0-3	2.8	1984-2003[3]
		> 3	2.4	
4	Hector Mine	0-3	2.4	1984-2003[3]
		> 3	2.1	
5	Parkfield	0-6	1.4	2004.74-2005[2,4]
		> 6	1.2	

Table 5.2: Seismicity parameters for the aftershock sequences. Superscripts refer to the providers of the catalogs: [1]*Schaff et al.* (2002), [2]NCSN, [3]*Hauksson* (2000), [4]HypoDD J. Hardebeck (pers. comm).

For the stress tensor inversion, we use the focal mechanism catalog by *Hauksson* (2000) computed using a 3D velocity model for events in southern California and the focal mechanism catalog provided by the Northern California Earthquake Data Center (NCEDC) using a combination of several 1D velocity models for events in northern California (*Oppenheimer*, 1990). We checked the results of the stress tensor inversion and its measure of heterogeneity β using (1) all focal mechanisms and (2) events with high-quality focal mechanisms based on two quality parameters: the misfit to the first motion polarities is required to be less than 0.2 and the station distribution ratio needs to be larger than $STDR \geq 0.5$. The $STDR$ introduced by *Reasenberg and Oppenheimer* (1985) quantifies the spacing of the observations on the focal sphere relative to the nodal planes. The larger the $STDR$, the better the distribution with a value of 0.5 being an adequate quality indicator (*Hardebeck and Shearer*, 2002).

5.2.1 Stress tensor inversion

Earthquake focal mechanisms can be inverted to determine the orientation of the principal components of the stress tensor using several methods (e.,g. *Gephart and Forsyth*, 1984; *Michael*, 1984, 1987a; *Hardebeck and Shearer*, 2002). We apply

this approach to resolve the trend of the maximum principal stress axis σ_1 and the heterogeneity of the regional stress field as a function of space and time. We assess the orientations of the principal axes of the stress tensor and their uncertainties using the stress tensor inversion method of *Michael* (1987a) for two reasons: Firstly, *Hardebeck and Hauksson* (2001a) showed that uncertainties in the axis orientations based on synthetic tests are more accurate with this approach than Gepharts' method. Secondly, we use both high-quality and low-quality or noisy data sets. Stress tensor orientations of the noisy data sets are better resolved with Michaels' method whereas they are almost equally accurate for high-quality data sets using the Gephart method.

The inversion assumes that the regional stress field is a constant tensor, that the slip events are independent and that the magnitude of the tangential traction $|\vec{\tau}| = 1$ applied to each fault plane is similar. The inversion minimizes the misfit angle β_0, the angle between the observed slip direction $\vec{s}$ from each focal mechanism and the assumed shear stress or tangential traction (*Michael*, 1984, 1987a). The stress tensor inversion resolves the orientations of the principal stresses (σ_1, σ_2, and σ_3) ordered from most compressional to most dilatational and their relative amplitude ϕ:

$$\phi = \frac{\sigma_2 - \sigma_3}{\sigma_1 - \sigma_3}. \tag{5.1}$$

A general limitation of any stress tensor inversion is to correctly distinguish between the fault and the auxiliary plane. Although geological information can be used to select the correct plane *a priori*, a large percentage of the data cannot be attributed to specific faults (*Michael*, 1987a). This problem is accounted for by using a bootstrap technique to calculate the confidence limits for the stress tensor orientation. *Michael* (1987b) introduced a bootstrap resampling technique to estimate the

confidence limits focussing on the problem of unknown fault planes. The bootstrap technique switches a selected percentage of fault planes for the bootstrap samples. In principle, the more information is available for the inversion algorithm, the better the resolution obtained, i. e. , the confidence limits will be smaller if fault planes can be picked *a priori*. In our study, we assume for the bootstrap that both fault planes are equally likely. Based on this assumption, we compute 2000 bootstrap samples to obtain 95%-confidence limits.

The average misfit angle β is used as the measure for the heterogeneity of the stress field and is defined as the average of the β_0 values for the faults in the data set (*Michael*, 1987a). Errors $\sigma(\beta)$ are the standard deviations determined from the single fits to the data. According to *Michael* (1991), the distinction between a heterogeneous and a homogeneous stress field based on stress tensor inversion is a function of uncertainties in the fault plane solutions. We assume uncertainties of less than 20° for strike, dip, and rake for the data sets used according to *Michael* (1991); *Hauksson* (1992). Hence, we define the regional stress field to be heterogeneous for misfit angles $\beta \geq 45°$ since in these cases the assumption of a homogeneous stress tensor does not hold.

The ability to define meaningful confidence intervals is critical to distinguish spatial and temporal differences of the average misfit angle β. Performing stability tests, we scrutinize the dependence of β on the similarity of focal mechanisms in the data set and on the sample size of fault plane solutions for the inversion. The first test is crucial since the stress tensor is largely undefined when using identical or nearly identical focal mechanisms (*Michael*, 1987a). *Hardebeck and Hauksson* (2001b) suggested an approach to quantify adequate focal mechanism diversity for stress inversion based on synthetic tests using a root mean square difference compared to the mean focal mechanism. They proposed that a mechanism diversity of

$\sim$ 40°-45° for a data set with errors on the order of 10°-20° would be adequate to differentiate between and correctly recover two stress states which would be indistinguishable with less diverse focal mechanisms. However, the behavior of β in this respect is not documented. The second test allows to define a minimum number of events required for a stable β estimate. In the following, $\sigma(\beta)$ will refer to the uncertainty of the bootstrap estimates introduced above and $\sigma(\beta_{Michael})$ to the uncertainty computed in the inversion code.

Stability test 1: Similarity of focal mechanisms

To test the influence of similar fault plane solutions on the angular misfit, we define (1) a right-lateral strike slip event with dip direction $\phi_{dip} = 165°$, dip $\delta = 90°$ and rake $\lambda = 0$ and (2) a thrust event with dip direction $\phi_{dip} = 180°$, dip $\delta = 50°$ and rake $\lambda = 90$. One hundred samples of this synthetic focal mechanism are used as input to the stress tensor inversion algorithm, resulting in a $\beta = 0$ and $|\vec{\tau}| = 1$ as expected. In the following, we add uncertainties of increasing size ($2 \leq \delta \leq 40$, stepsize 2) to the hundred synthetic focal mechanisms. The uncertainties are assigned a uniform distribution, which is the worst case assumption. The experiment is repeated 100 times to compute standard deviations for the β-value. For the right-lateral strike slip event (Figure 5.2a), we add the uncertainty only to the rake.

Figure 5.2 shows that the misfit angle is increasing with increasing errors added to the focal mechanisms. The standard deviations from the hundred resamplings increase slightly but steadily with increasing errors. The standard deviation $\sigma(\beta_{Michael})$ calculated in the inversion code jumps at an error of about 20 degrees. This occurs when adding errors only to the rake (Figure 5.2a) and when adding errors to all three variables (Figure 5.2b). In the case of the chosen mechanisms, events do not switch the style of faulting, thus the jump in $\sigma(\beta_{Michael})$ is either an error in the code or a manifestation of a larger number of mechanisms that are very different from the general stress tensor. However, it is important for the application to note

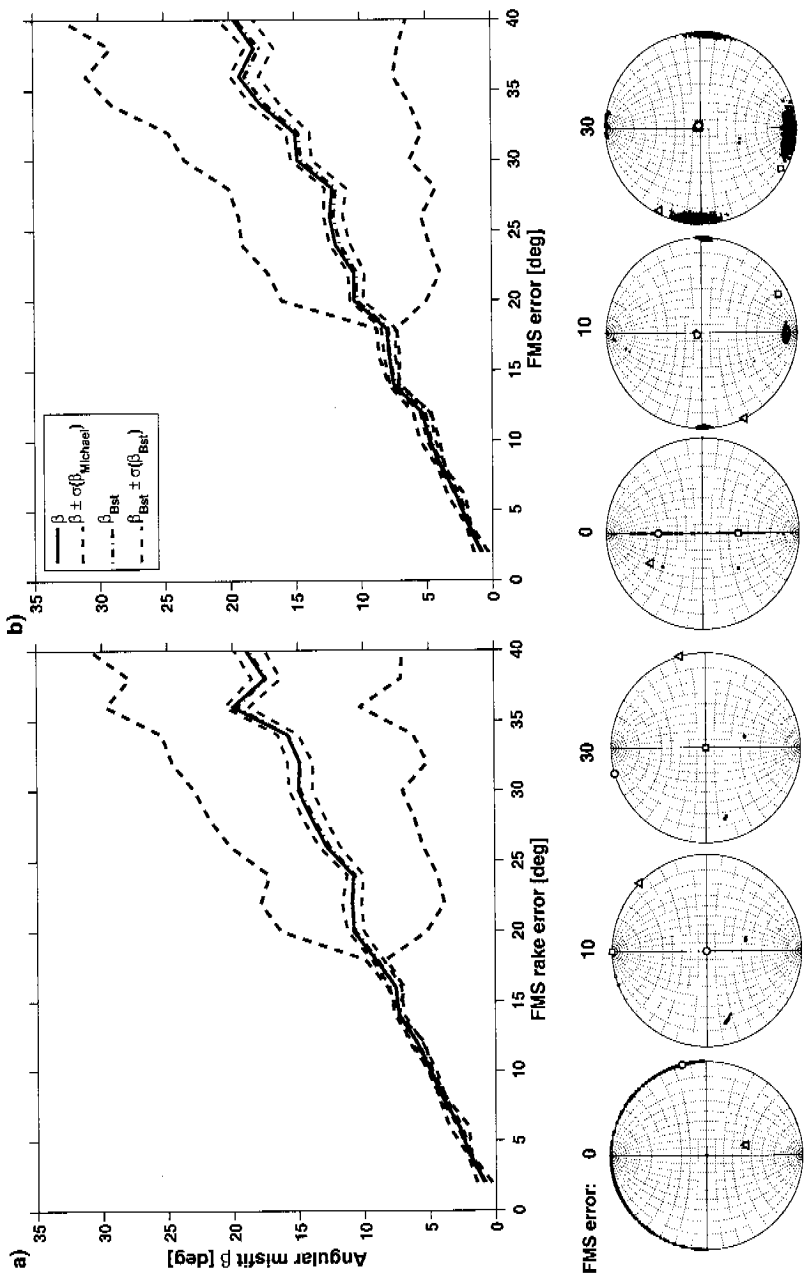

Figure 5.2: Stability of the average angular misfit angle β as a function of focal mechanism error: a) Right-lateral strike slip event with increasing error added to the rake angle. b) Dip slip event with focal mechanism error added to all three angles. Bottom line: Stereonet plot of the stress tensor inversion for different amounts of focal mechanism errors show that the stress field cannot be resolved adequately.

that the β value delivers stable estimates although the stress tensor itself cannot be resolved adequately because of identical or very similar focal mechanisms (Figure 5.2, bottom line of stereonet projections).

Stability test 2: Dependence on sample size

We investigate the stability of β as a function of sample size, i. e., the number of focal mechanisms, using the bootstrap resampling technique. The stability test focuses on the epistemic uncertainties of the solution by randomly producing subsets of the original catalog. This is different from the bootstrap technique applied in the stress tensor inversion itself, which incorporates aleatory uncertainties in focal mechanisms by flipping a selected percentage of the input fault planes to the auxiliary plane (*Michael*, 1987a). We generate 500 bootstrap samples of the original data set and then randomly draw an increasing number of focal mechanisms from the bootstrap samples starting at $n = 15$ and ascending up to the number of events in the catalog. For each of these subcatalogs, we compute the average misfit angle β and its standard deviation.

Assuming a dependence of β on the degree of diversity in the focal mechanisms, we select two regions of the 1989 Loma Prieta earthquake that reflect focal mechanism difference. The test is not based on synthetic data but on a selection of events described in section 5.3.1 and displayed in Figure 5.4a. These events represent both a homogeneous and a heterogeneous stress field region, each containing an adequate number of events. The dataset at shallow depths contains 83, in the deep section about 155 events. The stability test demonstrates that with an increasing number of events, β-values approximate the results for the entire data set, $\beta = 69°$ and $\beta = 19°$ (Figure 5.3a and 5.3b). Standard deviations $\sigma(\beta)$ decrease as expected with an increasing number of events (Figure 5.3c), with larger standard deviations obtained for the heterogeneous data set ($3.6° \leq \sigma(\beta) \leq 11.5°$) than for the homogeneous one ($1.5° \leq \sigma(\beta) \leq 4.6°$).

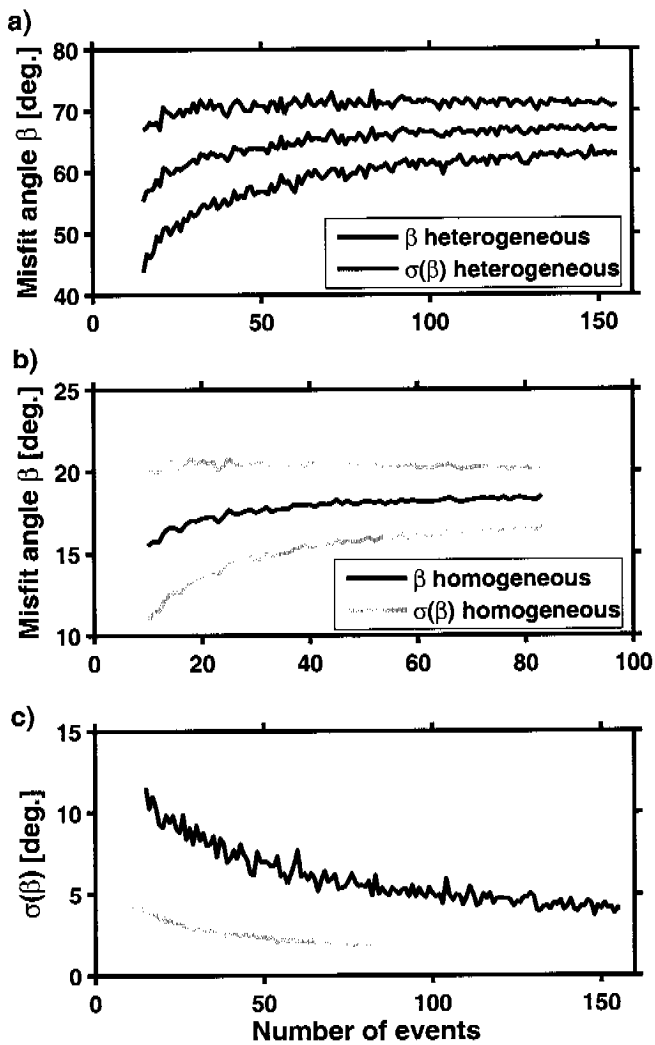

Figure 5.3: Stability of the average angular misfit angle β as a function of sample size using data from the Loma Prieta earthquake for a) a region with highly diverse focal mechanism, b) a region with more homogeneous focal mechanisms. c) Dependence of the standard deviations for the two data sets in comparison. Location is displayed in Box 2 and Box 1, Figure 5.4, respectively.

Based on the convergence for the different types of data sets, we recommend a minimum number of $n \geq 30$ focal mechanisms to estimate the stress tensor in regions with less diverse focal mechanisms and about $n \geq 50$ events in regions with highly diverse focal mechanisms. These minimum sample sizes are in good agreement with general suggestions for applying bootstrap techniques that require at least about $n \geq 50$ samples (*Chernick*, 1999).

5.2.2 Properties of aftershock sequences

We apply the Gutenberg-Richter relation and the modified Omori law to parameterize the properties of aftershock sequences. The frequency-magnitude distribution describes the relationship between the frequency of occurrence and the magnitude of earthquakes (*Ishimoto and Iida*, 1939; *Gutenberg and Richter*, 1944):

$$\log_{10} N(M) = a - bM, \quad M \geq M_c. \tag{5.2}$$

N is the cumulative number of earthquakes with magnitudes larger than M. The b-value is a measure of the relative size distribution of small to large events, the a-value describes the productivity of the volume. To ensure sufficient data for the maximum likelihood estimation procedure (*Bender*, 1983), we require at least $N = 100$ events above the magnitude of completeness to compute stable b-value estimates (*Woessner and Wiemer*, 2005).

The modified Omori law (*Utsu*, 1961) describes the temporal decay of the rate of aftershocks:

$$n(t) = k(t + c)^{-p}, \quad M \geq M_c. \tag{5.3}$$

with $n(t)$ being the number of earthquakes occurring at time t. k represents the

productivity of the main shock and depends on the lower magnitude threshold of the earthquake catalog. p is the measure of the exponential decrease of the aftershock rate, and c describes a temporal offset that compensates for incomplete data at the beginning of the aftershock sequence. These parameters are computed by a constrained nonlinear grid search over the parameter space ($0.2 \leq p \leq 2.7$, $0.01 \leq c \leq 5$, $10 \leq k \leq 5000$), maximizing the likelihood function for the modified Omori law following *Ogata* (1999).

For both empirical relationships it is critical to estimate the magnitude of completeness M_c. In general, the completeness level jumps abruptly after a large event and decreases gradually with time (*Woessner and Wiemer*, 2005). Of special interest are the first few days in the sequence during which seismic activity is very high, but for several reasons the completeness levels generally are also very high in this period. We approach this problem by using step functions for M_c with the levels determined by the EMR-method (*Woessner and Wiemer*, 2005). We map b- and p-values according to the approach of *Wiemer and Katsumata* (1999) by covering the study regions with rectangular grids ($0.5\,\mathrm{km} \times 0.5\,\mathrm{km}$, $1\,\mathrm{km} \times 1\,\mathrm{km}$) and selecting events in overlapping cylindrical volumes. We vary the radii of the cylinders as sensitivity checks and to evaluate the best possible coverage.

In principle, it is straightforward to estimate the duration of aftershock sequences t_a based on the modified Omori law parameters and the background rate of previous seismicity. By setting the background rate R_b equal to the modeled rate of aftershocks and solving for t, we obtain

$$t_a = \left(\frac{k}{R_b}\right)^{1/p} - c, \tag{5.4}$$

assuming the same magnitude of completeness or magnitude threshold before and

after the main shock.

Uncertainties in the modified Omori parameters can be adequately computed using a bootstrap approach. Based on a Kolmogorov-Smirnov test, inappropriate fits of the model to the data can be identified (*Woessner et al.*, 2004a). A correct estimate of the background rate bears potentially larger uncertainties due to the following reasons: First, in many cases the data set is rather insufficient to estimate the background rate at the threshold level obtained in an aftershock sequence since the completeness level is higher especially in the first days. Second, the selected regions to estimate t_a are generally chosen subjectively. Third, the background rate assumes independent events, i. e., a poissonian distribution of earthquakes. This requires declustering the earthquake catalog before the period of the main shock, resulting in even smaller data sets. Being aware of these deficiencies and uncertainties, but as a first approach we are using a windowing technique based on estimates for northern California (*Gardner and Knopoff*, 1974; *Uhrhammer*, 1986) to decluster the earthquake catalog. From the declustered catalogh we estimate the background rate.

5.3 Results I: Spatial comparison of seismicity parameters and main shock properties

First we discuss the results for the b-value, the p-value, the stress tensor heterogeneity β and the main shock slip and stress-drop distribution and compare their patterns in fixed periods. Second we discuss the durations of aftershock sequences t_a, their relations to the modified Omori law parameters, and the temporal dependence of the stress tensor heterogeneity.

5.3.1 Revisiting the 1989 Loma Prieta earthquake

The 1989 Loma Prieta $M_W = 6.9$ earthquake occurred within the San Andreas fault zone, near the Sargent and the Zayante-Vergeles fault. The main shock rup-

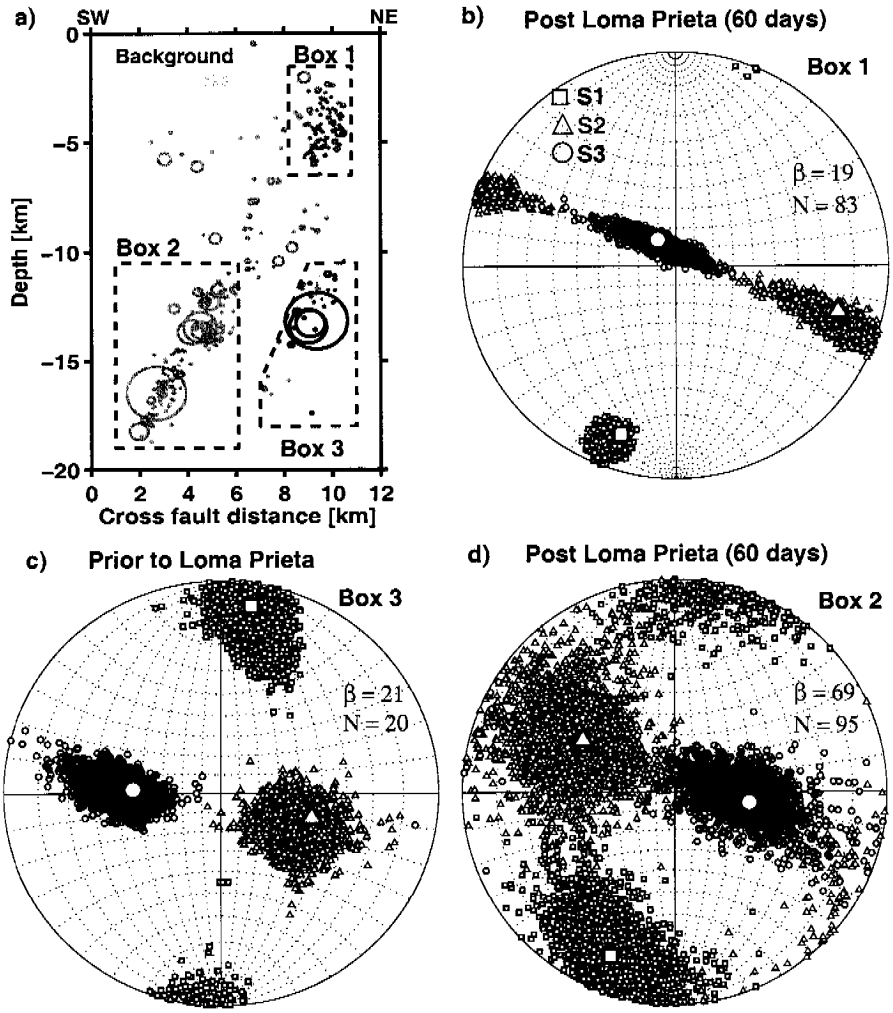

Figure 5.4: Replicating stress tensor heterogeneity at Loma Prieta. a) Cross section normal to the San Andreas fault (121.95°W /37.053°N – 121.872°W /37.125°N, width 10 km) and selected box volumes. b) Stress tensor for shallow events in the 60 days following the main shock. c) Stress tensor for deep events prior to the main shock (1967-1989.79). d) Stress tensor for deep events in the 60 days following the main shock. N is the number focal mechanisms available for the inversion.

Period	Location	β [deg]	$\overline{\beta}_{Bst}$ [deg]	$\sigma(\beta_{Bst})$ [deg]	$\sigma(\beta)$ [deg]	n
60 d	Box 1	19	18.4	1.7	15	83
60 d	Box 2	69	67.6	5.7	56	95
Prior	Box 3	21	18.3	3.6	16.6	20
60 d	Box 3	38	29.3	9.5	52	11

Table 5.3: Loma Prieta stress tensor inversion results. $\overline{\beta}_{Bst}$ is the mean average misfit angle of the bootstrap samples, $\sigma(\beta_{Bst})$ the standard deviation based on our approach and $\sigma(\beta)$ the standard deviation of *Michael* (1987a).

tured a steeply dipping fault, located to the southwest of the main surface trace of the San Andreas fault (*Eberhart-Phillips and Michael*, 1998). Aftershocks occurred in the volume surrounding the primary fault plane with few events re-rupturing the main-shock fault plane (*Dietz and Ellsworth*, 1990). First motion focal mechanisms determined using 1D- and 3D-velocity models reveal a diverse set of faulting styles ranging from normal, right- and left-lateral, to reverse faulting earthquakes (*Oppenheimer*, 1990; *Eberhart-Phillips and Michael*, 1998). Right lateral and reverse faulting mechanisms predominate the overall solutions. In the northern part of the rupture zone thrust faulting events become more abundant. This is consistent with finite-fault source models which indicate a higher portion of reverse slip to the north (*Beroza*, 1991; *Wald et al.*, 1991).

We selected a 10 km wide cross section (Figure 5.4a) perpendicular to the San Andreas fault and computed the stress tensor prior to and in the 60 days following the Loma Prieta main shock (121.95°W /37.053°N − 121.872°W /37.125°N). Since no events were located at shallow depths prior to the main shock in this part of the San Andreas fault zone, the comparison is only possible for the deep section (d $\geq$ 10km). The stress tensor prior to the main shock shows a thrust to right-lateral strike-slip regime with the maximum compressive stress axis σ_1 oriented about N9°E (Figure 5.4c). The stress field is relatively uniform with a misfit angle of $\beta = 21° \pm 3.6°$. A relatively uniform stress field remains in the shallow region

after the main shock ($\beta = 19° \pm 1.7°$) with approximately the same horizontal compression (Figure 5.4b). The stress field in the deep section exhibits a very high misfit angle of $\beta = 69° \pm 5.7°$, confirming the heterogeneous stress field caused by the main event (*Michael et al.* (1990); *Eberhart-Phillips and Michael* (1998), Figure 5.4e). In the footwall where seismicity occurred before the main shock (box 3), the heterogeneity also increases to $\beta = 38° \pm 9.5°$; however, the misfit angle remains below the threshold we use to define a heterogeneous stress field.

To go beyond earlier studies based on selective regions, we spatially and temporally map the properties of the aftershock sequence and the local stress field. We use cylindrical volumes normal to the fault plane (radii $r = 3 - 5\,\mathrm{km}$) and tested data from time periods ranging between 1-14 years. The NW–SE extent matches the dimensions of the finite-fault source model defined by *Beroza* (1991) (Figure 5.5a). Aftershocks where selected in a 15 km wide cross section around the 70° dipping fault plane extending from 121.054°W /37.16°N to 121.71°W /36.92°N. Our results confirm the findings of previous studies. They also reveal a heterogeneous stress field in the deeper section of the fault plane, below 10 km, with a lateral extent of about 15 km (Figure 5.5c). The spatial extent of the highly heterogeneous stress field patch ($\beta \geq 50°$) covers approximately the regions of highest slip during the main shock, supporting the HPSSF-hypothesis. When compared to other finite-fault source models, this conclusion holds since the slip models are similar in the distribution of slip though not in the slip partitioning between the ruptured asperities to the northwest and southeast of the hypocenter (*Hartzell et al.*, 1991; *Steidl et al.*, 1991; *Wald et al.*, 1991). This highlights difficulties determining the complex slip distribution of the main shock, but does not affect our interpretation. The stress field is rather homogeneous at shallow depth ($\beta \leq 30°$). Adjacent to the regions of highest slip, the stress field becomes homogeneous to the southeast with $\beta \leq 35°$ and similarly to the northwest with $35°\beta \leq 45°$ (Figure 5.5c) in regions

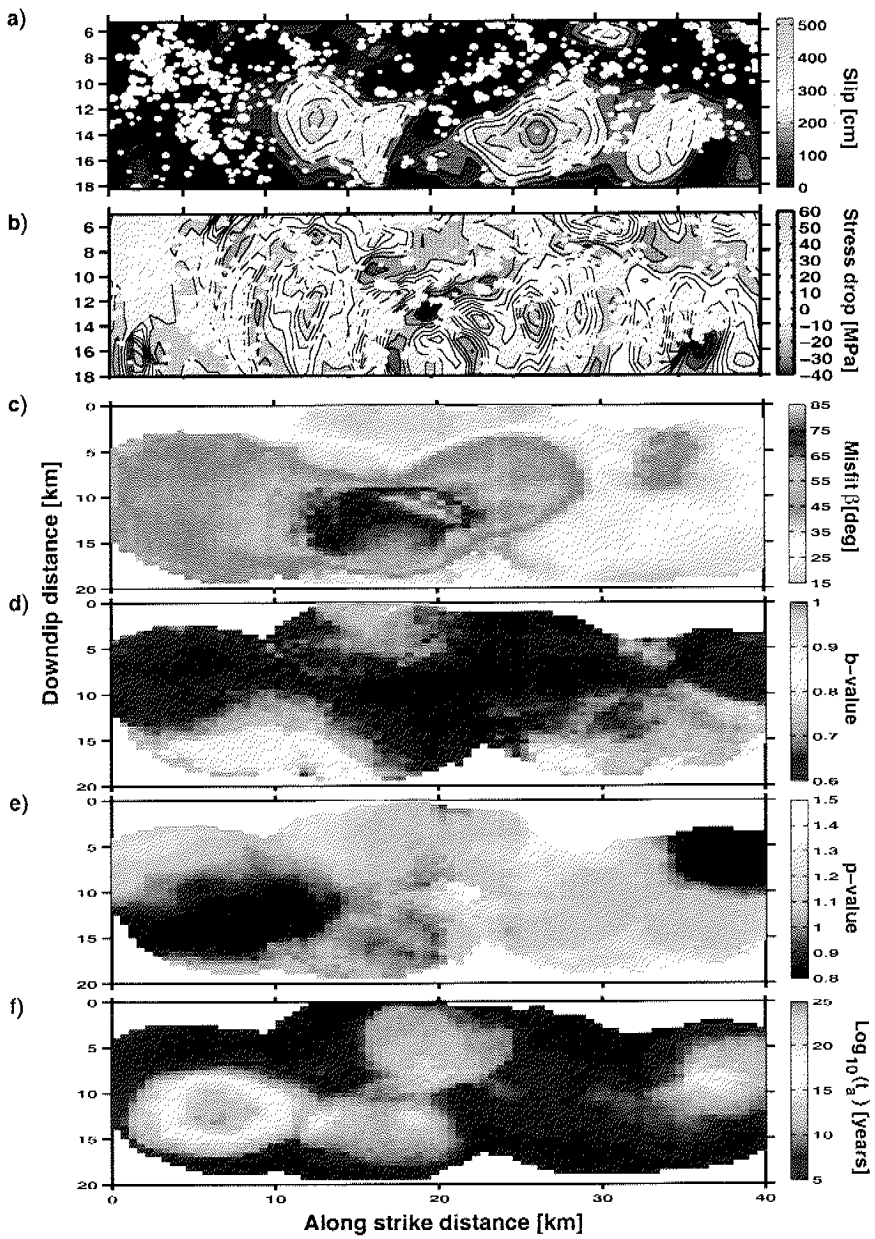

Figure 5.5: Cross section of the 1989 Loma Prieta earthquake: a) the finite-fault source model by *Beroza* (1991) and b) stress-drop distribution scaled by the 1D-velocity model (*Beroza*, 1991) superimposed with aftershocks of the NCSN-catalog ($M \geq 1.4$), c) average misfit angle $\beta\,[deg]$ from stress tensor inversion, d) b-value, e) p-value, f) aftershock duration t_a. Radius for mapping is $r = 5\,\mathrm{km}$, period $t = 5\mathrm{year}$.

with smaller slip values.

Mapping b- and p-value distributions for the Loma Prieta earthquake reveals relatively small values of both parameters ranging from 0.6 to 1.0. Larger values are found in the lower crust near the bottom of the seismogenic zone. Smallest b-values are found in regions of high heterogeneity and, qualitatively, outside regions of highest slip. We used the NCSN-catalog with a magnitude of completeness $M_c = 1.4$ in the first 3 days of the sequence and thereafter magnitudes above $M_c = 1.2$ based on the EMR-approach (*Woessner and Wiemer*, 2005). These values are higher compared to *Gerstenberger* (2004), who used methods presented by *Wiemer and Wyss* (2000). In both analyzes, the completeness level is high shortly after the main shock and rapidly decreases in the first hours after the main shock, reaching a constant level starting about three days after the event. A complicating aspect in Loma Prieta aftershock sequence is a break in the slope of the frequency-magnitude distribution at magnitude $M = 4$ (Figure 5.6). We agree with *Gerstenberger* (2004) who argues that the break in slope is not a completeness determination error, but rather a consequence of other factors influencing the frequency-magnitude distribution: First, the sequence was not very productive with only one magnitude 5 event which can affect the maximum likelihood estimate. Second, in the northern section, a swarm like activity is detected with a large number of $3 \leq M \leq 4$ events. Third, and most important, the NCEDC provides a preferred magnitude in which events of $M_L < 3.5$ are reported using the local magnitude scale that saturates at $M_L = 4.5$. Alternative magnitudes, if available, are used following a specific rating scheme (see documentation of the NCEDC at `http://quake.geo.berkeley.edu/ftp/pub/doc/ncsn/shadow2000.pdf`), and duration magnitude or moment magnitudes are used for events $M_L \geq 4$. Thus, the slope of the Gutenberg-Richter law might be underestimated in many cases due to the different magnitudes used in

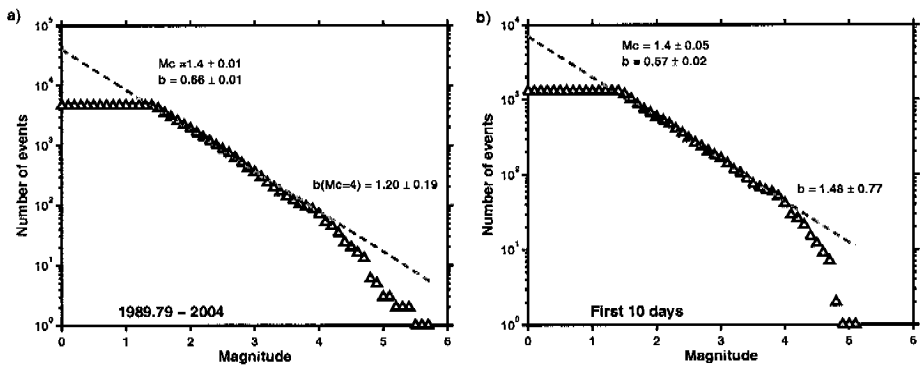

Figure 5.6: Frequency-magnitude distributions of the Loma Prieta for a) the period 1989.79-2004 and b) the first 10 days of the aftershock sequence. Note the break in the slope at magnitude $M = 4$.

the catalog. The change in the b-value using events above the completeness level $M_c = 1.4$ and events above a threshold of $M \geq 4$ is about $\Delta b = 0.3 - 0.6$, depending on the time period and region (Figure 5.6). Correlations with other parameters are, based on these probably biased b-values and their interpretation are highly speculative to interpret or may lead to unreliable conclusions.

The magnitude calibration problem is not important for the determination of p-values for which the temporal sequence is decisive. p-values spatially vary between 0.8 and 1.5. In areas of $p \geq 1.3$, neither the Omori law nor nested Omori models fit the sequence based on a Kolmogorov-Smirnov test (*Woessner et al.*, 2004a). Small values ($p \leq 0.9$) are obtained near the northern end of the ruptured plane at depths between 10-16 km and at shallow depths near the southern end of the cross section. These regions cover areas of main shock faulting that experienced little to no slip during the main shock and show a rather homogeneous stress field.

In summary, we find that regions of stress tensor heterogeneity and regions of high slip qualitatively coincide in support of the HPSSF-hypothesis. In contrast to hypothesis H_1, b-values are not correlated (correlation coefficient $r^2 = 0.04$) to β,

but here the magnitude inconsistencies prevent us from drawing final conclusions.

5.3.2 The 1992 Landers earthquake

We spatially and temporally map the stress tensor parameters for the aftershock sequence of the $M_W = 7.3$ Landers earthquake that occurred on the 28 June 1992. Figure 5.7a shows the misfit angle β as colormap in the background for the first year of data and the orientation of the maximum compressive stress σ_1 superimposed as black lines, determined on a $0.01° \times 0.01°$ grid and using a radius of $r = 5$km to sample events. We require at least 50 events at each node for the stress tensor inversion. Additionally, the surface traces of the planes in the finite-fault source model by *Wald and Heaton* (1994) are shown (thick grey lines). Throughout the Landers rupture zone, the misfit values are relatively high ($\beta \gtrsim 40°$) which emphasizes the disturbance of the local stress field due to the large earthquake. In agreement with *Hauksson* (1992), the stress tensor heterogeneity measure β increases from south to north, with the largest misfits found along the Emerson fault and the cross-over between the Emerson and the Homestead Valley fault (Figure 5.7). The same pattern is also shown in a fault parallel cross section (Figure 5.8). The superimposed lower hemisphere stereonet plots show examples of the stress tensor inversion from two locations: (1) is located along the Emerson fault in a region of complex fault structure and (2) is located along the Johnson Valley fault with a simpler fault system. At location 1 and 2, misfit angles of $\beta = 70.20° \pm 4.60°$ and $\beta = 33.06° \pm 1.70°$ are determined, respectively.

The style of faulting in the Eastern California Shear Zone (ECSZ) is predominantly strike-slip. Along the faults that ruptured during the Landers event, the ratio between thrust, normal and strike–slip type aftershocks to the overall number of events varies spatially. The largest diversity of faulting styles is found near the intersection of the Emerson/Homestead Valley fault, where we find the largest

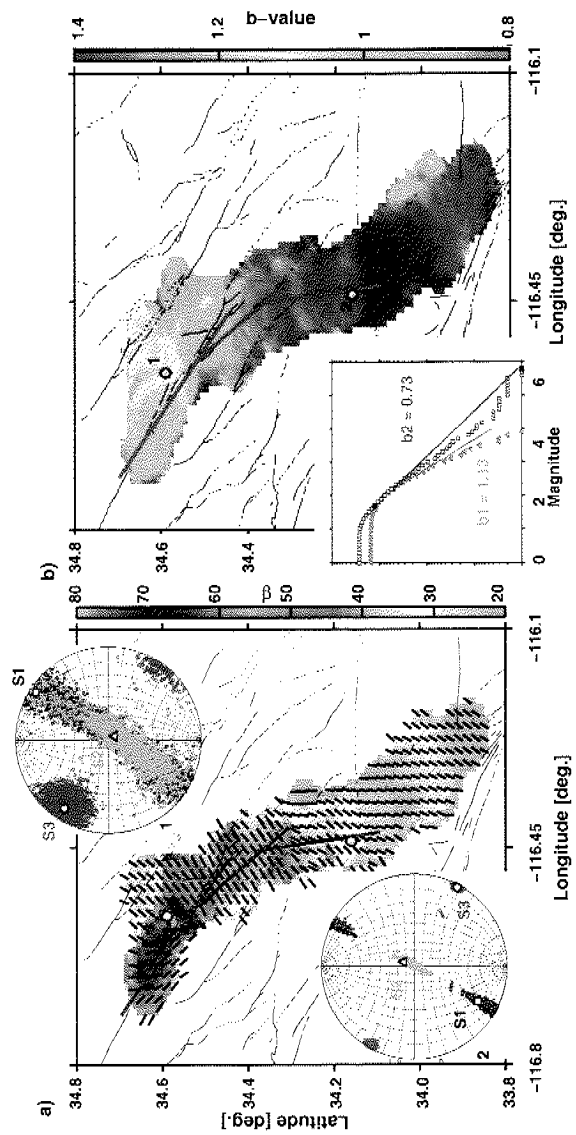

Figure 5.7: a) Misfit angle β (colored background) superimposed with the orientation of the maximum compressive stress axis σ_1 axis (black lines) determined from the stress tensor inversion and b) b-value map for the 28 June 1992 Landers earthquake of the first year of the aftershock sequence. Example stereonet plots of the stress tensor inversions width low and high heterogeneity and two frequency-magnitude distributions with illustrating low and high b-values.

fractions of thrust and normal faulting events. The diversity of different faulting styles also coincides with the geometrical complexity of the fault system which is highest in the area of the fault intersections and decreases to the south along the Johnson Valley fault. The location of the largest β values therefore corresponds to the complexity of the mapped fault system and fault rupture (Figure 5.7a and 5.8c, (*Liu et al.*, 2003)). In the cross-sectional view, the correspondence of the largest slip patches and the spatial pattern of the stress field heterogeneity is not as convincing as for the Loma Prieta sequence. Nonetheless, when considering the uncertainties in the main-shock slip distribution, we nevertheless argue that high β-values are found in the vicinity of high-slip regions.

Similar spatial patterns are obtained for the b-value pattern: high b-values ($b \geq 1.1$) in the northern section of along the Camp-Rock and Emerson fault, smaller values of $b \leq 0.9$ along the Homestead and Johnson Valley fault with decreasing values southward (Figure 5.7b and Figure 5.8d). These results are found for different earthquake catalogs, using either a fixed minimum magnitude of completeness M_c or a variable M_c determined at each grid node (*Woessner and Wiemer*, 2005, EMR-method) and are in agreement with previous studies (*Wiemer and Wyss*, 1997, 2002). The map in Figure 5.7b shows the result on the same grid as used for the stress tensor inversion computations ($0.01° \times 0.01°$, radius $r = 5$km) with a minimum of 100 events required for the b-value determination. The frequency-magnitude insert in Figure 5.7b illustrates the differences in b at locations 1 and 2. At location 1, small events are more abundant relative to large ones as a larger b-value is determined. In general, the productivity is smaller to the north than to the south.

The b-values and the parameters describing the stress tensor heterogeneity appear to be correlated in the Landers case. We speculate that b-values correlate linearly with the stress field heterogeneity, measured by the misfit angle β in the

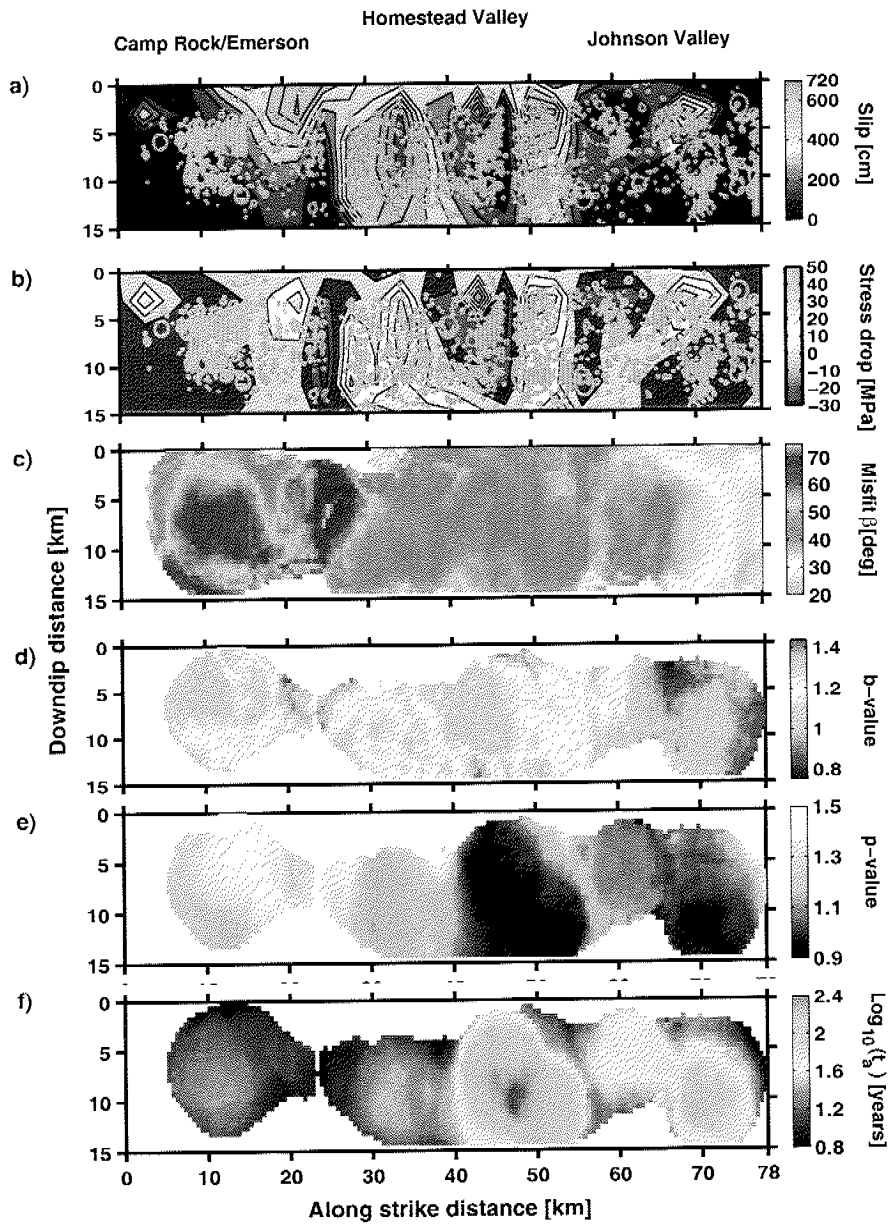

Figure 5.8: Cross section of the Landers earthquake according to the dimensions of the Wald finite-fault source model. a) Slip and b) stress-drop distribution superimposed by aftershocks of the relocated catalog Hauksson catalog above magnitude $M = 2.1$ for 11 years. c) Misfit angle β, d) b-value, e) p-value for the first year of aftershocks and f) logarithmic aftershock duration t_a based on 11 years of data.

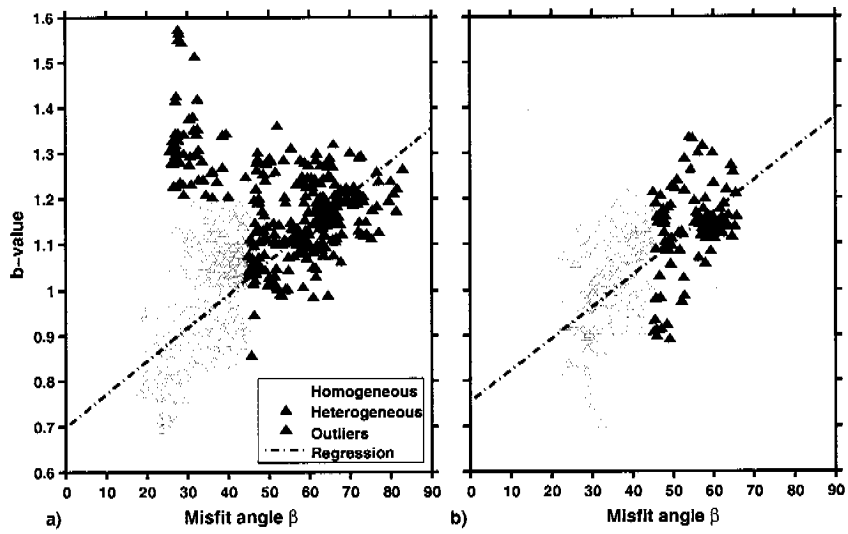

Figure 5.9: b-value as a function of misfit angle β sampled for a) the map view grid and b) the cross-sectional view.

proximity of a fault that ruptured during a major earthquake. Figure 5.9a and 5.9b display b as a function of β as determined from the grid nodes in map view and from the cross section (Figure 5.8). The cross section corresponds to the extent of the finite-fault source model by *Wald and Heaton* (1994). In the map view panel (Figure 5.9a), outliers are plotted with black triangles. These outliers originate from events off the main shock faulting area on faults called Iron Ridge and Argos faults (*Hudnut et al.*, 1994), thus these are from outside the region of main slip. The data plotted in both panels show a positive linear correlation of the b-value and the misfit angle β with correlation coefficients of $r^2 = 0.63$ and $r^2 = 0.35$ for the map and cross-sectional view, respectively. For the map view, we removed the outliers to compute the correlation. According to our definition for the stress field heterogeneity, white and filled grey triangles separate low ($\beta \leq 45°$) and high misfit regions.

In addition to the parameter of the frequency-magnitude distribution, we mapped the p-value distribution on the cross section corresponding to the Wald fault model

ranging from 0.9 to 1.5 (Figure 5.8e). Similar to the b-value distribution, higher p-values are found to the north indicating a faster decay. Smallest values are found in the center of the Homestead Valley fault and at the southern end of the Johnson Valley fault. Both of these regions approximately correspond also to regions of increased shear stress (Figure 5.8b).

Summing up the results for the Landers earthquake, we find evidence for the correspondence of high slip and high stress heterogeneity values considering the uncertainties in the slip distribution. Throughout the main shock rupture zone we find β-values above $45°$ in support of the HPSSF-hypothesis. β- and b-values are positively correlated and thus support our hypothesis H_1, but the correlation coefficients are rather small. A relation to the geometrical complexity of the fault system or a more fundamental relation of the b-value to differential stresses (*Schorlemmer and Wiemer*, 2005) cannot be excluded with this approach.

5.3.3 The 1999 Hector Mine earthquake

The $M_W = 7.1$ Hector Mine earthquake occurred about seven years after the Landers event and caused surface rupture in the eastern California shear zone (*Rymer et al.*, 2002). Like the Landers earthquake, the Hector Mine quake ruptured multiple faults, some of which had not been mapped before. The geometrical complexity is a challenge for the approach we pursue and could significantly influence our final conclusions. Aftershock properties, their implications for aftershock hazard and the observation of stress field heterogeneity were discussed by *Wiemer et al.* (2002), but they did not conduct a depth dependent cross sectional analysis.

The geometrical complexities of the rupture are reflected in the pattern of the aftershock seismicity and in finite-fault source models (*Ji et al.*, 2002b; *Jónsson et al.*, 2002; *Kaverina et al.*, 2002). We analyze the aftershock sequence along the strike of the combined model by *Ji et al.* (2002b) using the relocated data set by

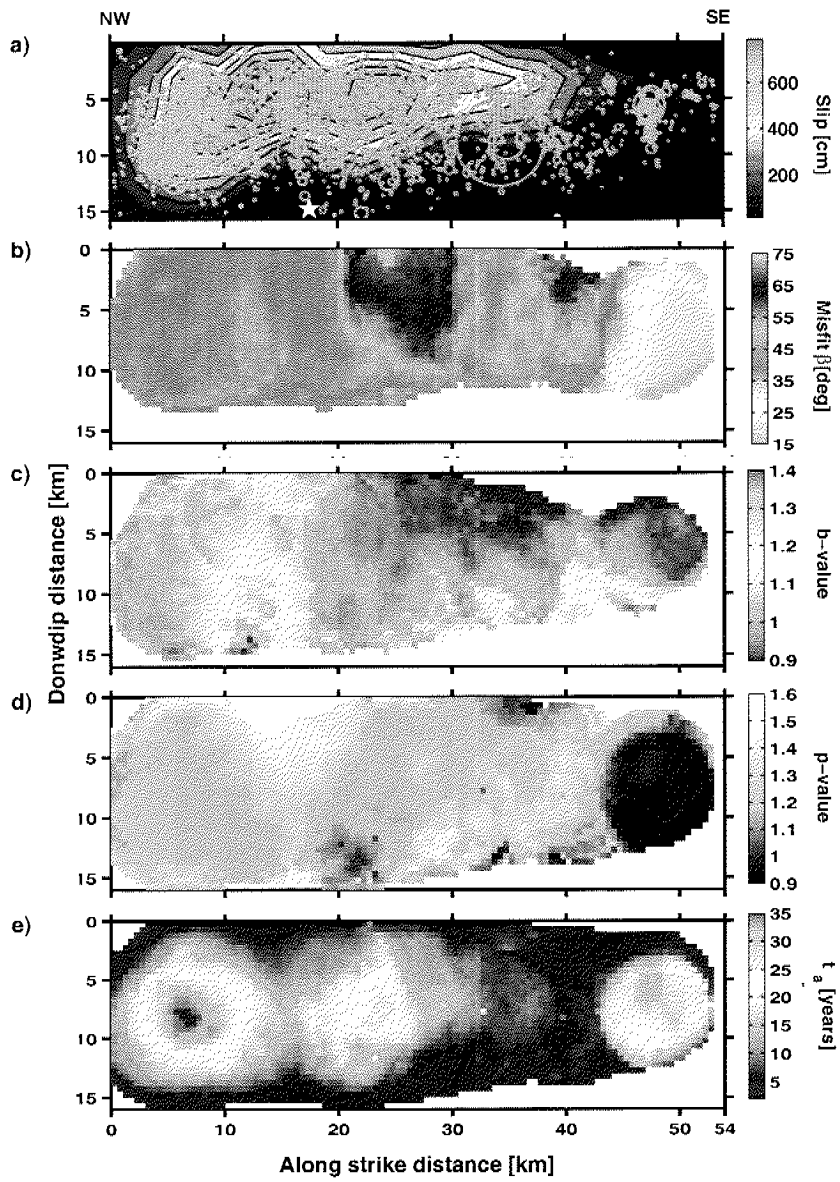

Figure 5.10: Cross-sectional view of the Hector Mine earthquake according to the dimensions of the *Ji et al.* (2002b) finite-fault source model. a) Slip distribution superimposed by aftershocks of the relocated catalog Hauksson catalog above magnitude $M = 2.1$. b) Misfit angle β, c) b-value, d) p-value for the first year of aftershocks and e) aftershock duration t_a based on 5 years of data.

Hauksson (2000) and the general SCSN catalog ($M_c = 2.4$ in the first 3 days, later on $M_c = 2.1$). We also analyzed the sensitivity of the results to varying radii of the cylindrical volumes and to different width of the swath around the fault plane for which aftershocks are projected on the fault plane. We find that results are stable for a swath width of 8 km and 5 km radius (Figure 5.10).

The cross-sectional view shows a central area of high misfit angles $\beta \geq 45°$, smaller values to the northern end ($35° \leq \beta \leq 45°$), and the lowest values at the southern end $\beta \leq 35°$. The region of highest heterogeneity in the local stress field coincide with the regions of high slip but also with the intersection of the different fault branches of the main shock. In addition, the northern part of the Hector Mine main shock rupture exhibited large slip values that correspond to values of β that, according to our definition, are not heterogeneous. We cannot exclude that the fault zone complexity may have the same influence on β as the slip distribution. Therefore, the first order observation that heterogeneity is related to high slip patches is only weakly supporting the HPSSF-hypothesis.

Comparing the b-value to the β-value distribution does not exhibit a positive linear correlation as we found for the Landers event, and thus does not support our hypothesis H_1. An analysis using the fault branches of the finite-fault source models separately might allow to obtain a more detailed picture on the relation between the b-value and the β-value.

b-values and p-values do not follow a similar pattern. In general, both are in the upper ranges of the scale observed for these parameters for crustal seismicity ($b \geq 0.9$ and $p \geq 0.9$). The highest values of the b-value ($b \geq 1.2$) are found in the northern section at depths below 10 km, the smallest values in the central region at shallow depth in the cross section. In contrast, the highest p-values are found in the northern part of the cross-section at shallow depths ($d \leq 7\,\mathrm{km}$) and the smallest

values to the south ($p \leq 1.1$).

In summary, the analysis of the Hector Mine aftershock sequence shows only weak support for the HPSSF-hypothesis and no support for hypothesis H_1 on the relation between b-values and β, the correlation coefficient being $r^2 = 0.002$. Fault system complexity or other physical mechanisms may have played an equally important role for this earthquake.

5.3.4 The 1984 Morgan Hill and the 2004 Parkfield earthquake

In the previous sections, we analyzed two M7-type earthquakes and locally found highly heterogeneous stress field conditions following the main shocks. We now focus on two moderate sized M6-type earthquakes to examine if the HPSSF-hypothesis holds for: 1) the 1984 $M_W = 6.1$ Morgan Hill earthquake that ruptured the Calaveras fault (Figure 5.11) and 2) the 2004 $M_W = 6.0$ Parkfield event that ruptured Parkfield segment of the San Andreas fault zone (Figure 5.12). Besides the smaller size, these events occurred on fault segments that are geometrically less complex than the faults ruptured by the M7-type earthquakes. The fault segments are characterized by highly organized seismicity that forms streaks, holes and repeating events on the same locations (*Waldhauser et al.*, 2004; *Schaff et al.*, 2002).

We mapped the average angular misfit β using the focal mechanism catalog of the NCSN in cylindrical volumes of 5 km radius, using a period of 5 years for the Morgan Hill event and up to the 16 June 2005 for the Parkfield main shock. Both cross sections show small misfit values ($\beta \leq 25°$) which is consistent with the relative similarity of the focal mechanisms. The underlying data set does not allow us to resolve if the high slip patches defined in the finite-fault source models of the Morgan Hill main shock (*Hartzell and Heaton*, 1986; *Beroza and Spudich*, 1988) or the Parkfield main shock (*Ji et al.*, 2004; *Dreger et al.*, 2005) correlate with spots of higher heterogeneity. Hence, we infer that the local stress field was not significantly

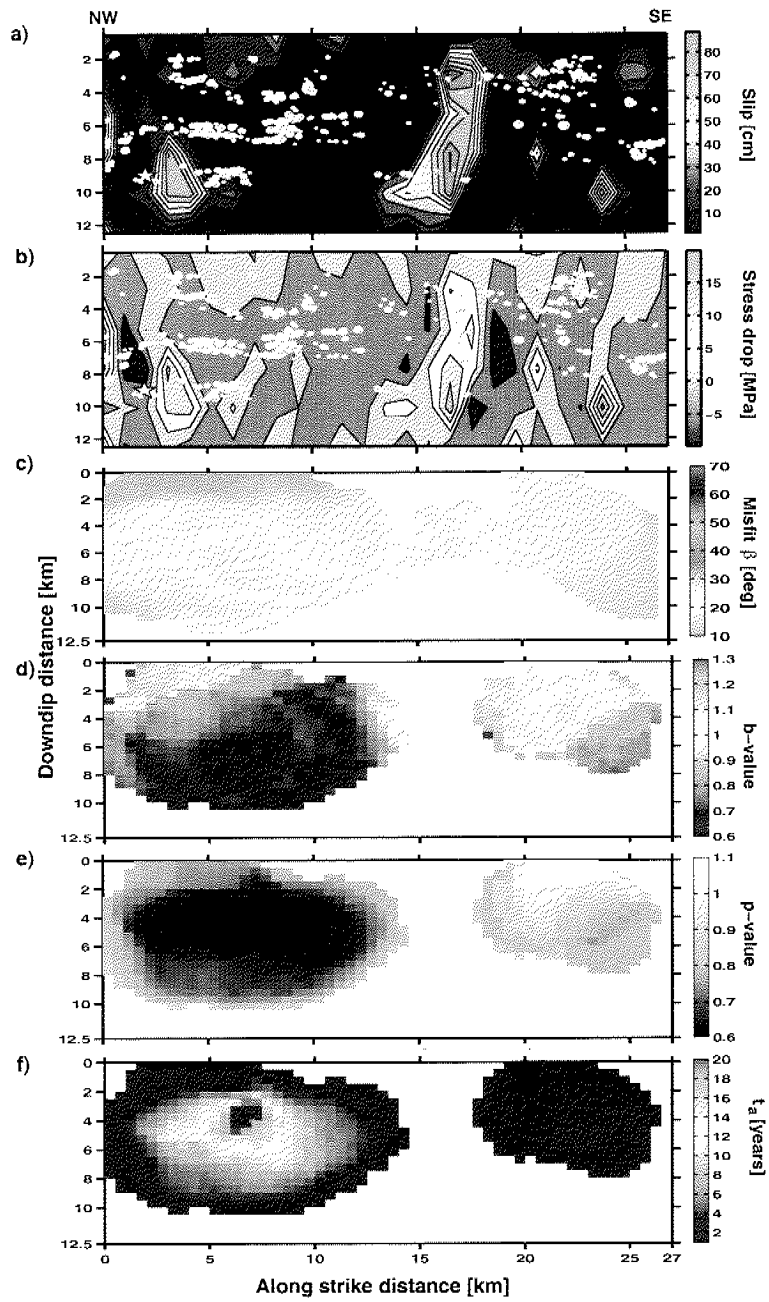

Figure 5.11: Cross section of the Morgan Hill earthquake according to the dimensions of the Hartzell finite-fault source model. a) Slip and b) stress-drop distribution superimposed by aftershocks of the relocated catalog by *Schaff et al.* (2002) catalog above magnitude $M = 1.4$ for 5 years. c) Misfit angle β, d) b-value, e) p-value for the first year of aftershocks and f) aftershock duration t_a based on 5 years of data.

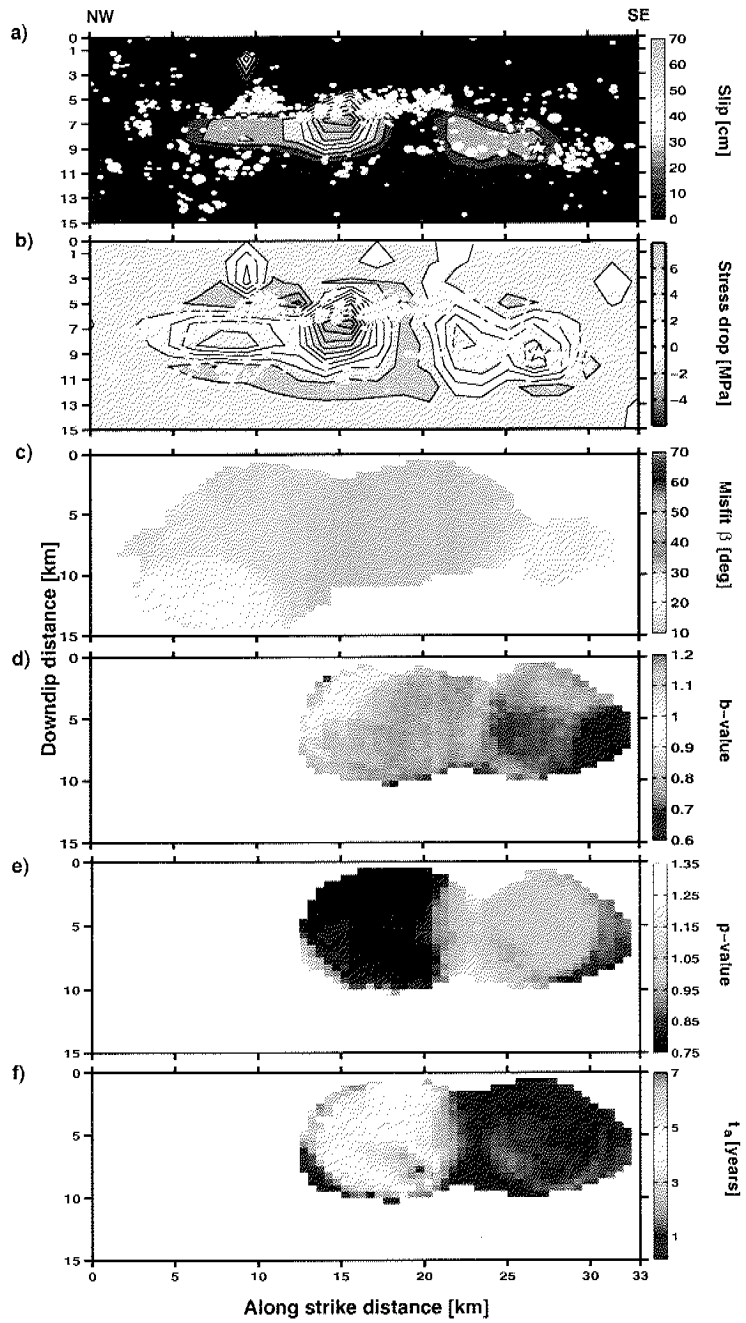

Figure 5.12: Cross section of the 2004 Parkfield earthquake according to the dimensions of the Ji finite-fault source model. a) Slip and b) stress-drop distribution superimposed by aftershocks of the NCSN catalog ($M \geq 1.2$). c) Misfit angle β, d) b-value, e) p-value for approximately the first year of aftershocks and f) aftershock duration t_a.

disturbed by the main shocks. This suggests that both main shocks released only a minor portion of the existing background stress level or that the state of stress along the strike-slip faults in northern California has a much smaller heterogeneous component.

The b- and p-value cross sections are computed using the relocated catalog by *Schaff et al.* (2002) ($M_c = 1.4$) for the Morgan Hill and the NCSN catalog in the Parkfield case, selected for the same periods as for the focal mechanism catalog. Based on a temporal analysis of the Parkfield sequence, the catalog was cut at $M_c = 1.4$ in the first six days following the main shock and at $M_c = 1.2$ in the later period. The b-values at Parkfield are mainly smaller than $b \leq 0.9$ and are not significantly different based on Utsu's test from the values before the main shock matching the stationarity hypothesis posted for Parkfield by *Schorlemmer et al.* (2004a); *Woessner et al.* (2004b). The b-value distribution of the Morgan Hill event can be divided in two regions: 1) b-values above 0.9 in the shallow crust ($d \leq 6\,\mathrm{km}$) to the southeast and close to asperity mapped in the finite-fault slip model (*Hartzell and Heaton*, 1986). 2) b-values below 0.8 are observed to the northwest above 9 km depth and coincide with regions of low-slip in which most of the aftershocks are located (see Chapter 4). Using the relocated catalog, we cannot confirm conclusively that the high b-value region spatially correlates with the asperity as claimed in *Wiemer and Katsumata* (1999). However, we confirm higher b-values for aftershocks located along this part and the lack of correlation may be caused by uncertainties in the slip distribution. Similarly to the dataset of the Loma Prieta earthquake, the frequency-magnitude distribution shows a break in slope at magnitude 3.5 which may lead to underestimate b-values.

Summing up the results for the moderate sized earthquakes, we do not find a heterogeneous post-seismic stress field following the M6-type main shocks. This

No	Event	R_b [1/year]	r [km]	M_{th}	t_a [years] min/mean/max	$t_a(all)$ [years] min/mean/max
1	Morgan Hill	53.80	4	1.4	0.72/ 4.32/ 21.4	1.43/ 1.89 / 2.28
2	Loma Prieta	15.21	5	1.2	1.49/ 8.57/ 23.9	9.30/ 10.58 / 12.38
3	Landers	6.27	5	2.4	5.75/ 43.3/ 251	28.33 / 35.20 / 63.2
4	Hector Mine	14.12	5	2.1	2.44/ 13.2/ 36.4	21.73/ 31.05 / 38.65
5	Parkfield	127.05	5	1.4	0.26/ 1.71/ 7.5	0.54/ 0.76 / 1.25

Table 5.4: Parameters for the spatial aftershock durations determined in the dimensions used. R_b is normalized by the area in the computation, r the radius to sample data in cylindrical volumes, M_{th} is the magnitude threshold, t_a denotes the aftershock duration range obtained on the grid, $t_a(all)$ the range obtained for the entire sequence.

indicates that these events did not release a large portion of the background stress field and cannot be used as a real test for the HPSSF-hypothesis. Alternatively, the stress conditions along strike-slip faults in central California may have a very small heterogeneous component.

5.4 Results II: Duration of aftershock sequences and their relation to the temporal dependence of β

In this part, we demonstrate the spatial variability of aftershocks sequence durations, their relation to the above discussed seismicity parameters and to the overall length of aftershock sequence duration. We present results of the temporal dependence of the misfit angle β and discuss the results with respect to the duration of aftershock sequences.

5.4.1 Spatial variable aftershock sequence duration

We transformed the detailed mapping of the Omori law parameters into a spatial estimate of local aftershock duration (Figures 5.5f, 5.8f, 5.10d, 5.11f, and 5.12f). For each event, we estimated the background rate from a declustered catalog that matches the dimensions of the cross section used for the mapping. The cross-sectional views exhibit strong spatial heterogeneities for moderate sized as well as large events. Overall, the aftershock sequences last for periods ranging between

a few days in case of the 2004 Parkfield earthquake to a few hundred of years in the 1992 Landers case.

The background rate estimated for the Landers earthquake based on the relocated catalog of about 8 years is small resulting in very long t_a. Estimating R_b at $M_{th} = 2.4$ from the SCSN catalog reaching back to 1932 (see `http://www.data.scec.org/`) in a polygon comprising the entire Landers fault system, for which this low threshold level is not reached before the mid eighties, we obtain a rate of 10.32 events per year instead of 6.27 estimated for the swath (Figure 5.8f). Using a polygon enclosing the first six months of the Landers aftershocks, we obtain background rates of about 15.42 events per year for the relocated catalog which leads to an estimate for the aftershock sequence duration between 7.6 - 13.69 years including the uncertainties in the modified Omori law. For a 10 km wide swath, the t_a values in the range of 17.74 - 30.32 years when using R_b from the swath, and values ranging from 5.25 - 14.78 years when applying R_b values derived from the polygon. The estimates are strongly dependent on the choice of data.

The background rate estimates for the Hector Mine event based on the relocated catalog, although declustered, seem to be rather high since the rate is influenced by the Landers event. Selecting events in a polygon based on the first six months of the Hector Mine earthquake sequence, we obtain $R_b = 14.12$ per year, and $R_b = 5.48$ per year is estimated for the catalog back to 1932 ($M_{th} = 2.1$, events missed in the period before 1985). The largest seismicity rates are found on the Parkfield section which also shows the shortest sequence duration.

The maximum time periods of aftershock sequences following the moderate-sized main shocks along the Parkfield segment of the San Andreas fault and on the Calaveras fault are of shorter duration (0.2–25 years) compared to the durations estimated for the earthquakes in the Mojave desert (2–251 years). The shorter durations

for the main shocks in central California are consistent with the higher background seismicity as compared to the seismicity in the ECSZ prior to the events in 1992 and 1999 (Table 5.4). The patterns of aftershock duration primarily display the patterns observed for p-values: the smaller the p-values, the larger the sequence duration t_a. Though this seems trivial, we could not *a priori* exclude that the productivity k could have a similar influence. Using different time periods, we found that the p-values increase slightly with time, which reduces the expected aftershock duration when using longer period data sets (*Felzer et al.*, 2003; *Felzer and Brodsky*, 2005; *Helmstetter and Sornette*, 2002).

The range of aftershock durations determined from spatial mapping and the aftershock length for the entire selected regions $t_a(all)$ are in general comparable (Table 5.4). The uncertainties for $t_a(all)$ are computed using a bootstrap approach for estimating the modified Omori law parameters (*Woessner et al.*, 2004a). The overall sequence durations tend to be around the mean values of the spatially mapped t_a results. For the 1992 Landers earthquake, *Toda et al.* (2005) computed aftershock lengths ranging from 20-53 years, *Gross and Kisslinger* (1997) provided estimates ranging between 2.27 and 7.58 years based on the modified Omori law. Based on a rate and state friction model, these authors argue that there would be significantly increased activity for about 15 years following the Landers event. For the Loma Prieta event, *Dieterich* (1994) estimated 1.7-3.5 years which is shorter than our overall estimate and at the low end of what we obtain for the cross section. The longer aftershock durations that we map for the Loma Prieta earthquake are in agreement with the time-dependent hazard model by *Gerstenberger et al.* (2005) which still shows elevated probabilities of strong shaking in this regions. Considering the overall agreement of mapped and entire sequence aftershock sequence durations, we conclude that the cross-sectional analysis is a viable tool for detecting regions were increased seismicity is locally more pronounced and longer lasting.

5.4.2 Temporal dependence of the stress tensor heterogeneity

The HPSSF-hypothesis predicts a sudden increase of stress tensor heterogeneity β in the immediate vicinity of the main shock rupture following immediately after the main shock. In the previous sections, we spatially mapped the heterogeneity parameter β and confirmed the increase of β using specified time periods. As a next step, we examine the temporal evolution of the stress field heterogeneity during the aftershock sequence. We test the hypothesis H_2 that the stress field recovers with time. We expect the angular misfit to decrease with time towards the values observed before the rupture.

We determine the stress tensor during the time period before the main shocks to establish a reference angular misfit. The data set for these periods is sometimes small ($n \simeq 20$), since we apply strict quality criterions for the stress tensor inversion. Likewise, we determine the stress tensor in periods following the main shock, requiring at least about $n = 100$ events and a period of at least 60 days after the main shock. To estimate the uncertainty in the angular misfit, we use the boostrap approach outlined in the method section. The standard deviation $\sigma(\beta_{BST})$ from the Monte Carlo approximation (500 samples) are used to determine the significance of the change. The time series $\beta(t)$ are computed using a moving window approach. Each window includes 50 successive events, the stepsize is 10 events. The resulting time series is non-linear because a constant number of events is used. Stability tests showed that 50 events are needed for reliable β estimates. For comparison, we computed the time series with non-overlapping windows and obtained almost identical results.

All time series uncover a significant sudden increase in β at the time of the main shock, whether they are computed for entire sequences or hot spots, i. e., the areas of highest β values, of large earthquakes (Figure 5.13 and 5.14). For the 1983

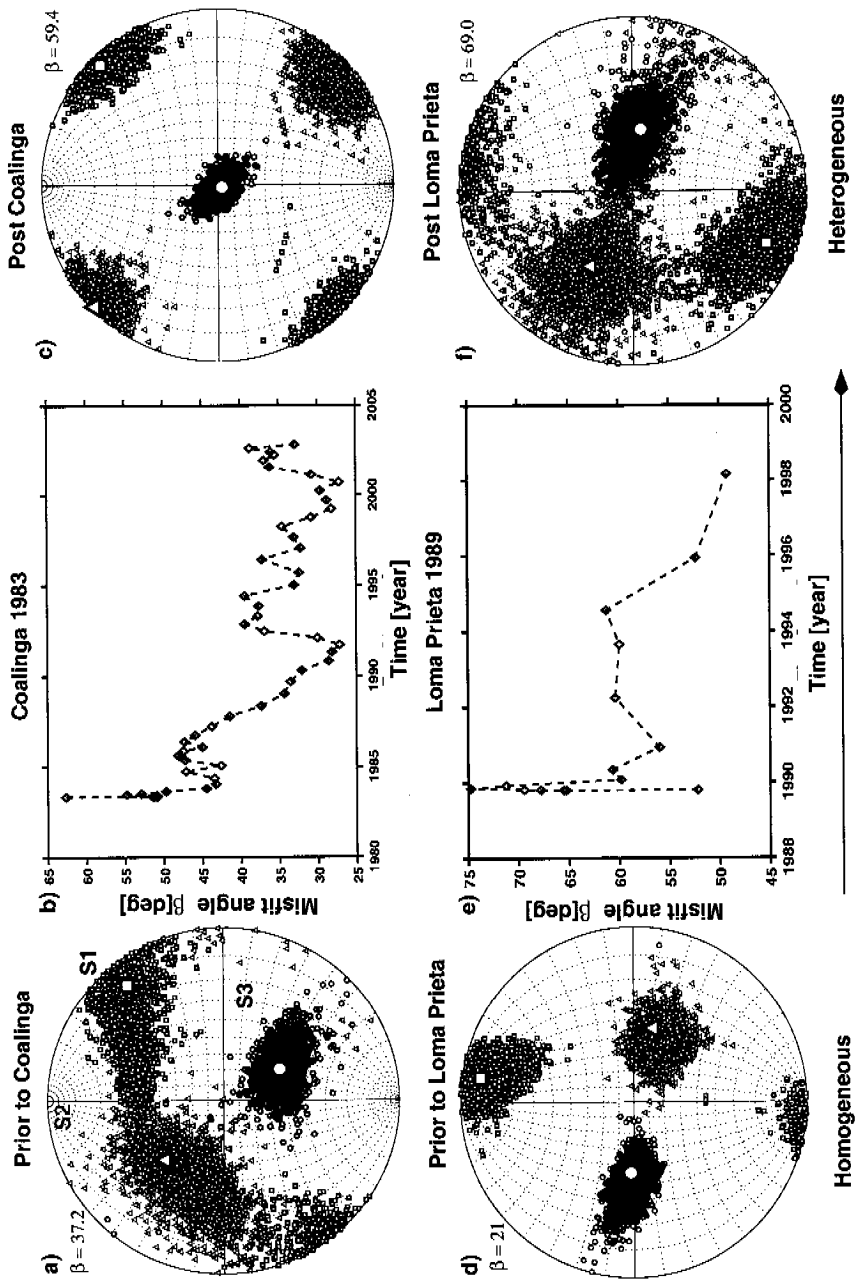

Figure 5.13: Temporal dependence of the stress tensor misfit angle β for the 1983 Coalinga and the 1989 Loma Prieta earthquake. Stress condition prior to the events (a and d), temporal evolution of $\beta(t)$ (b and e), and state of stress based on 100 events after the main shock (c and f) including about 80 and 60 days of aftershock focal mechanisms, respectively.

Coalinga and the 1989 Loma Prieta earthquakes, the time series include only the aftershock sequence for the period after the event, because the specified amount of 50 events is not available (Figure 5.13b and 5.13e) for the time period before. We computed the stress tensor and the β value for the earlier periods and obtain significant changes despite the small data sets before the events. For the Coalinga event, β jumps from $37.2° \pm 9.89°$ to $59.4° \pm 4.69°$, for the Loma Prieta from $21.0° \pm 1.7°$ to $69° \pm 5.7°$. Both time series show a gradual decrease of the β value, which is in agreement with our hypothesis of stress field recovery. The values of the Coalinga sequence decrease below the threshold of $\beta = 45°$ after about 2 years and stabilizes around $35°$ starting about 4 years after the main shock. We conclude that the influence of the Coalinga event on the stress field vanished after this time period. The angular misfit in case of the Loma Prieta event shows a strong increase right after the main shock, then a fast decrease shortly after the main shock and then it remains in a state that we define as heterogeneous since it is above the threshold level ($\beta \geq 45°$) and about twice as high compared to the stress state before the main shock.

Analog to the main shocks that occurred on the San Andreas fault system in northern California, the earthquakes rupturing the ESCZ caused locally heterogeneous stress fields in their immediate vicinity. The differences in the Landers fault zone range from $20°$ to $50°$ degrees, on the Hector Mine fault system β increased from $24.2°$ to $55.7°$ degrees, both showing significant deviations. The time series in the northern part of the Landers event, the Emerson and Camp Rock faults, as well as the spot around the intersection of the Lavic Lake and Bouillon fault of the Hector Mine event tend to decrease shortly after the main shock, whereas the Homestead valley fault stays at about the same level of $\beta = 45°$ until 2005. However, all three sections stay in a state above the threshold level, indicating that these regions are still in a heterogeneous state of stress. We are convinced that this feature is not an

artifact of the stress tensor inversion algorithm since β values provide stable estimates even when inverting a set of similar focal mechanisms (Figure 5.2).

The relationship between the Landers and the Hector Mine earthquakes was discussed in the special issue on the Hector Mine event (*Rymer et al.*, 2002). The Landers earthquake probably triggered the magnitude $M = 5.2$ Pisgah event in 1992 near the future epicenter of the Hector Mine main shock. Due to the stress transfer from the Landers earthquake, parts of the Lavic Lake and Bouillon fault were advanced to a more critical state of stress. The Hector Mine main shock may have nucleated in a region of increased Coulomb stress (*Stein*, 2003) although the level of Coulomb stress varies and can also be negative according to *Harris and Simpson* (2002). In the β time series for Hector Mine, we do not see a difference in the heterogeneity of the stress field following the Landers event. However, an increase in β is observed in the Landers time series that matches the time of the Hector Mine event (Figure 5.14b and 5.14e).

In summary, the time series demonstrate that the misfit angle decays fast from high β-values shortly after the main shock and then the decay slows down. This suggests that the stress regime recovers from the stress anomaly as the frequency of aftershock decreases and hints to a causal link between the decay of the anomaly and the occurrence of aftershocks (*Michael*, 1987b). The Coalinga event is the only example for which the β-level existing before the main shock is reached. Based on the same volume but using the general NCSN catalog, we estimated the aftershock duration of the Coalinga sequence. The background rate ($R_b = 2.485$, $M_{th} = 2.4$) is reached after about 22.07 years, or between 17.18–27.20 years considering the uncertainties in the modified Omori law parameters estimated from 1000 bootstraps (Figure 5.15). The estimated length of the sequence is rather long which could be a result of the small background rate based on the short data set (1967-1983) or an

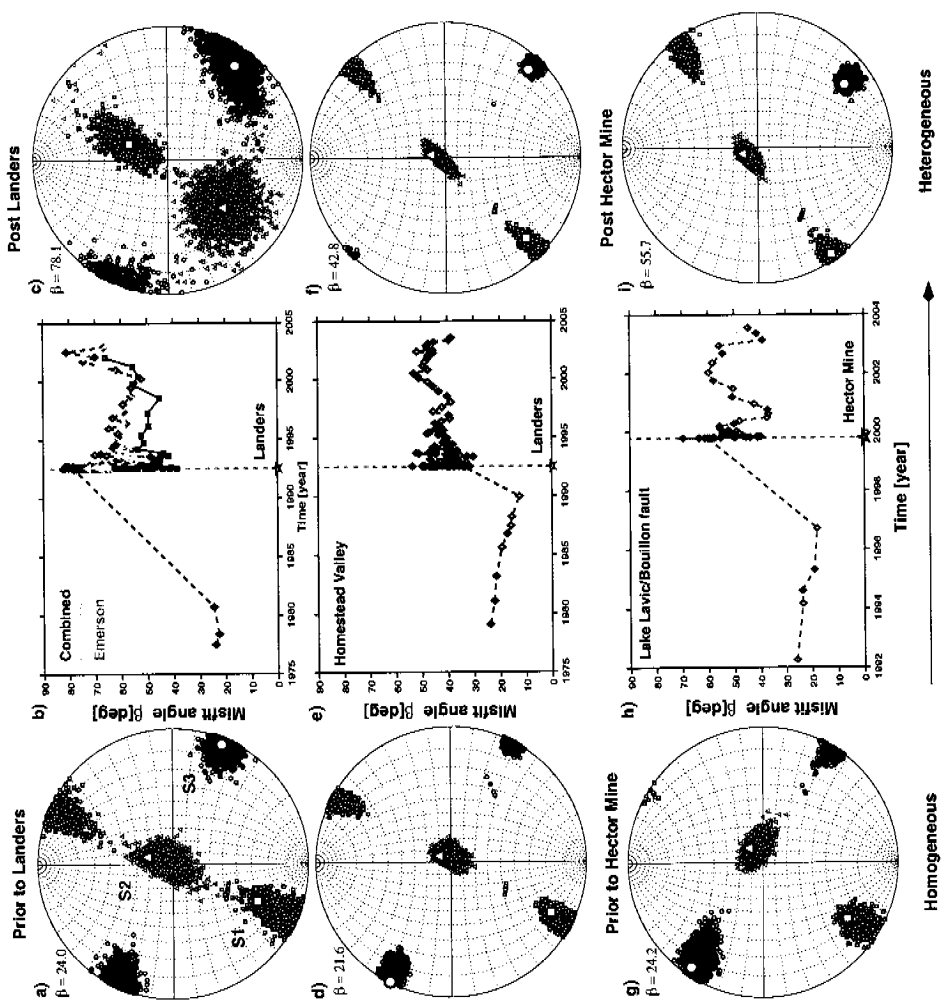

Figure 5.14: Temporal dependence of the stress tensor misfit angle β for the 1992 Landers (Emerson and Camp rock fault, separated and combined) and the 1999 Hector Mine earthquake. Stress condition prior to the events (a, d, g), temporal evolution of $\beta(t)$ (b, e, h) , and state of stress based on 60 days of aftershock focal mechanisms (c, f, i). For the Landers event, the northern fault sections according to the Wald model is used, for Hector Mine we selected a spot according to the highest heterogeneity between 20 and 30 km along strike and depths smaller than 12 km (see Figure 5.10b).

effect of declustering. However, even assuming higher background rates, the aftershock duration would be at least twice as long as it takes the β-value to decrease down to around 37°, the state before the main shock (Figure 5.13b) which is on the order of 2 to 4 years. An estimate for the other events in the study is not given since these have either not reached their respective background levels or, in the case of the Loma Prieta earthquake, the background rate in the volume of interest is not sufficient for a reliable analysis.

Taking into account the results of spatially mapping t_a, we observe that regions of largest t_a do no coincide with regions of largest stress field heterogeneity (Figures 5.5c and 5.5f, 5.8c and 5.8f, and 5.10b and 5.10e). The p-values in regions of high heterogeneity are generally high ($p \geq 1.2$) and consequently the local aftershock activity decreases rapidly. We can only speculate about the physical reason for the rapid decay in the regions of high stress field heterogeneity and attribute this to a faster healing of the crust compared to regions that were not disrupted as strong during the main shock.

5.5 Discussion and Conclusion

The analysis of aftershock sequences in the immediate vicinity of seismogenic faults with the focus on the HPSSF-hypothesis allowed us to confirm (1) that the largest heterogeneities in the stress field are in general concentrated in areas of highest coseismic slip and (2) that the heterogeneity β decreases with time. We present a first order conceptual physical model that partly explains the results of our observational study.

Figure 5.7a displays the stress field heterogeneity and the rotations of the maximum compressive stress axis σ_1 (black lines) that are highest around the highest slip patches on the fault plane of the 1992 Landers earthquake. Rotations of the

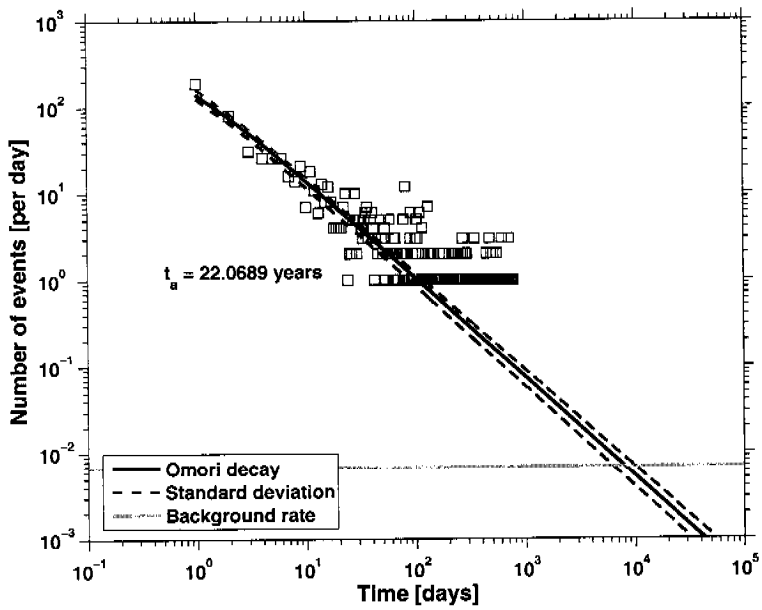

Figure 5.15: Aftershock duration of the 1983 Coalinga event. Considering the uncertainties in the modified Omori law parameters, t_a varies between 17.18 and 27.20 years.

maximum compressive stress axis have been documented by *Hauksson* (1992) and *Hardebeck and Hauksson* (2001b) for the Landers main shock which is also reflected in our results (Figure 5.16a). Similarly, rotations for the Coalinga event were presented by *Michael* (1987b) rotating back with time to the orientation prior to the event. The stress field heterogeneity in map view is also revealed by cross-sectional mapping along the ruptured segments of the Landers earthquake which facilitates the correlation with the main-shock slip distribution (Figure 5.8). Our conceptual model is based on modeling the stress rotations resulting from stress transfer based on a Coulomb model (*Stein et al.*, 1992). We calculated coseismic rotations of the principal stress axes in an elastic half space under the assumption of a uniaxial N7°E compression with varying regional stress levels. Qualitatively, we obtain good agreement between the stress tensor axis rotations and the modeled rotations when assuming a 30-50 bar uniform regional stress field (Figure 5.16b).

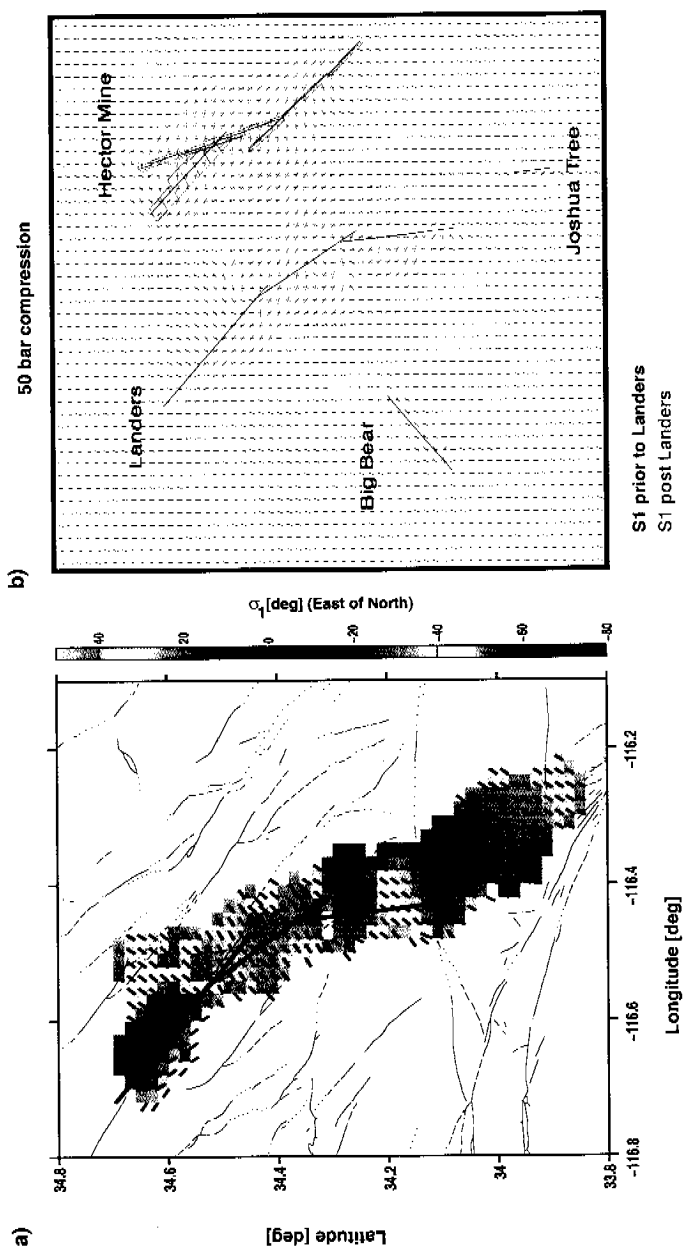

Figure 5.16: Conceptual model for rotations of stress axes following strong earthquakes: a) Trend of σ_1 from stress tensor inversion as background colorscale superimposed with σ_1 trend lines (black). b) Orientation of σ_1 prior (blue, N7°E) and post (red) the Landers main shock on optimally oriented planes at a depth of 8 km. Rotations of σ_1 are calculated assuming a 50 bar uniaxial background stress field ($mathrmN7°$E) and using the slip distribution of *Wald and Heaton* (1994).

The agreement vanishes when using lower stress levels (around 10 bar) of the regional stress field which produces rotations in much larger regions and further away from the fault. Higher stress levels ($\geq$ 80 bar) result in very small to no rotations of the σ_1 stress axis. These results support the HPSSF-hypothesis assuming that the regional stress field is on the order of 30-50 bar. In this case, the Landers earthquake would locally cause a complete stress drop, triggering a diverse set of aftershocks and resulting in a temporary heterogeneous stress field.

The conceptual model not only bears the potential of modeling the stress rotations following a main shock, but may also be used to estimate the absolute state of stress in the Earths' crust in a quantitative study. In addition, including stress loading mechanisms in the conceptual model with, e. g., a tectonic loading, viscoelastic relaxation (e. g., *Freed and Lin*, 2001), or fluid flow (*Nur and Booker*, 1972; *Hickman et al.*, 1995, and references therein), might also lead to a better understanding of the stress field prior to the occurrence of a strong earthquakes.

In terms of earthquake prediction, our conceptual model contradicts the reasoning that earthquakes cannot be predicted (*Geller et al.*, 1997) or occur at random (*Kagan*, 1997). We find evidence that the stress drop locally on the fault plane is a substantial fraction of the total regional background stress field, supporting the HPSSF-hypothesis in agreement with the arguments of *Wyss and Wiemer* (1999). Moreover, the conceptual model based on Coulomb stress transfer shows preliminary evidence that large earthquakes along faults are likely to release almost the total traction of the system.

Wiemer et al. (2002) speculated that the high b-values coincide in some cases with areas of increased stress-field heterogeneity or large stress-drops. A simple linear relationship between β and b is only found for the Landers earthquake in which high b-values correlate with high stress-field heterogeneity. This relation is

not found for other events. It is further problematic since the regions of highest values coincide with a complex fault structure, thus either the complexity of the fault zone or other physical mechanisms could have similar influence. We are not able to resolve conclusively if this observation is a consequence of the fault zone or fault network complexity or based on the contribution of normal faulting events. The latter would clearly link this phenomena to the faulting styles as suggested by *Schorlemmer et al.* (2005b).

We observe the phenomena of a decaying stress anomaly for all the sequences we have analyzed. The time periods are much smaller compared to the aftershock sequence durations. Remarkably, the stress field heterogeneity decreases fast at first and then slows down which is also seen for the rotation of the σ_1 axis (*Michael*, 1987b), who also argues that the return to previous state of stress due to elastic rebound may have been finished already 2 years after the Coalinga event which is roughly in agreement with the time span found for β. The temporal stress anomaly and the decay with time was already suggested by *Benioff* (1951) and attributed to elastic creep. The time scales to recover the stress field and to return to the seismicity rate before the main shock are largely different and for most events the elapsed time since the main shock is not long enough.

Spatial mapping of seismicity parameters is applied in time-dependent hazard assessment where it is a critical input (*Gerstenberger et al.*, 2005). Our analysis, based on well located aftershocks, confirms earlier analyzes that found similar values and patterns of b- and p-values for the events investigated. It also shows that improved hypocenter locations reveal the patterns more distinctly, which is certainly important when providing aftershock forecasts with a depth dependent component. Therefore, we emphasize that fast, automated and reliable hypocenter locations accompanied with subsequent spatial mapping of aftershock properties can improve

near-real time aftershock forecasting.

We transformed the detailed mapping of modified Omori law parameters to map aftershock sequence durations along the strike of faults. The cross-sectional mapping reveals strong lateral heterogeneities in t_a. The pattern of low p-values and long aftershock sequence durations coincide; however, the areas of long t_a do not match the areas of highest heterogeneity. We are not able to provide a causal physical link for this observation. The persistence of longer durations in regions of lower heterogeneity might be related to the activation of seismicity on favorably oriented faults. This is in contrast to regions where diverse faulting styles where activated shortly after the main shock, returning relatively fast to the background seismicity when the stress field recovers.

The mapping of aftershock sequence duration suffers from small data sets before the main shocks forcing us to use background rates averaged over the entire fault. Ideally, we would map the background rates in the same volumes. Thus, the absolute numbers might be taken as rules of thumb. As a possible continuation of this study, we anticipate to compare the spatial mapping of aftershock duration with a model based on rate and state friction and the shear-stress change computed on the causative fault planes. *Dieterich* (1994) provides a theoretical basis for this approach which bears the potential for new physically based time-dependent forecast models.

5.6 Acknowledgments

We thank P. M. Mai, E. Hauksson, G. Hiller, D. Schorlemmer and J. Ripperger for critical reviews and stimulating discussions. We thank the Southern California Earthquake Data Center (SCEDC) for providing the catalog of the Southern California Seismic Network (SCSN) and the Northern California Seismic Network (NCSN,

U.S. Geological Survey, Menlo Park) for providing the Northern California Earthquake Catalog together with the Berkeley Seismological Laboratory, University of California, Berkeley.

Chapter 6

Conclusions

The principal objectives of the thesis were (1) to better understand the spatial and temporal occurrence of clustered seismicity in the near-source region of seismogenic faults, (2) to improve links to the underlying physics of earthquakes, and (3) to analyze implications for seismic hazard assessment. I approached these goals by developing new statistical methods for seismicity analysis in general and for aftershock sequences in particular. These methods are essential to perform detailed analyzes of observable and derived parameters and their uncertainties. The parameters of interest are the magnitude of completeness M_c (Chapter 2), the b-value from the Gutenberg-Richter law (Chapter 2 and 5), the exponent p in the modified Omori law (Chapter 3 and 5), the location and location uncertainty of aftershock hypocenters, the slip and stress drop distribution of earthquakes (Chapter 4), the orientation of the stress tensor axis σ_1, and the angular misfit β as a measure of stress field heterogeneity (Chapter 5). I have demonstrated that the spatial and temporal evolution of the properties of aftershock sequences are related to the slip and stress changes in the near-field of rupture planes, as reflected in heterogeneities of the seismicity parameters on all scales resolvable.

6.1 Summary of results

I have developed a method to determine the magnitude of completeness M_c which uses the entire observed magnitude range of earthquakes (EMR-method) (Chapter 2). The EMR-method is superior to other methods because it is based on a refined likelihood based procedure, provides a comprehensive model for the entire frequency-magnitude range and is testable against the original distribution with standard statistical tests, e. g., a Kolmogorov-Smirnov test. I have introduced a bootstrap approach that can be combined with each method to determine M_c. It is now possible to simultaneously estimate reliable uncertainties of M_c and b for the quality assessment of earthquake catalogs in an automated fashion. Tests with synthetic catalogs showed that the EMR-method performed superior in reproducing previously defined completeness levels than other existing methods. The application to various regional and global catalogs, several aftershock sequences and the comparison with other methods showed that the EMR-method, although computationally more demanding, proved to be more robust for automated mapping purposes (Chapter 2). However, for specific earthquake catalogs, the seismicity model as defined in the EMR-method may not provide the best fit due to procedures of the network operators or the tectonic regime. Consequently, other functions can be adapted in the algorithm to model the observed seismicity.

Thoroughly investigated earthquake catalogs are essential and critical when addressing the fine-scale structure of aftershock sequence properties. The techniques developed for the quality assessment provided an indispensible basis to investigate rate changes in clustered seismicity. I have formulated a procedure to determine the statistical significance of relative rate changes within aftershock sequences (Chapter 3). This procedure subsequently combines (1) a grid-search based approximate maximum likelihood estimate of the single and nested Omori law parameters, (2) an estimate of uncertainties by a bootstrap approach, (3) the determination of the best

fitting model according to the Akaike Information Criterion, and (4) a verification of the best fitting model with a two-sample Kolmogorov-Smirnov goodness-of-fit test. The approach is designed to map relative rate changes in clustered seismicity in contrary to rate change algorithms that are limited to be used for declustered catalogs (z- and β-statistic, *Wiemer and Wyss*, 1994; *Reasenberg and Matthews*, 1988). I performed a high resolution study for an earthquake doublet in the Kagoshima province (Japan) and showed that the second main shock ($M_W = 6.0$) strongly influenced the on- and off-fault aftershock activity of the first main shock ($M_W = 6.1$). The results are qualitatively in good agreement with the Coulomb stress change pattern of *Toda and Stein* (2003) away from and near the rupture plane. These results suggest that aftershocks can be understood as stress meters (*Schorlemmer et al.*, 2005b) and that changes in the state of stress in their immediate vicinity are reflected in their rate of occurrence (*Woessner et al.*, 2004a). This is consistent with a rate and state friction model to infer stress changes from earthquake rate changes (*Dieterich et al.*, 2000).

The spatio-temporal mapping approach of seismicity parameters to determine the significance of relative rate changes is currently limited to aftershock sequences and only employs the modified and nested modified Omori laws including one secondary aftershock sequence. Although this has been proven to adequately fit observed data for large fractions of fault zones, it is desirable to integrate more complex models like the Epidemic Type Aftershock model (ETAS) based on the idea that each earthquake can trigger its own aftershocks. The integration of more complex models could lead to better fit for example swarm like activity (*Ogata*, 1999; *Hainzl and Ogata*, 2005).

The comparison between mapped Coulomb stress changes and relative rate changes was performed covering a region in and around the ruptured fault plane of the 1997 Kagoshima event up to a distance of about 20 km. This analysis is

comparable to many other studies in the last decade that focused on static and/or dynamic stress changes caused by main shocks (*Harris*, 1998; *Steacy et al.*, 2005, and references therein). Performing the correlation of aftershock hypocenter locations with on-fault main shock properties using high-quality data allowed me to scrutinize the relationship between main shocks and subsequent triggered seismicity in more detail on the ruptured faults. In Chapter 4, I developed non-standard statistical tests to quantify the spatial correlation of aftershock hypocenter locations and properties of finite-fault source models: the slip and stress-drop distribution. The results of the statistical tests confirm that aftershocks are preferentially located in low-slip regions with high statistical significance, given the uncertainty levels in the data sets. At a lower statistical significance level, aftershock hypocenters are correlated with the on-fault shear stress distribution. The correlations are improved when using relocated catalogs. In general, the results fit the expectations of the asperity model which predicts aftershocks to occur in response to stress transfer from an asperity to the surrounding regions (*Beroza and Zoback*, 1993). The approach is limited by epistemic and aleatory uncertainties in the finite-fault source models. I addressed these shortcomings by using different finite-fault source models and by simulating slip distributions with a random spatial field model which is likely to overestimate the uncertainties. Non-linear or dynamic effects that influence the stress transfer up to a few days in the first period of the aftershock sequence are not incorporated in the computation of shear-stress changes which further limits the information content of the results.

To obtain more observational constraints on the causal link between the heterogeneity of aftershock sequence properties and main shock induced stress changes, I inverted aftershock focal mechanisms for the best fitting stress tensor spatially and in time sequences (Chapter 5). I used cross-sections to compare the measure of stress field heterogeneity β with the slip, stress-drop, and b-value distribution with

high resolution. The investigation of cross-sections is used to question the suggestions of the heterogeneous post-seismic stress field hypothesis and confirmed (1) that the largest heterogeneities in the stress field are in general concentrated in areas of highest coseismic slip and (2) that the stress field heterogeneity β decreases with time.

I provided a conceptual model based on Coulomb stress transfer, assuming a background stress field on the order of 30-50 bars that qualitatively matches the rotations of the maximum compressive stress axis obtained from the stress tensor inversion. The results support arguments that large earthquakes occurring on the San Andreas fault system and in the eastern California shear zone release most of the shear stress on the ruptured fault plane implying almost complete stress drop events. In combination with the rotation of the maximum stress tensor axis and the post-seismic stress field heterogeneity, this further indicates that the San Andreas fault and faults in the eastern California shear zone are weak. Comparing time series of the stress tensor heterogeneity $\beta(t)$ with the duration of aftershock sequences suggest that these processes occur on different time scales, with the recovery of the stress field being much shorter than the durations of aftershock sequences.

6.2 Future perspectives

Combinations of the various methods presented in my thesis provide, despite their limitations, multifold opportunities to address topics in statistical seismology, e. g., the relation of aftershock sequence properties to earthquake physics and the improvement of time-dependent seismic hazard assessment.

Assessing the quality of parametric earthquake catalogs and determining the magnitude of completeness with its uncertainty is one of the most essential steps in this respect since the b-value of the earthquake size distribution strongly depends

on this parameter. Similarly, the parameters describing the temporal decay of aftershock sequences depend on the completeness level. As the time-dependent component of seismic hazard assessment becomes increasingly important and widely applied in earthquakes short- and long-term seismicity forecasts (e. g. , *Rundle et al.*, 2002; *Keilis-Borok et al.*, 2004; *Gerstenberger et al.*, 2005), the quality control of the incoming data also becomes increasingly important. In collaboration with the operators of the Southern California Seismic Network (SCSN), I started to create a database of yearly and long-term completeness level maps which might become a further resource of information available online for the scientific community. Figure 6.1 shows an example of the spatial and temporal variability of M_c computed for the Advanced National Seismic System catalog (ANSS). In essence, a common data base may facilitate processes like community efforts for comparative earthquake forecast model tests (*Schorlemmer and Gerstenberger*, 2005, `www.relm.org`).

Statistical tests comparing aftershock hypocenter locations with complex slip and shear-stress distributions derived from finite-fault source models have shown significant correlations for vertical strike-slip events. These results support the expectations of the asperity model in which the shear stress is transfered from the ruptured asperity to the surrounding regions. Applying and enhancing the non-standard spatial statistical tests to other parameters derived in earthquake source seismology is straightforward and a feasible future task. I am optimistic that this research leads to further insight in the source process of earthquakes, to quantitative validation procedures for theoretical models, and helps to constrain numerical models which simulate earthquake cycles including aftershock sequences (*Hillers et al.*, 2005; *Hillers and Miller*, 2005; *Zöller et al.*, 2005).

I have estimated the duration of aftershock sequences from the detailed depth-dependent cross-sectional mapping of the modified Omori law parameters which

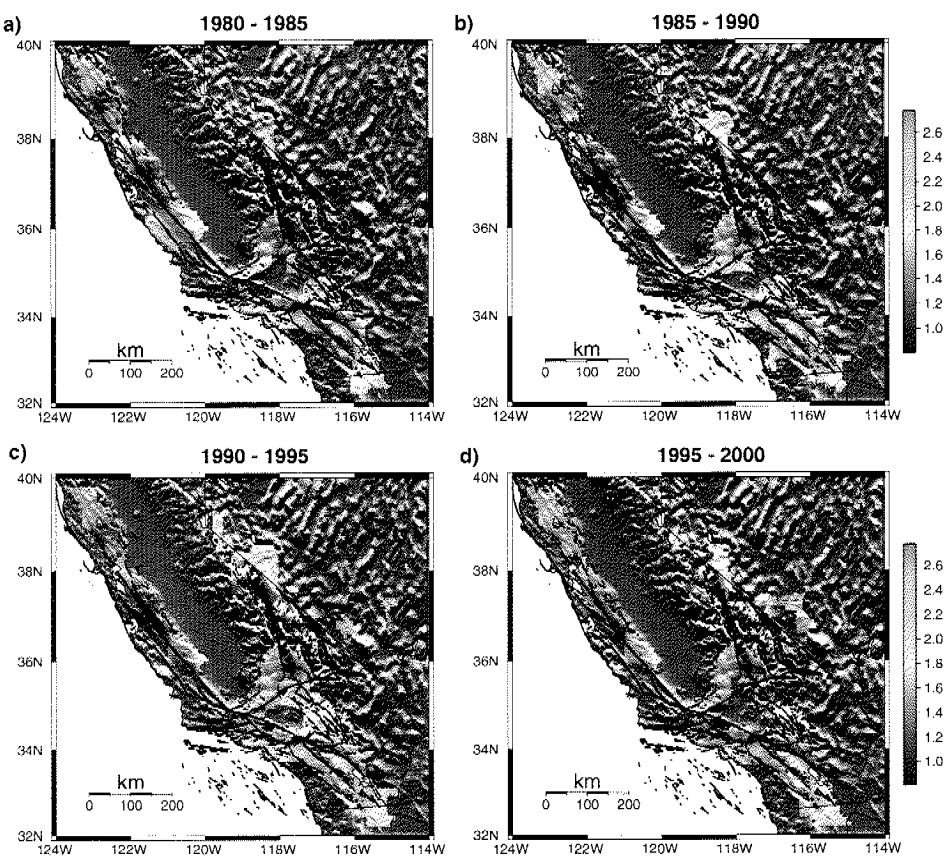

Figure 6.1: M_c maps for crustal seismicity of the ANSS catalog for 5 years periods from 1980-2000 ($r = 30\,\mathrm{km}$, $d \leq 30\,\mathrm{km}$, grid $0.1^\circ \times 0.1^\circ$deg).

reveals strong heterogeneities along strike and depth. A model that forecasts the aftershock durations and compares it to the observational results has not been implemented yet. However, *Dieterich* (1994) provides a theoretical basis using the rate and state friction model that can be used together with the detailed shear-stress distribution on a fault plane from a large earthquake. Based on this idea, I envision to develop a forecast model that might enhance existing time-dependent hazard assessment by supplying additional physical constraints.

The conceptual model based on Coulomb stress transfer provides possibilities to obtain insights in the state of stress of the Earth's crust and the mechanics of earthquake faulting. A quantitative analysis of the correlation between rotations of the principal stress axis from the Coulomb stress transfer model and the observed rotations from the stress tensor inversion may allow a better estimate of the absolute stress level in the crust (see Figure 5.16), which is an unresolved issue in the ongoing debate on earthquake prediction models (*Wyss and Wiemer*, 1999). This might additionally help to confirm the HPSSF-hypothesis which is based on the idea of almost complete stress drop earthquakes. Using different loading processes, e. g., tectonic loading, viscoelastic relaxation (*Freed and Lin*, 2001), or fluid flow (*Nur and Booker*, 1972; *Hickman et al.*, 1995, and references therein), the conceptual model potentially helps explaining the recovery of the stress field and the decrease of its heterogeneity with time.

Bibliography

Abercrombie, R. E., and J. N. Brune (1994), Evidence for a constant b-value above magnitude 0 in the southern San Andreas, San Jacinto and San Miguel fault zones, and at the Long Valley caldera, California, *Geophys. Res. Let.*, *21*, 1647–1650.

Aki, K. (1965), Maximum likelihood estimate of b in the formula $\log n = a - bm$ and its confidence limits, *Bull. Earthquake Re. Inst., Tokyo Univ.*, *43*, 237–239.

Aki, K. (1967), Scaling law of seismic spectrum, *J. Geophy. Res.*, *72*, 1217–1231.

Aki, K. (1979), Characterization of barriers on an earthquake fault, *J. Geophy. Res.*, *84*, 6140–6148.

Aki, K. (1984), Asperities, barriers, characteristic earthquakes and strong motion prediction, *J. Geophy. Res.*, *89*(B7), 5867–5872.

Albarello, D., R. Camassi, and A. Rebez (2001), Detection of space and time heterogeneity in the completeness of a seismic catalog by a statistical approach: An application to the Italian area, *Bull. Seism. Soc. Am.*, *91*(6), 1694–1703.

Amelung, F., and G. King (1997), The difference between earthquake scaling laws for creeping and non-creeping faults, *Geophys. Res. Let.*, *24*, 507–510.

Amitrano, D. (2003), Brittle-ductile transition and associated seismicity: Experimental and numerical studies and relationship with the b-value, *J. Geophy. Res.*, *108*(B1), ESE 19–1, doi:10.1029/2001JB000680.

Bakun, W. H., and A. G. Lindh (1984), The Parkfield California earthquake prediction experiment, *Science*, *229*, 619–624.

Bender, B. (1983), Maximum likelihood estimation of b-values for magnitude grouped data, *Bull. Seism. Soc. Am.*, *73*(3), 831–851.

Benioff, H. (1951), Earthquakes and rock creep, part I, Creep characteristics of rocks and the origin of aftershocks, *Bull. Seism. Soc. Am.*, *41*(62), 31–62.

Seite Leer /
Blank leaf

Beresnev, I. A. (2003), Uncertainties in finite-fault slip inversions: To what extent to believe?, *Bull. Seism. Soc. Am.*, *93*(6), 2445–2458.

Beroza, G. (1991), Near-source modeling of the Loma Prieta earthquake: Evidence for heterogeneous slip and implications for earthquake hazard, *Bull. Seism. Soc. Am.*, *81*(5), 1603–1621.

Beroza, G., and P. Spudich (1988), Linearized inversion for fault rupture behavior: Application to the 1984 Morgan Hill, California, earthquake, *J. Geophy. Res.*, *93*(B6), 6275–6296.

Beroza, G. C., and M. D. Zoback (1993), Mechanism diversity at Loma Prieta aftershocks and the mechanics of mainshock-aftershock interaction, *Science*, *259*, 210–213.

Berz, G. (2000), topics 2000 Naturkatastrophen - Stand der Dinge, Publikationsreihe der Müncher Rückversicherungs Gesellschaft, Sonderheft Millenium.

Bosl, W. J., and A. Nur (2002), Aftershocks and pore fluid diffusion following the 1992 Landers earthquake, *J. Geophy. Res.*, *107*(B12), 2366, doi:10.1029/2001JB000155.

Cao, A. M., and S. S. Gao (2002), Temporal variation of seismic b-values beneath northeastern Japan island arc, *Geophys. Res. Let.*, *29*(9), doi:10.1029/2001GL013775.

Chernick, M. R. (1999), *Bootstrap methods: A practitioner's guide*, Wiley series in probability and statistics, John Wiley & Sons Inc., New York.

Conover, W. J. (1999), *Practical nonparametric statistics*, Wiley series in probability and statistics: Applied probability and statistics section, 3rd ed., John Wiley & Sons, Inc., New York.

Dalguer, L. A., K. Irikura, and W. Zhang (2002), Distribution of dynamic and static stress changes during 2000 Tottori (Japan) earthquake: Brief interpretation of earthquake sequences; foreshocks, mainshock and aftershocks, *Geophys. Res. Let.*, *29*(16), 1762, doi:10.1029/2002GL014333.

Das, S., and K. Aki (1977), Fault planes with barriers; a versatile earthquake model, *J. Geophy. Res.*, *82*, 5658–5670.

Das, S., and C. Henry (2003), Spatial relationship between main earthquake slip and its aftershock distribution, *Rev. Geophys.*, *41*(3), doi:10.1029/2002RG000119.

Deichmann, N., et al. (2002), Earthquakes in Switzerland and surrounding regions during 2001, *Eclogae Geologicae Helvetiae*, *95*, 249–262.

Dieterich, J. H. (1994), A constitutive law for rate of earthquake production and its application to earthquake clustering, *J. Geophy. Res.*, *99*(B2), 2601–2618.

Dieterich, J. H., V. Cayol, and P. Okubo (2000), The use of earthquake rate changes as a stress meter at kilauea volcano, *Nature*, *408*(6811), 457–460.

Dietz, L. D., and W. L. Ellsworth (1990), The October 17, 1989, Loma Prieta, California, earthquake and its aftershocks: Geometry of the sequence from high-resolution locations, *Geophys. Res. Let.*, *17*(9), 1417–1420, doi:10.1029/90GL01000.

Dreger, D. S., L. Gee, P. Lombard, M. H. Murray, and B. Romanowicz (2005), Rapid finite-source analysis and near-fault strong motions: Application to the 2003 M_W 6.5 San Simeon and the 2004 M_W 6.0 Parkfield earthquakes, *Seism. Res. Let.*, *76*(1).

Dziewonski, A. M., G. Ekström, and N. N. Maternovskaya (1999), Centroid-moment tensor solutions for October-December, 1998, *Phys. Earth Planet. Inter.*, *115*(1-2), 1–16.

Eberhart-Phillips, D., and A. J. Michael (1998), Seismotectonics of the Loma Prieta, California, region determined from three-dimensional v_p, v_p/v_s, and seismicity, *J. Geophy. Res.*, *103*(B9), 21,099?21,120.

Efron, B. (1979), 1977 Rietz Lecture - Bootstrap Methods - Another look at the jackknife, *Annals of Statistics*, pp. 1–26.

Enescu, B., and K. Ito (2002), Spatial analysis of the frequency-magnitude distribution and decay rate of aftershock activity of the 2000 Western Tottori earthquake, *Earth, Planets and Space*, *54*, 847–859.

Faeh, D., et al. (2003), Earthquake catalog of Switzerland (ECOS) and the related macroseismic database, *Eclogae Geologicae Helvetiae*, *96*(2), 219–236.

Felzer, K. R., and E. E. Brodsky (2005), Testing the stress shadow hypothesis, *J. Geophy. Res.*, *110*, B05S09, doi:10.1029/2004JB003277.

Felzer, K. R., R. E. Abercrombie, and G. Ekström (2003), Secondary aftershocks and their importance for aftershock prediction, *Bull. Seism. Soc. Am.*, *93*(4), 1433–1448.

Freed, A. M., and J. Lin (2001), Delayed triggering of the 1999 Hector Mine earthquake by viscoelastic stress transfer, *Nature*, *411*, 180–183, doi:0.1038/35075548.

Frohlich, C., and S. D. Davis (1993), Teleseismic b values; or, much ado about 1.0, *J. Geophy. Res.*, *98*, 631–644.

Fukuyama, E., W. L. Ellsworth, F. Waldhauser, and A. Kubo (2003), Detailed fault structure of the 2000 Western Tottori, Japan, earthquake sequence, *Bull. Seism. Soc. Am.*, *93*(4), 1468–1478.

Gardner, J. K., and L. Knopoff (1974), Is the sequence of earthquakes in southern California, with aftershocks removed, poissonian?, *Bull. Seism. Soc. Am.*, *64*, 1363–1367.

Geller, R. J., D. D. Jackson, Y. Y. Kagan, and F. Mulargia (1997), Earthquakes cannot be predicted, *Science*, *275*, 1616–1617.

Gephart, J. W., and D. W. Forsyth (1984), An Improved Method for Determining the Regional Stress Tensor Using Earthquake Focal Mechanism Data: Application to the San Fernando Earthquake Sequence, *J. Geophy. Res.*, *89*(B11), 9305–9320.

Gerstenberger, M. C. (2004), Earthquake clustering and time-dependent probabilistic seismic hazard analysis for California, Ph.D. thesis, ETH Zurich, no. 15215.

Gerstenberger, M. C., S. Wiemer, and D. Giardini (2001), A systematic test of the hypothesis that the *b*-value varies with depth in California, *Geophys. Res. Let.*, *28*(1), 57–60.

Gerstenberger, M. C., S. Wiemer, L. M. Jones, and P. A. Reasenberg (2005), Real-time forecasts of tomorrow's earthquakes in California, *Nature*, *435*(7040), 328–331, doi:10.1038/03622.

Gomberg, J. (1991), Seismicity and detection/location threshold in the southern great basin seismic network, *J. Geophy. Res.*, *96*(16), 401–16,414.

Gomberg, J., P. Reasenberg, P. Bodin., and R. Harris (2001), Earthquake triggering by seismic waves following the Landers and Hector Mine earthquakes, *Nature*, *411*(6836), 462–466.

Gross, S., and C. Kisslinger (1997), Estimating tectonic stress rates and state with Landers aftershocks, *J. Geophy. Res.*, *102*(B4), 7603–7612.

Gutenberg, B., and C. F. Richter (1944), Frequency of earthquakes in California, *Bull. Seism. Soc. Am.*, *34*, 185–188.

Habermann, R. E. (1987), Man-made changes of seismicity rates, *Bull. Seism. Soc. Am.*, *77*, 141–159.

Habermann, R. E. (1991), Seismicity rate variations and systematic changes in magnitudes in teleseismic catalogs, *Tectonophysics*, *193*, 277–289.

Habermann, R. E., and F. Creamer (1994), Catalog errors and the M8 earthquake prediction algorithm, *Bull. Seism. Soc. Am.*, *84*, 1551–1559.

Hainzl, S., and Y. Ogata (2005), Detecting fluid signals in seismicity data through statistical earthquake modeling, *J. Geophy. Res.*, *110*, B05S07, doi:10.1029/2004JB003247.

Hardebeck, J. L., and E. Hauksson (1999), Role of fluids in faulting inferred from stress field signatures, *Science*, *285*, 236–239.

Hardebeck, J. L., and E. Hauksson (2001a), Stress orientations obtained from earthquake focal mechanisms: What are appropriate uncertainty estimates, *Bull. Seism. Soc. Am.*, *91*, 250–262.

Hardebeck, J. L., and E. Hauksson (2001b), Crustal stress field in southern California and its implications for fault mechanisms, *J. Geophy. Res.*, *106*(B10), 21,859–21,882.

Hardebeck, J. L., and A. J. Michael (2004), Stress orientations at intermediate angles to the San Andreas Fault, California, *J. Geophy. Res.*, *109*, b11303, doi:10.1029/2004JB003239.

Hardebeck, J. L., and P. M. Shearer (2002), A new method for determining first-motion focal mechanisms, *Bull. Seism. Soc. Am.*, *92*(6), 2264–2276.

Harris, R. A. (1998), Introduction to special section: Stress triggers, stress shadows, and implications for seismic hazard, *J. Geophy. Res.*, *103*(B10), 24,347–24,358.

Harris, R. A., and R. W. Simpson (2002), The 1999 M_W 7.1 Hector Mine, California, earthquake: A test of the stress shadow hypothesis?, *Bull. Seism. Soc. Am.*, *92*(4), 1497–1512.

Hartzell, S., G. S. Stewart, and C. Mendoza (1991), Comparison of L_1 and L_2 norms in a teleseismic inversion for the slip history of the Loma Prieta, California earthquake, *Bull. Seism. Soc. Am.*, *81*(5), 305–331.

Hartzell, S. H., and T. H. Heaton (1986), Rupture history of the 1984 Morgan Hill, California, earthquake from the inversion of strong motion records, *Bull. Seism. Soc. Am.*, *76*(3), 649–674.

Haskell, N. A. (1966), Total energy and enery spectral density of elastic wave radiation from popagating faults, Part II, A statistical source model, *Bull. Seism. Soc. Am.*, *56*, 125–140.

Hauksson, E. (1992), State of Stress from Focal Mechanisms Before and After the 1992 Landers Earthquake Sequence, *Bull. Seism. Soc. Am.*, *84*(3), 917–934.

Hauksson, E. (2000), Crustal structure and seismicity distribution adjacent to the Pacific and North America plate boundary in southern California, *J. Geophy. Res.*, *105*(B6), 13,875–13,903.

Hauksson, E. (2002), The 1999 M_W 7.1 Hector Mine, California, earthquake sequence: Complex conjugate strike-slip faulting, *Bull. Seism. Soc. Am.*, *92*(4), 1154–1170.

Hauksson, E., and P. Shearer (2005), Southern California Hypocenter Relocation with Waveform Cross-Correlation, Part 1: Results Using the Double-Difference Method, *Bull. Seism. Soc. Am.*, *95*(3), 896–903, doi:10.1785/0120040167.

Helmstetter, A., and D. Sornette (2002), Subcritical and supercritical regimes in epidemic models of earthquake aftershocks, *J. Geophy. Res.*, doi:10.1029/2001JB001580.

Helmstetter, A., G. Ouillon, and D. Sornette (2003), Are aftershocks of large Californian earthquakes diffusing?, *J. Geophy. Res.*, *108*(B10), 2483, doi:10.1029/2003JB002503.

Helmstetter, A., Y. Y. Kagan, and D. D. Jackson (2005), Importance of small earthquakes for stress transfer and earthquake triggering, *J. Geophy. Res.*, *110*, B05S08, doi:10.1029/2004JB003286.

Hernandez, B., F. Cotton, and M. Campillo (1999), Contribution of radar interferometry to a two-step inversion of the kinematic process of the 1992 Landers earthquake, *J. Geophy. Res.*, *104*(B6), 13,083–13,099.

Hickman, S., R. Sibson, and R. Bruhn (1995), Introduction to special section: Mechanical involvement of fluids in faulting, *J. Geophy. Res.*, *100*(B7), 12,831–12,840.

Hickman, S., M. Zoback, and W. Ellsworth (2004), Introduction to special section: Preparing for the San Andreas Fault Observatory at Depth, *Geophys. Res. Let.*, L12S01, doi:10.1029/2004GL020688.

Hillers, G., and S. A. Miller (2005), Stability regimes of a dilatant, fluid infiltrated fault plane in a 3-D elastic solid, *J. Geophy. Res.*, submitted.

Hillers, G., Y. Ben-Zion, and P. M. Mai (2005), Seismicity on a fault with rate- and state dependent friction and spatial variations of the critical slip distance, *J. Geophy. Res.*, submitted.

Horikawa, H. (2001), Earthquake doublet in Kagoshima, Japan: Rupture of asperities in a stress shadow, *Bull. Seism. Soc. Am.*, *91*(1), 112–127.

Hudnut, K. W., et al. (1994), Co-seismic displacements of the 1992 Landers earthquake sequence, *Bull. Seism. Soc. Am.*, *84*, 625–645.

Ide, S., and G. C. Beroza (2001), Does apparent stress vary with earthquake size?, *Geophys. Res. Let.*, *28*(17), 3349–3352.

Ishimoto, M., and K. Iida (1939), Observations of earthquakes registered with the microseismograph constructed recently, *Bull. Earthq. Res. Inst.*, *17*,, 443–478.

Ji, C., D. J. Wald, and D. V. Helmberger (2002a), Source description of the 1999 Hector Mine, California, earthquake, Part I: Wavelet domain inversion theory and resolution, *Bull. Seism. Soc. Am.*, *92*(4), 1192–1207.

Ji, C., D. J. Wald, and D. V. Helmberger (2002b), Source description of the 1999 Hector Mine, California, earthquake, Part II: Complexity of slip history, *Bull. Seism. Soc. Am.*, *92*(4), 1208–1226.

Ji, C., K. K. Choi, N. King, and K. W. Hudnut (2004), Co-seismic slip history and early afterslip of the 2004 Parkfield earthquake, *Eos Trans. AGU*, *85*(47), fall Meet. Suppl., Abstract S53D-04.

Jónsson, S., H. Zebker, P. Segall, and F. Amelung (2002), Fault slip distribution of the $M_W = 7.1$ Hector Mine, California, earthquake, estimated from satellite radar and GPS measurements, *Bull. Seism. Soc. Am.*, *92*(4), 1377–1389.

Kagan, Y. Y. (1997), Are earthquakes predictable?, *Geophys. J. Int.*, *131*, 505–525.

Kagan, Y. Y. (1999), Universality of the seismic moment-frequency relation, *Pure appl. geophys.*, *155*, 537–573.

Kagan, Y. Y. (2002), Seismic moment distribution revisited: I. Statistical results, *Geophys. J. Int.*, *148*, 520–541.

Kagan, Y. Y. (2003), Accuracy of modern global earthquake catalogs, *Phys. Earth Planet. Inter.*, *135*(2-3), 173–209.

Kagan, Y. Y., and D. D. Jackson (1998), Spatial aftershock distribution: Effect of normal stress, *J. Geophy. Res.*, *103*(B10), 24,453–24,467.

Kaverina, A., D. Dreger, and E. Price (2002), The combined inversion of seismic and geodetic data for the source process of the 16 October 1999 $M_W = 7.1$ Hector Mine, California, earthquake, *Bull. Seism. Soc. Am.*, *92*(4), 1266–1280.

Keilis-Borok, V., P. Shebalin, A. Gabrielov, and D. Turcotte (2004), Reverse tracing of short-term earthquake precursors, *145*, 75–85.

Kenneth, P., K. Burnham, and D. R. Anderson (2002), *Model selection and multimodel inference: A practical information - theoretical approach*, 2nd ed., Springer.

Kilb, D., M. Ellis, J. Gomberg, and S. Davis (1997), On the origin of diverse aftershock mechanisms following the 1989 Loma Prieta earthquake, *Geophys. J. Int.*, *128*, 557–570.

King, G. C. P., R. S. Stein, and J. Lin (1994), Static stress changes and the triggering of earthquakes, *Bull. Seism. Soc. Am.*, *84*(1), 935–953.

Knopoff, L. (2000), The magnitude distribution of declustered earthquakes in southern California, in *Proceedings of the National Academy of Sciences of the United States of America*, pp. 11,880–11,884.

Kvaerna, T., F. Ringdal, J. Schweitzer, and L. Taylor (2002a), Optimized seismic threshold monitoring - part 1: Regional processing, *Pure appl. geophys.*, *159*(5), 969–987.

Kvaerna, T., F. Ringdal, J. Schweitzer, and L. Taylor (2002b), Optimized seismic threshold monitoring - part 2: Teleseismic processing, *Pure appl. geophys.*, *159*(5), 989–1004.

Lachenbruch, A. H., and J. H. Sass (1992), Heat flow from the Cajon Pass, fault strength, and tectonic implications, *J. Geophy. Res.*, *97*, 4995–5015.

Liu, J., K. Sieh, and E. Hauksson (2003), A structural interpretation of the aftershock "cloud" of the 1992 M_W7.3 Landers earthquake, *Bull. Seism. Soc. Am.*, *93*(3), 1333–1344.

Mai, P. M. (2004), SRCMOD: a database of finite-fault source models, `http://www.seismo.ethz.ch/srcmod`.

Mai, P. M., and G. C. Beroza (2000), Source scaling properties from finite-fault-rupture models, *Bull. Seism. Soc. Am.*, *90*(3), 604–615.

Mai, P. M., and G. C. Beroza (2002), A spatial random field model to characterize complexity in earthquake slip, *J. Geophy. Res.*, *107*(B11), doi:10.1029/201JB000588.

Mai, P. M., P. Spudich, and J. Boatwright (2005), Hypocenter locations in finite-source rupture models, *Bull. Seism. Soc. Am.*, *95*(3), 965–980.

Main, I. (2000), Apparent breaks in scaling in the earthquake cumulative frequency-magnitude distribution: fact or artifact?, *Bull. Seism. Soc. Am.*, *90*(1), 86–97.

Marsan, D. (2003), Triggering of seismicity at short timescales following Californian earthquakes, *J. Geophy. Res.*, *108*(B5), 2266, doi:10.1029/2002JB001946.

Mendoza, C., and S. H. Hartzell (1988), Aftershock properties and main shock faulting, *Bull. Seism. Soc. Am.*, *78*(4), 1438–1449.

Michael, A. J. (1984), Determination Of Stress From Slip Data: Faults And Folds, *J. Geophy. Res.*, *89*(B13), 11,517–11,526.

Michael, A. J. (1987a), Use of Focal Mechanisms to Determine Stress, *J. Geophy. Res.*, *92*(B1), 357–368.

Michael, A. J. (1987b), Stress Rotation During the Coalinga Aftershock Sequence, *J. Geophy. Res.*, *92*(B8), 7963–7979.

Michael, A. J. (1991), Spatial Variations in Stress Within the 1987 Whittier Narrows, California, Aftershock Sequence: New techniques and Results, *J. Geophy. Res.*, *96*(B4), 6303–6319.

Michael, A. J., W. L. Ellsworth, and D. H. Oppenheimer (1990), Coseismic stress changes induced by the 1989 Loma Prieta, California earthquake, *Geophys. Res. Let.*, *17*, 1441–1444.

Miller, S. A., C. Collettini, L. Chiaraluce, M. Cocco, M. Barchi, and J. P. Kaus (2004), Aftershocks driven by a high-pressure CO_2 source at depth, *Nature*, *427*, 724–727.

Miyamachi, H., H. Iwakiri, H. Yakiwara, K. Goto, and T. Kakuta (1999), Fine structure of aftershock distribution of the 1997 Northwestern Kagoshima earthquakes with a three-dimensional velocity model, *Earth, Planets and Space*, *51*(4), 233–246.

Ni, S., H. Kanamori, and D. Helmberger (2005), Seismology energy radiation from the sumatra earthquake, *Nature*, *434*, 582, doi:10.1038/434582a.

Nur, A., and J. R. Booker (1972), Aftershocks caused by pore fluid flow?, *Science*, *175*, 885–887.

Ogata, Y. (1999), Seismicity analysis through point-process modeling: a review, *Pure appl. geophys.*, *155*, 471–507.

Ogata, Y. (2001), Increased probability of large earthquakes near aftershock regions with relative quiescence, *J. Geophy. Res.*, *106*(B5), 8729–8744.

Ogata, Y., and K. Katsura (1993), Analysis of temporal and spatial heterogeneity of magnitude frequency distribution inferred from earthquake catalogues, *Geophys. J. Int.*, *113*, 727–738.

Ogata, Y., L. M. Jones, and S. Toda (2003), When and where the aftershock activity was depressed: Contrasting decay patterns of the proximate large eathquakes in southern California, *J. Geophy. Res.*, *108*(B6), doi:10.1029/2002JB002009.

Okada, Y. (1992), Internal deformation due to shear and tensile faults in a half-space, *Bull. Seism. Soc. Am.*, *82*(2), 1018–1040.

Oppenheimer, D. H. (1990), Aftershock slip behavior of the 1989 Loma Prieta, California earthquake, *Geophys. Res. Let.*, *17*(8), 1199–1202, doi:10.1029/90GL01186.

Ouillon, G., and D. Sornette (2005), Magnitude-dependent omori law: Theory and empirical study, *J. Geophy. Res.*, *110*(B04306), doi:10.1029/2004JB003311.

Ratchkovski, N. A., S. Wiemer, and R. A. Hansen (2004), Seismotectonics of the Central Denali Fault, Alaska, and the 2002 Denali Fault Earthquake Sequence, *Bull. Seism. Soc. Am.*, *94*(6B), S156–S174.

Reasenberg, P., and D. Oppenheimer (1985), FPFIT, FPPLOT, and FPPAGE: FORTRAN computer programs for calculating and displaying earthquake fault-plane solutions, U.S. Geol. Surv. Open-File Rept. 85-739.

Reasenberg, P. A., and M. V. Matthews (1988), Precursory seismic quiescence: a preliminary assessment of the hypothesis, *Pure appl. geophys.*, *126*, 373–406.

Rice, J. R. (1992), Fault stress states, pore pressure distributions, and the weakness of the San Andreas fault, in *Fault mechanics and transport properties*, edited by B. Evans and T. F. Wong, pp. D73–D89, Academic.

Ripperger, J., and P. M. Mai (2004), Fast computation of static stress changes on 2D faults from final slip distributions, *Geophys. Res. Let.*, *31*, L18610, doi:10.1029/2004GL020594.

Rundle, J. B., K. F. Tiampo, W. Klein, and J. S. S. Martins (2002), Self-organization in leaky threshold systems: The influence of near-mean field dynamics and its implitcations for earthquakes, neuorbiology, and forecasting, *Proc. Nat. Acad. Sci. USA*, *99*, 2514–2521.

Rydelek, P. A., and I. S. Sacks (1989), Testing the completness of earthquake catalogues and the hypothesis of self-similarity, *Nature*, *337*, 251–253.

Rydelek, P. A., and I. S. Sacks (2003), Comment on "Minimum magnitude of completness in earthquake catalogs: Examples from Alaska, the Western United States, and Japan" by Stefan Wiemer and Max Wyss, *Bull. Seism. Soc. Am.*, *93*(4), 1862–1867.

Rymer, M. J., V. E. Landenheim, and E. Hauksson (2002), The Hector Mine, California, earthquake of 16 October 1999: Introduction to the special issue, *Bull. Seism. Soc. Am.*, *92*(4), 1147–1153.

Schaff, D. P., G. H. R. Bokelmann, G. C. Beroza, F. Waldhauser, and W. L. Ellsworth (2002), High-resolution image of the Calaveras fault seismicity, *J. Geophy. Res.*, *107*(B9), 2186, doi:10.1029/2001JB000633.

Scholz, C. H. (1968), The frequency-magnitude relation of microfacturing in rock and ist relation to earthquakes, *Bull. Seism. Soc. Am.*, *58*, 399–415.

Scholz, C. H. (2000), Evidence for a strong San Andreas fault, *Geology*, *28*, 163–166.

Schorlemmer, D., and M. C. Gerstenberger (2005), RELM testing center, *Seism. Res. Let.*, submitted.

Schorlemmer, D., and S. Wiemer (2005), Microseismicity data forecast rupture area, *Nature*, *434*, doi:10.1038/4341086a.

Schorlemmer, D., G. Neri, S. Wiemer, and A. Mostaccio (2003), Stability and significance tests for b-value anomalies: Example from the Tyrrhenian Sea, *Geophys. Res. Let.*, *30*(16), doi:10.1029/2004JB003234.

Schorlemmer, D., S. Wiemer, and M. Wyss (2004a), Earthquake statistics at Parkfield: 1. Stationarity of *b*-values, *J. Geophy. Res.*, *109*, B12307, doi:10.1029/2003GL017335.

Schorlemmer, D., S. Wiemer, M. Wyss, and D. Jackson (2004b), Earthquake statistics at Parkfield: 2. Probabilistic forecasting and testing, *J. Geophy. Res.*, *109*, B12308, doi:10.1029/2004JB003235.

Schorlemmer, D., M. C. Gerstenberger, S. Wiemer, and D. Jackson (2005a), Earthquake likelihood model testing, *Seism. Res. Let.*, submitted.

Schorlemmer, D., S. Wiemer, and M. Wyss (2005b), Variations in earthquake-size distribution across different stress regimes, *Nature*, doi:10.1038/04094.

Seggern, D. H. V., J. N. Brune, K. D. Smith, and A. Aburto (2003), Linearity of the earthquake recurrence curve to $m < -1$ from Little Skull Mountain aftershocks in Southern Nevada, *Bull. Seism. Soc. Am.*, *93*(6), 2493–2501.

Sekiguchi, H., and T. Iwata (2001), Source Process Inversion and Near-Source Ground Motion Simulation of the 2000 Tottoriken-Seibu, Japan, Earthquake ($M_w = 6.8$), *Eos Trans. AGU*, *82*(47), fall Meet. Suppl., Abstract S42C-0654.

Semmane, F., F. Cotton, and M. Campillo (2005), The 2000 Tottori earthquake: A shallow earthquake with no surface rupture and slip properties controlled by depth, *J. Geophy. Res.*, *110*, B03306, doi:10.1029/2004JB003194.

Shearer, P., E. Hauksson, and G. Lin (2005), Southern California Hypocenter Relocation with Waveform Cross-Correlation, Part 2: Results Using Source-Specific Station Terms and Cluster Analysis, *Bull. Seism. Soc. Am.*, *95*(3), 904–915, doi: 10.1785/0120040168.

Shi, Y., and B. A. Bolt (1982), The standard error of the magnitude-frequency b-value, *Bull. Seism. Soc. Am.*, *72*, 1677–1687.

Sieh, K. (2005), Aceh-Andaman earthquake: What happened and what's next?, *Nature*, *434*, 573–574, doi:10.1038/434573a.

Somerville, P., et al. (1999), Characterizing crustal earthquake slip models for the prediction of strong ground motion, *Seism. Res. Let.*, *70*(1), 59–80.

Steacy, S., J. Gomberg, and M. Cocco (2005), Introduction to special section: Stress transfer, earthquake triggering, and time-dependent seismic hazard, *J. Geophy. Res.*, *110*, B05S01, doi:doi:10.1029/2005JB003692.

Steidl, J. H., R. J. Archuleta, and S. Hartzell (1991), Rupture history of the 1989 Loma Prieta, California earthquake, *Bull. Seism. Soc. Am.*, *81*(5), 1573–1602.

Stein, R. S. (1999), The role of stress transfer in earthquake occurrence, *Nature*, *402*(6762), 605–609.

Stein, R. S. (2003), Earthquake conversations, *Scientific American*, *288*(1), 72–79.

Stein, R. S., G. C. P. King, and J. Lin (1992), Change in failure stress on the San Andreas and surrounding faults caused by the 1992 M=7.4 Landers earthquake, *Science*, *258*, 1328–1332.

Taylor, D. W. A., J. A. Snoke, I. S. Sacks, and T. Takanami (1990), Nonlinear frequency magnitude relationship for the Hokkaido corner, Japan, *Bull. Seism. Soc. Am.*, *80*, 340–353.

Thurber, C., S. Roecker, K. Roberts, M. Gold, and K. Rittger (2003), Earthquake locations and three dimensional fault zone structure along the creeping section of the San Andreas fault near Parkfield, CA: Preparing for SAFOD, *Geophys. Res. Let.*, *30*(3), 1112, doi:10.1029/2002GL016004.

Toda, S., and R. S. Stein (2003), Toggling seismicity by the 1997 Kagoshima earthquake couplet: a demonstration of time dependent stress transfer, *J. Geophy. Res.*, *108*(0), doi:10.1029/2003JB002547.

Toda, S., R. S. Stein, P. A. Reasenberg, J. H. Dieterich, and A. Yoshida (1998), Stress transferred by the 1995 $M_W = 6.9$ Kobe, Japan, shock: Effect on aftershocks and future earthquake probabilities, *J. Geophy. Res.*, *103*(B10), 24,543–24,565.

Toda, S., R. S. Stein, K. Richards-Dinger, and B. S. Bozkurt (2005), Forecasting the evolution of seismicity in southern California: Animations built on earthquake stress transfer, *J. Geophy. Res.*, *110*, B05S16, doi:10.1029/2003JB002547.

Uhrhammer, R.-A. (1986), Characteristics of northern and southern California seismicity (abstract), *Earthquake Notes*, *57*, 21.

Utsu, T. (1961), A statistical study of the occurence of aftershocks, *Geophys. Mag.*, *3*, 521–605.

Utsu, T. (1965), A method for determining the value of b in a formula $\log n = a - bm$ showing the magnitude frequency for earthquakes, *Geophys. Bull. Hokkaido Univ.*, *13*, 99–103.

Utsu, T. (1999), Representation and analysis of the earthquake size distribution: a historical review and some new approaches, *Pure appl. geophys.*, *155*, 509–535.

Vere-Jones, D. (1995), Forecasting earthquakes and earthquake risk, *International Journal of Forecasting*, *11*(4), 503–538.

Wald, D. J., and T. H. Heaton (1994), Spatial and temporal distribution of slip for the 1992 Landers, California, earthquake, *Bull. Seism. Soc. Am.*, *84*(3), 668–691.

Wald, D. J., D. V. Helmberger, and T. H. Heaton (1991), Rupture model of the 1989 Loma Prieta earthquake from the inversion of strong motion and broadband teleseismic data, *Bull. Seism. Soc. Am.*, *81*(5), 1540–1572.

Waldhauser, F., and W. L. Ellsworth (2000), A double-difference earthquake location algorithm: Method and application to the northern Hayward fault, California, *Bull. Seism. Soc. Am.*, *90*(6), 1353–1368.

Waldhauser, F., W. L. Ellsworth, D. P. Schaff, and A. Cole (2004), Streaks, multiplets, and holes: High-resolution spatio-temporal behavior of Parkfield seismicity, *Geophys. Res. Let.*, *31*, L18608, 10.1029/2004GL020649.

Wells, D. L., and K. J. Coppersmith (1994), New empirical relationships among magnitude, rupture length, rupture width, rupture area, and surface displacement, *Bull. Seism. Soc. Am.*, *84*(4).

Wessel, P., and W. H. F. Smith (1991), Free software helps map and display data, *Eos Trans. AGU*, *72*(441), 445–446.

Wiemer, S. (2000), Introducing probabilistic aftershock hazard mapping, *Geophys. Res. Let.*, *27*(20), 3405–3408.

Wiemer, S. (2001), A software package to analyze seismicity: ZMAP, *Seism. Res. Let.*, *72*(2), 373–382.

Wiemer, S., and K. Katsumata (1999), Spatial variability of seismicity parameters in aftershock zones, *J. Geophy. Res.*, *104*, 135–151.

Wiemer, S., and M. Wyss (1994), Seismic quiescence before the Landers (M=7.5) and Big Bear (M=6.5) 1992 earthquakes, *Bull. Seism. Soc. Am.*, *84*, 900–916.

Wiemer, S., and M. Wyss (1997), Mapping the frequency-magnitude distribution in asperities: An improved technique to calculate recurrence times?, *J. Geophy. Res.*, *102*(B7), 15,115–15,128.

Wiemer, S., and M. Wyss (2000), Minimum magnitude of complete reporting in earthquake catalogs: examples from Alaska, the Western United States, and Japan, *Bull. Seism. Soc. Am.*, *90*, 859–869.

Wiemer, S., and M. Wyss (2002), Mapping spatial variability of the frequency-magnitude distribution of earthquakes, *Advances in Geophysics*, *45*, 259–302.

Wiemer, S., and M. Wyss (2003), Reply to "Comment on 'Minimum magnitude of completeness in earthquake catalogs examples from Alaska, the Western United States and Japan' by Stefan Wiemer and Max Wyss", *Bull. Seism. Soc. Am.*, *93*(4), 1868–1871.

Wiemer, S., S. R. McNutt, and M. Wyss (1998), Temporal and three-dimensional spatial analyses of the frequency-magnitude distribution near Long Valley caldera, California, *Geophys. J. Int.*, *134*, 409–421.

Wiemer, S., M. Gerstenberger, and E. Hauksson (2002), Properties of the 1999, M_W 7.1, Hector Mine earthquake: Implications for aftershock hazard, *Bull. Seismol. Soc. Am.*, *92*(4), 1227–1240.

Woessner, J., and S. Wiemer (2005), Assessing the quality of earthquake catalogs: Estimating the magnitude of completeness and its uncertainties, *Bull. Seism. Soc. Am.*, *95*(2), doi:10.1785/0120040007.

Woessner, J., E. Hauksson, S. Wiemer, and S. Neukomm (2004a), The 1997 Kagoshima (Japan) earthquake doublet: A quantitative analysis of aftershock rate changes, *Geophys. Res. Let.*, *31*, L03605, doi:10.1029/2003GL018858.

Woessner, J., D. Schorlemmer, M. C. Gerstenberger, and S. Wiemer (2004b), Seismicity Patterns of the September 28th Parkfield Event, *Eos Trans. AGU*, *85*(47), abstract S51C-0170V.

Wyss, M., and Y. Toya (2000), Is background seismicity produced at a stationary poissonian rate?, *Bull. Seism. Soc. Am.*, *90*(5), 1858–1866.

Wyss, M., and S. Wiemer (1999), How can one test the seismic gap hypothesis? The case of repeated rupture in the Aleutians, *Pure appl. geophys.*, *155*, 4259–278.

Wyss, M., and S. Wiemer (2000), Change of probability for earthquakes in southern California due to the Landers magnitude 7.3 earthquake, *Science*, *290*, 1334–1388.

Yeats, R. S., K. Sieh, and C. R. Allen (1997), *The Geology of Earthquakes*, Oxfords University Press, New York.

Zoback, M. D., and G. C. Beroza (1993), Evidence for near-frictionless faulting in the 1989 (m 6.9) loma prieta, california, earthquake and its aftershocks, *Geology*, *21*(2), 181–185.

Zöller, G., S. Hainzl, M. Hohlschneider, and Y. Ben-Zion (2005), Aftershocks resulting from creeping sections in a heterogeneous fault, *Geophys. Res. Let.*, *32*(L03308), doi:10.1029/2004GL021871.

Zúñiga, F. R., and S. Wiemer (1999), Seismicity patterns: are they always related to natural causes?, *Pure appl. geophys.*, *155*, 713–726.

Seite Leer /
Blank leaf

Acknowledgements

I would like to thank "the boss" Stefan Wiemer, my "co-advisor" Martin Mai, and the "real boss" Domenico Giardini for providing me the opportunity to accomplish my thesis in a very convienent research enviroment.

Special thanks to Stefan for sharing so many ideas, leaving me enough space for developing my ideas, discussing every detail of my research, supporting my scientific travel desires and staying positive throughout the time. It's been a real pleasure!

Thanks to Egill Hauksson for provding me the opportunity to stay at the California Institute of Technology for a three months period and accepting to be co-examiner.

Thanks to Martin for sharing his expertise and sincerely trying to answer the daily questions on earthquake source physics. I profited a lot from our discussions.

Many, many, many, ..., so many thanks to Danijel for endless discussions on statistical testing, for solving computer problems, for being so critical reading my papers and being picky about sloppy figures. I will not forget having a few beers and discussing life on the lakeside every once in a while.

Thanks to my switching office mates Cedric, Tobias, Thomas, DJ Doloop Gregor and Rippi for all sorts of discussions and not complaining about me listening to great music. I had a great time with you guys!

Thanks to all members of the institute, especially Elisabeth and Andre for helping me out each time I needed something, most of the time when I was too late. I will not forget the Marx-brothers and the Ramones for running the jobs when I spent my time relaxing from work.

Thanks to all my friends for endless evenings on the balconies, the nights in the

pubs, and wearing me out doing sports: Antje, Inka, Jenny, Julia, Karin, Nicole, Sarah, Sybille, Sonja (a few of them), Suzanne, Bernhard, Craig, Dominic, Fortunat, Jörg, Martin, Michi, Miro, Res, Rüdi, Samuel, Sjonny, Stefano, Thomas (again a few), Ueli and the FC Unterstrass, Frank and the TC Dornhan, and Real Anabolica for at least one competitive summer soccer season. Special thanks to the Alps for so many possibilities to snowboard, ski, hike and mountain bike, the waves and the wind to let me windsurf bringing me back to life from hacking the keyboard.

Looking abroad, thanks to the CalTech team, SCEC, Odile and Matt, Georgia and John for their hospitality in Pasadena!

Thanks to S. Toda, D. D. Jackson, S. Miller and Y. Ben-Zion for fruitful discussions.

Very special thanks to Corinne for not being too frustrated with me being absent and not listening enough to you in the final stage of the thesis. I'd loved to spend more time with you!

Nothing is more pleasant than knowing that one can rely on his family! Thanks to my mother, my dad, my brother and his growing family for your support and the great times at home!

Curriculum Vitae

Jochen Wößner

born June 25, 1973, Sulz a. N., Germany
citizen of Germany

10/1993–07/1996	University of Konstanz, Konstanz, Physics
08/1996–06/1997	University of Arizona, Tucson, Physics
10/1997–10/2000	University of Karlsruhe (TH), Karlsruhe, Geophysics Diploma thesis: Modelling strong ground motion seismograms in the Upper Rhinegraben using Empirical Green's Functions
11/2000–01/2001	University of Karlsruhe (TH), Karlsruhe, Geophysics Assistant Researcher
02/2001–04/2002	Swiss Federal Institute of Technology (ETH), Zürich, Swiss Seismological Service Assistant Researcher
05/2002–09/2005	Swiss Federal Institute of Technology (ETH), Zürich, Swiss Seismological Service Doctoral thesis: Correlating Statistical Properties of Aftershocks to Earthquake Physics
11/2005	Expected degree: Doctor of Natural Sciences. Swiss Federal Institute of Technology (ETH), Zürich, Switzerland